

# Efficient frequency doubling of near-infrared diode lasers using quasi phase-matched waveguides

vorgelegt von

Diplom-Physiker  
Daniel Jędrzejczyk

geb. in Bielsko-Biała, Polen

von der Fakultät IV - Elektrotechnik und Informatik -  
der Technischen Universität Berlin

zur Erlangung des akademischen Grades  
Doktor der Naturwissenschaften  
- Dr. rer. nat. -

genehmigte Dissertation

Promotionsausschuss:

Vorsitzender: Prof. Dr.-Ing. Wolfgang Heinrich, TU Berlin

Gutachter: Prof. Dr. Günther Tränkle, TU Berlin

Prof. Dr. Günter Huber, Universität Hamburg

Prof. Dr. Michael Kneissl, TU Berlin

Tag der wissenschaftlichen Aussprache: 19. Dezember 2014

Berlin 2015



# Abstract

Single-pass frequency doubling of near-infrared (NIR) diode lasers in quasi phase-matched nonlinear bulk crystals represents a straightforward approach to realize efficient and compact green emitting lasers in continuous-wave (CW) operation with a high output power and a nearly diffraction-limited beam quality [19, 20]. In this thesis, the application of waveguide structures, instead of bulk crystals, is investigated theoretically and experimentally with the objective of increasing the efficiency of such laser systems. In particular, a complemented study of second-harmonic generation (SHG) in periodically poled MgO-doped lithium niobate (MgO:LN) ridge and planar waveguides is conducted in order to identify all benefits and limitations for both geometries with respect to maximum conversion efficiency and accessible power in the green spectral region.

In the first part of this work frequency doubling of a DBR ridge waveguide diode laser in a periodically poled MgO:LN ridge waveguide is studied. In particular, the influence of structural imperfection, optical absorption and subsequent heat generation on the conversion efficiency of the nonlinear interaction is investigated in-depth by means of experiments and numerical simulations.

In the second part of this work frequency doubling of a DBR tapered diode laser in a periodically poled MgO:LN planar waveguide is investigated. Prior to high-power experiments, a comprehensive experimental study of the normalized SHG conversion efficiency in planar waveguides as a function of spatial diode laser beam parameters is carried out in order to provide optimum values with corresponding tolerances for subsequent experiments.

The application of periodically poled MgO:LN waveguide structures for frequency doubling of NIR diode lasers results in this thesis in a distinct improvement of the opto-optical conversion efficiency. An increase from approx. 20 % in a bulk crystal to almost 30 % in a planar waveguide and approx. 40 % in a ridge waveguide is achieved. However, unlike in a bulk crystal, the maximum generated power is limited in both waveguide geometries. In a ridge-waveguide the maximum second-harmonic (SH) power of nearly 0.4 W is limited due to its gradual saturation with increasing NIR pump power accompanied by an increase in the propagation loss, which is attributed to nonlinear absorption. The nonlinear absorption affects the SHG process starting from an SH wave intensity of approx.  $1.7 \text{ MW/cm}^2$ . Above an SH wave intensity of approx.  $3.1 \text{ MW/cm}^2$  a saturation of the SH output power can be observed. In a planar waveguide the maximum generated SH power of approx. 1.2 W is limited due to its gradual

saturation with increasing NIR pump power. However, unlike in case of the ridge waveguide, no distinct increase of loss in the investigated power range can be determined. In addition, the maximum SH wave power density is determined here to  $0.3 \text{ MW/cm}^2$ , which is one order of magnitude lower compared to the maximum SH wave intensity in the ridge waveguide structure. Therefore, the experimentally observed power limitation in a planar waveguide is attributed to thermally induced quasi phase-matching distortion, caused by waveguide cladding material not suitable for high power operation. Higher maximum output power is expected for improved planar waveguide structures.

The generated laser radiation in the green spectral range is characterized by a single-frequency spectrum and nearly diffraction-limited beam quality and is therefore well suited for applications in the fields of bio-medicine, bio-technology and spectroscopy.

# Kurzfassung

Frequenzverdopplung von nah-infraroten (NIR) Diodenlasern im einfachen Durchgang durch nichtlineare, periodisch gepolte Volumenkristalle stellt eine einfache Anordnung dar, um effiziente und kompakte, grün emittierende Laserstrahlquellen mit hoher Ausgangsleistung im Dauerstrichbetrieb und annähernd beugungsbegrenzter Strahlqualität zu realisieren [19, 20]. Im Rahmen dieser Arbeit wird die Verwendung von Wellenleiterstrukturen anstelle von Volumenkristallen theoretisch und experimentell mit dem Ziel betrachtet, die Konversionseffizienz solcher Lasersysteme zu steigern. Insbesondere wird die Erzeugung der zweiten Harmonischen in periodisch gepolten Rippen- und Planarwellenleitern aus MgO-dotierten Lithiumniobat (MgO:LN) ausführlich untersucht, um die Vorteile und Grenzen beider Strukturen bezüglich der maximalen Konversionseffizienz und der maximal erreichbaren Ausgangsleistung im grünen Spektralbereich zu finden.

Im ersten Teil dieser Arbeit wird die Frequenzverdopplung der Strahlung eines DBR-Rippenwellenleiterlasers in einem periodisch gepolten MgO:LN-Rippenwellenleiter betrachtet. Insbesondere wird dabei der Einfluss der Strukturinhomogenität, der optischen Absorption und der daraus resultierenden Wärmeentwicklung auf die Konversionseffizienz dieser nichtlinearen Wechselwirkung sowohl experimentell als auch durch numerische Simulationen ausführlich untersucht.

Im zweiten Teil dieser Arbeit wird die Frequenzverdopplung der Strahlung eines DBR-Trapezlasers in periodisch gepolten MgO:LN-Planarwellenleitern dargelegt. Zur Vorbereitung auf die Hochleistungsexperimente wird zunächst die normierte Konversionseffizienz in planaren Wellenleitern als Funktion von räumlichen Strahlparametern ausführlich untersucht, um die optimalen Werte und die dazugehörigen Toleranzen zu finden.

Die Verwendung von periodisch gepolten MgO:LN-Wellenleiterstrukturen für die Frequenzverdopplung von NIR-Diodenlasern führt in dieser Arbeit zu einer verbesserten opto-optischen Konversionseffizienz. Deren Erhöhung von ca. 20 % in Volumenkristallen [9, 10] auf hier nahezu 30 % in einem planaren Wellenleiter und auf ca. 40 % in einem Rippenwellenleiter wird beobachtet. Im Gegensatz zu Volumenkristallen ist die maximal erreichbare Ausgangsleistung in beiden Wellenleiterstrukturen jedoch begrenzt. In einem Rippenwellenleiter ist die maximale Leistung der zweiten Harmonischen auf nahezu 0,4 W begrenzt, und zwar durch die mit steigender NIR-Pumpleistung graduell auftretende Sättigung. Gleichzeitig wird eine Erhöhung der Ausbreitungsverluste beobachtet, die

auf die nichtlineare Absorption zurückzuführen ist. Die nichtlineare Absorption beeinflusst den nichtlinearen Prozess der Frequenzverdopplung ab einer Intensität der zweiten Harmonischen von ca.  $1,7 \text{ MW/cm}^2$ . Oberhalb einer Intensität der zweiten Harmonischen von ca.  $3,1 \text{ MW/cm}^2$  ist eine Sättigung der Leistung der zweiten Harmonischen zu beobachten. Für den Planarwellenleiter ergibt sich eine Leistungsgrenze für die zweite Harmonische von ca.  $1,2 \text{ W}$ , wiederum verursacht durch die mit steigender NIR-Pumpleistung graduell auftretende Sättigung. Jedoch kann im Gegensatz zum Rippenwellenleiter in den planaren Wellenleitern keine deutliche Erhöhung der Ausbreitungsverluste festgestellt werden. Des Weiteren wird hier die maximale Intensität der zweiten Harmonischen zu einem Wert von  $0,3 \text{ MW/cm}^2$  bestimmt, welcher im Vergleich zu der maximalen Intensität im Rippenwellenleiter um eine Größenordnung kleiner ist. Folglich ist die im Planarwellenleiter experimentell beobachtete Leistungsbegrenzung auf eine thermisch verursachte Störung der Quasi-Phasenanpassung zurückzuführen, die durch das für hohe Leistungen nicht geeignete Mantelmaterial des Wellenleiters verursacht wird. Höhere Ausgangsleistungen sind für optimierte planare Wellenleiterstrukturen zu erwarten.

Die erzeugte Strahlung im grünen Spektralbereich ist durch ein einmodiges Emissionsspektrum und durch eine nahezu beugungsbegrenzte Strahlqualität gekennzeichnet. Sie ist deswegen für die Anwendungen im Bereich der Biomedizin, Biotechnologie und Spektroskopie gut geeignet.

# Acknowledgment

First and foremost, I would like to express my sincere gratitude to Prof. Dr. Günther Tränkle for offering me the opportunity to conduct research leading to the results of this work at the Ferdinand-Braun-Institut, Leibniz-Institut für Höchstfrequenztechnik, and for supervising this thesis. His active interest in my work, his constant advice and encouragement have been of great help during the course of this work.

I also owe my sincere gratitude to Prof. Dr. Günter Huber and Prof. Dr. Michael Kneissl for agreeing to act as further appraisers of this work.

I am sincerely grateful to Dr. Katrin Paschke for her guidance and constructive ideas. Her permanent availability to provide advice and support in terms of technical and organizational matters at all stages of this work were crucial to its progress and are greatly appreciated.

I am deeply grateful to Dr. Reiner Güther for his guidance and valuable advice in the course of this work. His exceptional knowledge in the fields of diode lasers and nonlinear optics contributed considerably to my understanding of the related physical phenomena.

I am very grateful to Dr. Bernd Eppich for his support, particularly in the fields of spatial characterization and propagation simulation of laser beams.

I am indebted to Dr. Götz Erbert for many technical discussions and his valuable advice, especially with regard to diode lasers used in the frame of this work.

I am grateful to all colleagues at Ferdinand-Braun-Institut, who have contributed to the design, epitaxy, coating and mounting of diode lasers applied in this work. In particular, I wish to thank Dr. Bernd Sumpf, Dr. Karl-Heinz Hasler and Dr. Christian Fiebig for fruitful discussions on diode laser properties. I sincerely thank all members of the mechanical department under the direction of Thomas Roos for their patience in constructing and adopting of mechanical components for the needs of my experimental setup, particularly the nonlinear crystal mounts. I also want to thank the present and past members of the group "Hybrid Diode Laser Systems" for their tolerance, motivation and support.

I am grateful to Mr. Yasuhiko Hakotani from Panasonic Electronic Devices Co., Ltd., to Mr. Paolo Byun from Commax Co., Ltd. and to Dr. Han-Young Lee from Korea Electronics Technology Institute for fruitful discussions on QPM waveguide devices.

The financial support of the German Federal Ministry of Education and Research within the InnoProfile initiative "Hybride Diodelaser-Systeme" (Grant No. 03IP613) is gratefully acknowledged.

Finally, I wish to thank my parents for their love and understanding. Their encouragement and support during my studies and during the course of this thesis contributed greatly to its successful completion. I also thank my parents-in-law for their encouragement and motivation.

Most of all, I wish to thank my wife Anya for her love and support. No laser will ever shine brighter than you, you are my sunshine!

# Contents

<b>Abstract</b>	<b>iii</b>
<b>Kurzfassung</b>	<b>v</b>
<b>Acknowledgment</b>	<b>vii</b>
<b>Contents</b>	<b>ix</b>
<b>1 Introduction</b>	<b>1</b>
<b>2 Design and selection of NIR diode lasers for frequency doubling</b>	<b>3</b>
2.1 Fundamentals of diode lasers . . . . .	3
2.1.1 Inversion and optical gain . . . . .	3
2.1.2 Optical cavity and laser threshold . . . . .	5
2.1.3 Longitudinal single-mode operation . . . . .	7
2.1.4 Lateral confinement . . . . .	7
2.1.5 Spatial properties of a diode laser beam . . . . .	8
2.2 Requirements for diode lasers intended for frequency doubling . . . . .	9
2.3 Single emitters design and selection . . . . .	10
2.3.1 Vertical design . . . . .	10
2.3.2 Resonator layout . . . . .	11
<b>3 Waveguide structures for SHG into the green spectral region</b>	<b>15</b>
3.1 Introduction to integrated optics . . . . .	15
3.1.1 Propagation constant and effective refractive index . . . . .	16
3.1.2 Electric field distributions . . . . .	17
3.1.3 Loss . . . . .	17
3.2 Nonlinear optics . . . . .	19
3.2.1 Dielectric polarization and nonlinear coefficient . . . . .	19
3.2.2 Second-harmonic generation . . . . .	21
3.2.3 Quasi phase-matching . . . . .	22
3.2.4 SH power dependency on the fundamental power . . . . .	26
3.3 Design and selection of waveguide SHG devices . . . . .	30
3.3.1 MgO doped lithium niobate . . . . .	31
3.3.2 Ridge waveguide . . . . .	32
3.3.3 Planar waveguides . . . . .	34

<b>4</b>	<b>Diode laser frequency doubling in a ridge waveguide</b>	<b>37</b>
4.1	Experimental setup . . . . .	38
4.2	Diode laser characteristics . . . . .	39
4.3	Experimental results . . . . .	41
4.4	Development of a tailored theoretical model . . . . .	45
4.4.1	System of coupled equations . . . . .	46
4.4.2	Quasi phase-matching condition . . . . .	46
4.4.3	Heat and temperature distribution . . . . .	46
4.5	Exemplary simulation models . . . . .	48
4.6	Comparison between results of experiment and simulation . . .	50
4.7	Summary . . . . .	57
<b>5</b>	<b>Diode laser frequency doubling in planar waveguides</b>	<b>59</b>
5.1	Frequency doubling of a near-Gaussian beam . . . . .	60
5.1.1	Experimental setup . . . . .	60
5.1.2	Near-Gaussian beam characteristics . . . . .	62
5.1.3	SHG with a near-Gaussian beam . . . . .	65
5.1.4	SH beam characteristics . . . . .	67
5.2	Frequency doubling of a DBR-TPL beam . . . . .	68
5.2.1	Experimental setup . . . . .	68
5.2.2	Diode laser characteristics . . . . .	69
5.2.3	SHG process subject to pump beam parameters . . . . .	73
5.2.4	High-power generation . . . . .	78
5.2.5	SH beam characteristics . . . . .	83
5.3	Summary . . . . .	84
<b>6</b>	<b>Final conclusions and perspectives</b>	<b>87</b>
6.1	Summary and conclusions . . . . .	87
6.2	Future directions . . . . .	89
	<b>Appendix</b>	<b>91</b>
A.1	Equipment used for measurements . . . . .	91
A.2	Propagation of uncertainty . . . . .	93
	<b>List of publications</b>	<b>95</b>
	<b>Bibliography</b>	<b>97</b>

# Chapter 1

## Introduction

In over five decades since its invention [1], not only has the laser found widespread applications in science and industry, but it has also become an irreplaceable tool in our everyday life. Due to a permanent improvement in its performance, flexibility and diversity, the number of applications has been growing rapidly over the years. However, in spite of a high demand, the availability of efficient and compact laser systems in the green spectral range has been limited until recently.

Such lasers, that are additionally characterized by an output power of several hundred milliwatt in continuous-wave operation and a nearly diffraction limited beam quality, are required in a variety of application fields. The green spectral region, characterized by a very low absorption in water, is particularly interesting for bio-medical and bio-technical applications, such as, for example, flow cytometry [2]. In addition, such laser systems are also required in the fields of spectroscopy, in which case single-frequency emission is often indispensable [3]. Furthermore, efficient and compact lasers in the green spectral region with moderate power have already found wide application in the rapidly growing field of laser display technology [4]. Finally, in the high-power range, a laser with the aforementioned characteristics can be utilized as a pump source for a Ti:Sapphire laser [5].

In recent years, a few approaches to realize miniaturized and efficient green emitting lasers have been introduced, among which frequency doubling of near-infrared diode lasers in quasi phase-matched nonlinear bulk crystals provides a number of advantages. In comparison to direct diode lasers based on In-GaN [6, 7, 8], the aforementioned concept enables a higher output power [9, 10]. In addition, it provides single-frequency emission and is also suitable for generation of laser radiation in the yellow spectral range [11, 12]. As opposed to frequency doubled solid-state lasers [13, 14, 15] and blue diode laser pumped Pr:YLF lasers [16, 17, 18], frequency doubling of near-infrared diode lasers is not limited to strict atomic transitions and, therefore, enables generation of arbitrary wavelengths. Furthermore, wavelength tuning over a range of several hundred picometer can be achieved by adjusting the temperature and the injection current. An important additional argument in favor of direct second-harmonic generation with diode lasers is also the already demonstrated miniaturization

---

of this concept in a straightforward single-pass configuration [19, 20].

Apart from the advantages of direct diode laser frequency doubling in a single-pass configuration, the low conversion efficiency of the nonlinear interaction in a bulk crystal represents the main disadvantage of this concept. This impediment, which is induced by a relatively low fundamental radiation intensity resulting from crystal length dependent laser beam focusing [21], is additionally reinforced in case of diode lasers by laser beam quality degradation with increasing output power. The improvement of the conversion efficiency during frequency doubling of near-infrared diode lasers is therefore a key factor to ensure high wall-plug efficiency of miniaturized green emitting laser modules, based on this approach [19, 20]. The target of this thesis is to investigate the potential of quasi phase-matched waveguide structures for this purpose. In this context, an extensive study of second-harmonic generation in ridge and planar waveguides is conducted in order to identify all benefits and limitations for both geometries with respect to maximum conversion efficiency and accessible second-harmonic power range.

This thesis is organized as follows: in Chapter 2 fundamentals of diode lasers are discussed, followed by the presentation of requirements for single emitters suitable for frequency doubling, and the description of near-infrared diode lasers applied in this work. Chapter 3 covers the fundamentals of integrated optics and nonlinear optics. In case of the latter field the focus is laid on the concepts of second-harmonic generation and quasi phase-matching. Subsequently, the waveguide structures applied in this work for second-harmonic generation into the green spectral region are discussed.

In Chapter 4, efficient frequency doubling of a diode laser in a ridge waveguide structure is demonstrated. In particular, the influence of structural imperfection, optical absorption and subsequent heat generation on the conversion efficiency of the nonlinear interaction is investigated in-depth by means of experiments and numerical simulations.

In Chapter 5, efficient high-power frequency doubling of a diode laser in a planar waveguide is demonstrated. Prior to high-power experiments, the second-harmonic generation process is investigated extensively with respect to near-infrared pump beam parameters, resulting in a definition of their optimum values with corresponding tolerances. Summary, conclusions and perspectives are presented in Chapter 6.

# Chapter 2

## Design and selection of NIR diode lasers for frequency doubling

### 2.1 Fundamentals of diode lasers

Laser operation from a semiconductor material was demonstrated for the first time in 1962 [22, 23, 24, 25, 26]. In the following years a room-temperature continuous-wave (CW) operation [27, 28] and significant reliability improvement [29, 30, 31] were achieved. The robustness and small footprint of diode lasers, as well as the feasibility of mass-production at low cost resulted in two early commercial applications in the field of data storage and optical communication [32, p. 3]. Over the years, diode laser technology evolved further enclosing diverse new applications in different spectral and power ranges.

At the present day, diode lasers are the most efficient lasers reaching maximum electro-optical conversion efficiency in extent of 70 % [33, 34, 35]. They find application in a wide scope of fields, ranging from pumping of solid state and fiber lasers [36, 37], through material processing [38], spectroscopy [39, 40] and metrology [41] to free space communication [42, 43].

In this section, the fundamentals of diode lasers are discussed. The population inversion and optical gain are described in Sect. 2.1.1, followed by the concept of optical cavity and laser threshold in Sect. 2.1.2. In Sect. 2.1.3 and 2.1.4 the resonator concepts for longitudinal single-mode operation and the methods for lateral confinement are presented, respectively. Finally, in Sect. 2.1.5 the spatial characteristics of a diode laser beam are discussed.

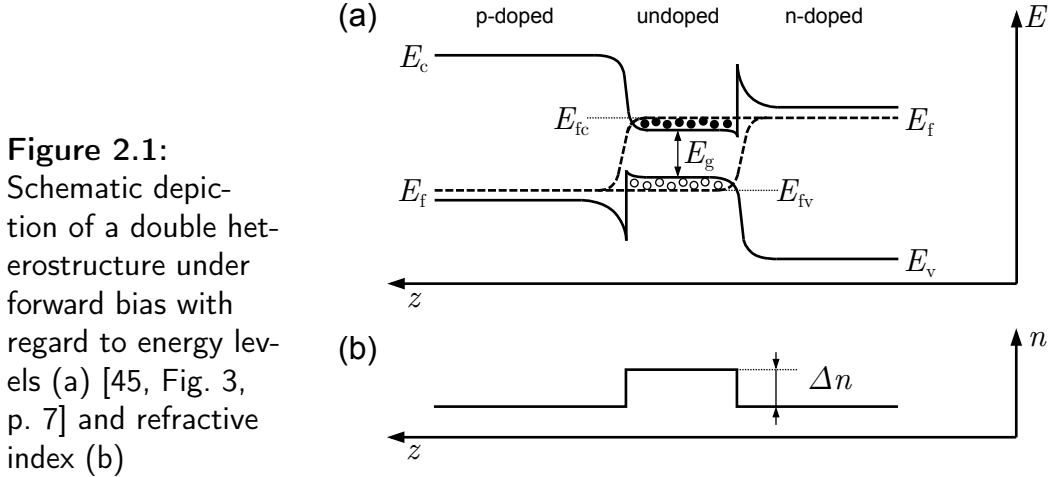
#### 2.1.1 Inversion and optical gain

Selective doping with donors and acceptors as well as concentration variation of semiconductor layers during growth enables the fabrication of a double heterostructure, a fundamental component of a diode laser. This is basically a pin-junction complemented by a joint confinement region for both charge carriers and photons. The charge carriers are confined due to lower band gap energy, the photons due to higher refractive index, as presented in Fig. 2.1 (a) and (b), respectively. Under forward bias this structure provides a local

inversion in the population of energy states, a condition which needs to be fulfilled in order for laser operation to take place. The dominant optical transition between the conduction and valence band in the confinement region determines the wavelength of the emitted electro-magnetic radiation. This generated optical field propagating through the junction is amplified further by means of stimulated emission due to the presence of population inversion. The amplification is described by the relation

$$\mathcal{J}(x) = \mathcal{J}(0) e^{\gamma x} \quad (2.1)$$

in accordance with [44, Eq. 9.28, p. 225], where  $\mathcal{J}$  is the intensity of light,  $x$  is the propagation direction and  $\gamma$  is the material gain. Since gain is directly proportional to the difference between the electron populations in the conduction and valence band [44, Eq. 9.29, p. 225], negative gain and therefore attenuation of radiation is present in case of thermal equilibrium, i.e. no forward bias. However, as mentioned above, under forward bias the population inversion



results in a positive value of  $\gamma$  and a corresponding amplification. In general, photon energy and carrier density have a significant influence on the optical gain profile [44, p. 225], calculation of which is however beyond the scope of this work. Positive gain is expected in the photon energy region given by

$$E_g < h\nu < E_{fc} - E_{fv} \quad (2.2)$$

in accordance with [44, Eq. 9.33, p. 226], where  $E_g$  is the band gap energy,  $h\nu$  is the photon energy and  $E_{fc}$  and  $E_{fv}$  are the conduction and valence quasi Fermi levels, respectively, as depicted in Fig. 2.1 (a).

Modern diode lasers consist of a separate confinement double heterostructure [44, p. 242] with separate confinement regions for charge carriers and photons, as presented schematically in Fig. 2.2 (a). The latter are confined in a thicker optical waveguide, preferably in the waveguide lowest-order mode, the former

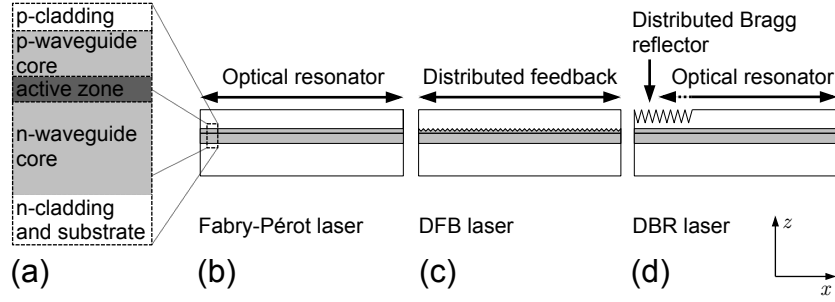


**Figure 2.2:** Schematic depiction of a separate confinement double heterostructure (a), depiction of a Fabry-Pérot laser (b), a DFB laser (c) and a DBR laser (d)

are confined in a much thinner active zone. The confinement factor [45, Eq. 21, p. 11]

$$\Gamma = \frac{\int_{AZ} \mathfrak{J}^{(m)}(z) dz}{\int_{-\infty}^{+\infty} \mathfrak{J}^{(m)}(z) dz} \quad (2.3)$$

defines the overlap between the intensity distribution  $\mathfrak{J}^{(m)}(z)$  of the optical waveguide mode  $m = 0, 1, 2, \dots$  and the active zone (AZ). The gain of the corresponding optical mode  $\gamma_{\text{modal}}$  amounts to

$$\gamma_{\text{modal}} = \Gamma\gamma, \quad (2.4)$$

as described in detail in [45, p. 10]. During design of diode laser structures care needs to be taken for the modal gain of waveguide higher-order modes to be lower than of the fundamental mode.

Primarily, quantum-well structures [46] utilizing quantum effects [44, p. 49] are applied as active region, since they assure lower threshold current density and a lower linewidth enhancement factor [44, p. 243]. Furthermore, the polarization or emission wavelength in a quantum-well can be adjusted due to strain effects. In addition, multiple quantum-wells [47] provide a higher overall gain and a superior performance at high currents [44, p. 243].

## 2.1.2 Optical cavity and laser threshold

For laser operation to begin, optical feedback into the active medium is required. A resonant cavity providing optical oscillation is well suited for this purpose. In case of edge-emitting diode lasers, a Fabry-Pérot resonator, consisting of two parallel mirrors as depicted in Fig. 2.2 (b), is created through proper facet cleaving.

The consideration of gain and loss during single resonator roundtrip allows to define the threshold gain value [45, Eq. 24, p 13]

$$\Gamma\gamma_{\text{th}} = \alpha_i + \alpha_M \quad (2.5)$$

$$= \alpha_i + \frac{1}{2L_R} \ln \frac{1}{R_f R_r}, \quad (2.6)$$

at which the internal loss  $\alpha_i$  and the mirror loss  $\alpha_M$  are compensated and the laser operation begins. Here,  $L_R$  is the resonator length and  $R_f$  and  $R_r$  is the reflectivity of the front and rear facet, respectively. The radiation coupled out from the resonator through the facet forms the laser beam which is then available for the desired application.

The threshold gain  $\gamma_{th}$  is reached at a threshold current density  $\mathcal{I}_{th}$ , which, for a given injection area, corresponds to a threshold current  $I_{th}$ . Below this value the output power  $P$ , driven by spontaneous emission, increases insignificantly with increasing current  $I$ , as shown schematically in Fig. 2.3. The transition to

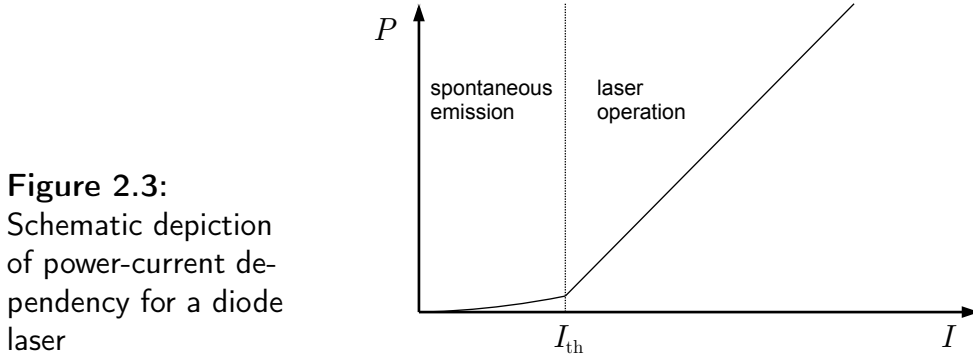


**Figure 2.3:**  
Schematic depiction  
of power-current de-  
pendency for a diode  
laser

stimulated emission at the threshold current  $I_{th}$  induces a linear dependency between the output power and the injection current. The output power is then given in accordance to [45, Eq. 93, p. 44] by

$$P = \eta_d \left( \frac{h\nu}{q} \right) (I - I_{th}) \quad (2.7)$$

with differential conversion efficiency  $\eta_d$ , photon energy  $h\nu$  and electron charge  $q$ .

An optical resonator provides oscillation for its resonance frequencies defined as

$$\nu = \frac{c_0}{2 L_R n(\nu)} m \quad (2.8)$$

in accordance to [44, Eq. 9.44, p. 234] with velocity of light in vacuum  $c_0$ , resonator length  $L_R$ , refractive index  $n$  and an integer  $m$ . All resonance frequencies, for which the threshold gain defined in Eq. (2.5) is reached, can contribute to the laser operation. In general, this results in a broadband laser emission.

The resonance frequencies from Eq. (2.8) correspond to longitudinal modes in the wavelength distribution. The permitted wavelength values are defined as

$$\lambda = \frac{2 L_R n(\lambda)}{m} \quad (2.9)$$

according to [45, Eq. 19, p. 10] with the corresponding mode spacing [45, Eq. 54, p. 33]

$$\Delta\lambda = \frac{\lambda^2}{2 L_R n_{gr}}, \quad (2.10)$$

where  $n_{gr}$  is the group index of refraction [48, p. 298].

### 2.1.3 Longitudinal single-mode operation

Laser operation in a longitudinal single-mode can be obtained through a targeted control of the mirror loss  $\alpha_M$  from Eq. (2.5) by an application of a wavelength selective mirror. A grating is well suited for this purpose, since the periodic modulation of a refractive index induced in this manner leads to a wavelength dependent Bragg reflection.

Two sorts of diode lasers with distributed-feedback can be distinguished. A distributed feedback (DFB) laser, in case of which the grating is integrated in the active region over its entire length, is presented schematically in Fig. 2.2 (c). A distributed Bragg reflector (DBR) laser makes use of a biased active region and a passive grating region operating as a cavity mirror, as depicted in Fig. 2.2 (d). In both cases the effective refractive index is modulated, either by longitudinal refractive index variation in the waveguide core [49, 36] or by surface etching of the cladding layer [50, 51]. For a grating period  $\Lambda_{\text{DBR}}$ , effective refractive index  $N$  and integer grating mirror order  $m$ , a targeted DBR emission wavelength

$$\lambda_{\text{DBR}} = \frac{2N}{m} \Lambda_{\text{DBR}} \quad (2.11)$$

is expected [44, Eq. 9.69, p. 260]. According to the coupled-wave theory [52, 53] for wavelengths around this value the forward and backward traveling waves are coupled. The strength and the spectral range of this interaction is defined by grating properties, such as its order and shape, corrugation duty cycle and depth and residual distance to the active region [54]. The proper choice of these parameters results therefore in a longitudinal single-mode operation.

### 2.1.4 Lateral confinement

Gain-guided lasers make use exclusively of current confinement in the lateral direction, based on current injection through a defined conductive area on the surface of a diode laser, as shown schematically in Fig. 2.4 (a). In such devices

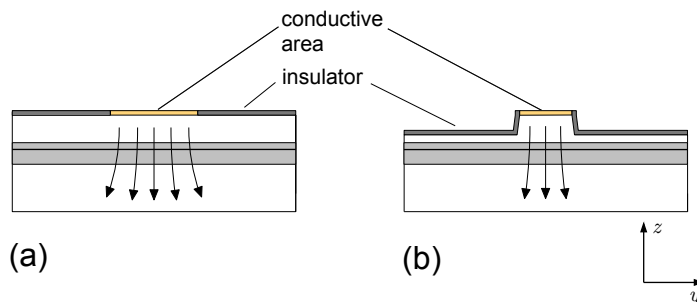


**Figure 2.4:** Schematic depiction of lateral confinement concepts: gain-guiding (a) and index-guiding (b)

the inversion and therefore the positive material gain  $\gamma$  can only be generated below the conductive stripe area. Outside of it the laser operation is not possible due to optical loss. Furthermore, during laser operation a thermally induced refractive index increase due to resistive heating in the current injection area can lead to a lateral wave-guiding.

Geometrical index-guiding resulting from a difference in the effective refractive

index is presented schematically in Fig. 2.4 (b). This method is used, additionally to current confinement, in ridge-waveguide (RW) lasers in order to induce injection current independent optical wave-guiding in the lateral direction. Proper choice of the index step and the ridge width leads to laser operation in the lateral lowest-order waveguide mode, which is of major significance for good lateral beam quality.

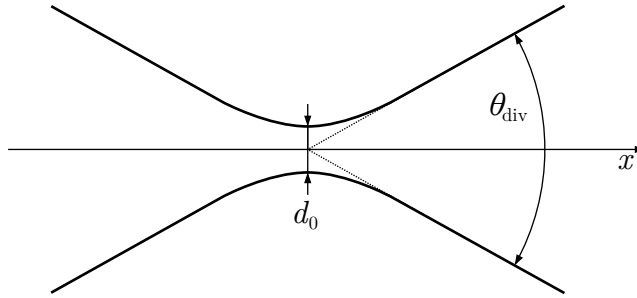
### 2.1.5 Spatial properties of a diode laser beam

During propagation in free space the laser beam diameter alters with increasing distance due to diffraction. In the consequent laser beam caustic a beam waist diameter  $d_0$  and a divergence full angle  $\theta_{\text{div}}$  can be specified, as presented in Fig. 2.5. These two parameters define the beam propagation ratio  $M^2$  through the relation

$$\frac{d_0 \cdot \theta_{\text{div}}}{4} = M^2 \frac{\lambda}{\pi} \quad (2.12)$$

in accordance with [55, Eq. 5.29 and 5.30, p. 226], where  $\lambda$  is the wavelength of radiation. The value of  $M^2$  describes the beam quality of a laser beam. Please note that the beam quality decreases with increasing  $M^2$  value. A Gaussian

**Figure 2.5:**  
Schematic depiction of a laser beam caustic



beam [56, p. 52] represents a diffraction-limited 3-dimensional eigensolution of the wave equation for a laser beam propagating in free space under slowly varying envelope approximation and is characterized by an  $M^2 = 1$ . Real laser beams possess beam propagation ratio  $M^2$  equal to 1 or larger. In this work, the laser beam quality is determined by means of a caustic measurement, which is described in detail in Appendix A.1.

In general, a diode laser beam is simple astigmatic, which means that two principal directions can be distinguished, as shown schematically in Fig. 2.6. A caustic measurement in these two directions, the fast- and the slow-axis to be specific, enables a complemented spatial laser beam characterization. The fast-axis denotes the vertical direction, which is characterized by a large beam divergence due to tight confinement in the waveguide structure defined during epitaxial growth. Hence, optics with high NA values needs to be applied in front of a diode laser in order to collimate its radiation in the fast-axis. In addition, this principal direction is characterized by a nearly diffraction-limited beam quality.

The lateral direction is referred to as the slow-axis. It exhibits smaller beam

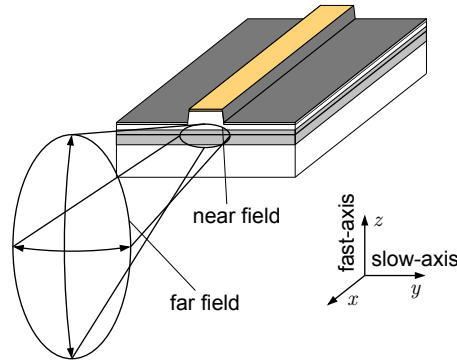


**Figure 2.6:** Schematic depiction of a diode laser and its emission characteristics. The principal directions are fast- and slow-axis

divergence compared to the fast-axis, which, in addition, depends significantly on the lateral resonator design. Narrow emitters, such as for example RW lasers, are characterized by a larger far field distribution than their wide counterparts [45, Sect. 3.3, p. 29]. In addition, due to lateral wave-guiding in the spatial fundamental mode, RW lasers exhibit a nearly diffraction-limited beam quality in the slow-axis. Their maximum output power is limited due to small light emitting area and the consequent catastrophic optical damage [57] or catastrophic optical mirror damage [58, 59] caused by a too high power density. An increase in the maximum output power can be achieved with wider resonator geometries, characteristic for broad area emitters, which, however, is accompanied by a significant degradation of the lateral beam quality.

## 2.2 Requirements for diode lasers intended for frequency doubling

Laser beam available for frequency doubling must possess specific characteristics, in order for the nonlinear process to be efficient. It has been recognized shortly after the first demonstration of second-harmonic generation (SHG) [60], that the efficiency of the frequency conversion process increases with increasing pump intensity [61, 62]. Higher power density in a nonlinear bulk crystal can be reached by a stronger focusing of the pump laser beam, which, however, leads to a shorter effective interaction length due to larger divergence. As has been investigated for a Gaussian pump beam in [21, 63, 64], the optimum focusing changes with the nonlinear crystal length. Later on, it has been also shown theoretically and experimentally, that longitudinal modes in the spectral distribution closely spaced within the acceptance bandwidth of the nonlinear crystal can additionally enhance the frequency doubling efficiency by a factor of two [65, 66]. Furthermore, other experiments have demonstrated, that too wide spectral emission leads to a decrease in conversion efficiency [67, 68]. Finally, the beam quality influence has also been investigated theoretically and experimentally in nonlinear bulk crystals, indicating that increasing beam quality parameter  $M^2$  leads to a less efficient SHG [69, 70, 71, 72, 73].

For efficient frequency conversion process in quasi phase-matched waveguide structures diode lasers emitting nearly diffraction-limited radiation are required.

Good beam quality is of great relevance for high coupling efficiency into waveguide lowest-order mode in addition to its beneficial influence on the normalized SHG conversion efficiency during free beam propagation.

Spectrally narrow-band emission matching the acceptance bandwidth of the nonlinear crystal is crucial for an efficient SHG process. In case of diode lasers this condition can be fulfilled by longitudinal single-mode operation.

The diode laser output power does not influence the normalized SHG conversion efficiency. However, due to the nonlinear character of the interaction, increasing pump power results in an increasing opto-optical conversion efficiency. Additionally, the power level has to be chosen properly to the geometrical configuration of the SHG device applied for frequency doubling, as will be shown in successive chapters of this work.

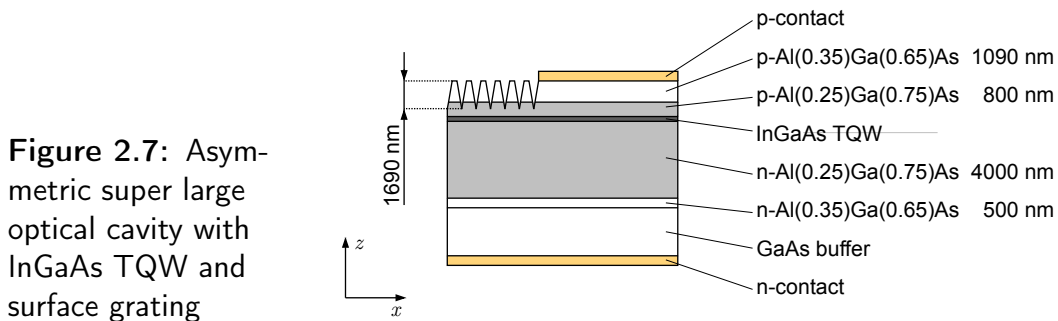
## 2.3 Single emitters design and selection

In recent years diode lasers suitable for direct continuous-wave (CW) frequency doubling have been reported. In the power range of 1 W wavelength stabilized ridge waveguide diode lasers [49, 74, 75, 76, 77, 78] providing laser radiation in spectral and spatial single mode have been demonstrated. For high-power operation, DBR tapered diode lasers [79, 80, 81] and monolithic DFB tapered master-oscillator power-amplifiers (MOPA) [82, 83, 84, 85] have been introduced, which emit nearly diffraction-limited radiation in a longitudinal single-mode at power levels up to 12 W. These lasers are well suited for direct frequency doubling in a single-pass configuration both in bulk crystals and waveguide structures.

In this work, DBR ridge waveguide and DBR tapered diode lasers are applied for frequency doubling in a ridge and a planar waveguide nonlinear crystal, respectively. Below, in Sect. 2.3.1 and 2.3.2, their vertical structure design and resonator concepts are discussed in-depth, respectively.

### 2.3.1 Vertical design

DBR diode lasers applied in this work consist of an asymmetric super large optical cavity grown by metal-organic vapor phase epitaxy (MOVPE) on a (100) GaAs wafer. This vertical structure, introduced already in [81] and depicted



schematically in Fig. 2.7, contains a  $4.8 \mu\text{m}$  thick asymmetric AlGaAs waveguide core, which results in a reduced  $1/e^2$ -level far field angle in the fast-axis of approx.  $25^\circ$ . An InGaAs triple-quantum-well (TQW) is applied to ensure a high confinement factor  $\Gamma$  despite the high asymmetry of the waveguide core, which is incorporated in the structure in order to provide lower absorption, higher conversion efficiency and reduced leakage current. The excellent material quality of the applied epitaxial structure has been confirmed by pulsed measurements on broad area emitters with a variable cavity length, described in detail in [81]. In Tab. 2.1 the most relevant electro-optical parameters resulting from these measurements are presented. Additional information regarding this vertical structure can be found in [81].

$\mathcal{I}_{\text{tr.}} / \text{A/cm}^2$	$\eta_{\text{d}} / 1$	$\Gamma\gamma_0 / \text{cm}^{-1}$	$\alpha_{\text{i}} / \text{cm}^{-1}$
191	0.85	27	1.1

**Table 2.1:** Electro-optical characteristics of the applied epitaxial structure [81]

### 2.3.2 Resonator layout

#### Distributed Bragg reflector

In order to ensure longitudinal single-mode operation, a 1 mm-long 6<sup>th</sup> order distributed Bragg reflector is utilized as rear resonator mirror. The surface grating is realized by i-line photolithography and reactive ion etching [50] to a depth of 1690 nm, as presented in Fig. 2.7. A measurement of the output power from the front and the rear facet of a DBR ridge waveguide laser indicates a DBR grating reflectivity of about 60 % [81].

#### DBR ridge waveguide diode laser

For SHG experiments in a ridge waveguide nonlinear crystal a 4 mm-long DBR ridge waveguide diode laser (DBR-RWL) is applied. It consists of a 3 mm-long index-guided gain section and a 1 mm-long passive DBR section, as presented in Fig. 2.8 (a). I-line photolithography and reactive ion etching [50] to a depth

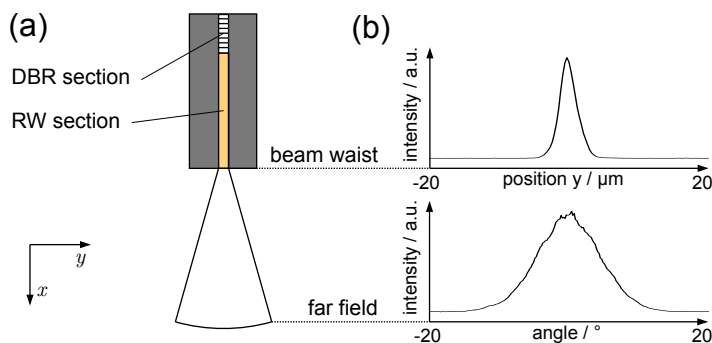


**Figure 2.8:** Top view of a DBR-RWL (a), exemplary intensity distributions (b) in the lateral beam waist and far field at  $P = 1 \text{ W}$

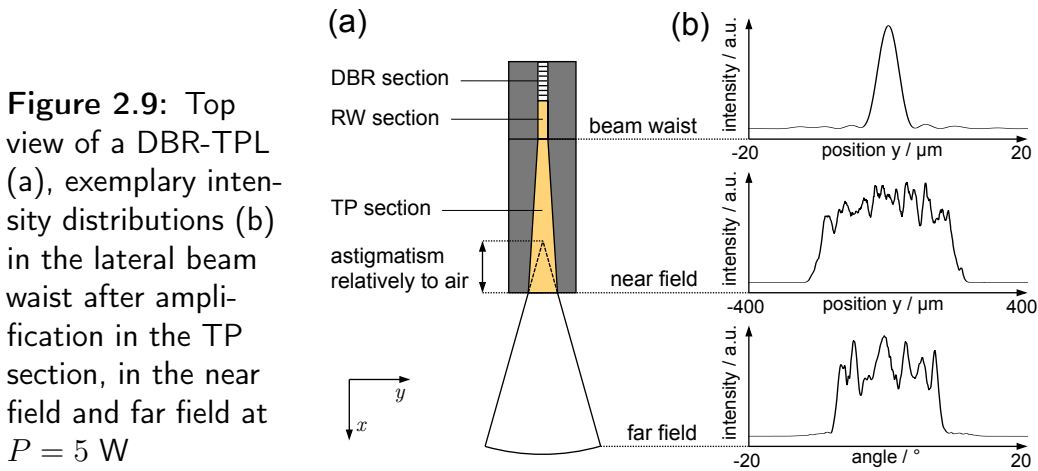
of 1690 nm is applied to fabricate the  $5 \mu\text{m}$ -wide ridge waveguide (RW). The facets of the device are passivated and coated [86], resulting in a front and rear

facet reflectivity of  $R_f = 1\%$  and  $R_r = 0\%$ , respectively.

The lateral intensity distributions measured behind a telescope system of two lenses with a moving slit method at an output power of 1 W are depicted exemplarily in Fig. 2.8 (b). Both beam waist and far field are characterized by a Gaussian-like intensity distribution due to lateral wave-guiding, which results in a good beam quality. In addition, the intensity patterns alter insignificantly with increasing output power. With lasers of this kind a maximum output power in the range of 1 W can be reached [77], which makes them well suited for SHG experiments in nonlinear crystals with ridge waveguide structures.

### DBR tapered diode laser

For high-power SHG experiments in planar waveguides a DBR tapered diode laser (DBR-TPL) schematically depicted in Fig. 2.9 (a) is applied. It consists of a 1 mm-long passive DBR section and two separately contacted active sections: a 1 mm-long index-guided RW section and a 4 mm-long gain-guided tapered (TP) section.



The RW section is  $4\text{ }\mu\text{m}$  wide, and the taper full angle is  $6^\circ$ . Analog treatment of the facets as in case of the DBR-RWL results in a front and rear facet reflectivity of  $R_f = 0.5\%$  and  $R_r = 0\%$ , respectively.

The TP section induces a shift of the lateral beam waist into the diode laser, as depicted in Fig. 2.9 (a), resulting in an output power dependent astigmatism between the slow- and fast-axis. For a 4 mm-long TP section, an astigmatism in the range of 1.4 mm relatively to air needs to be compensated by the optical system. On the other hand however, the TP section leads to a wider front facet and enables, therefore, much higher output powers compared to a DBR-RWL, as will be presented below in Sect. 5.2.2.

The lateral intensity distributions characteristic for a DBR-TPL, which were measured behind a telescope system of two lenses with a moving slit method at an output power of 5 W, are depicted exemplarily in Fig. 2.9 (b). The beam waist of a DBR-TPL laser beam is characterized by a distinct Gaussian-like central lobe and additional considerably lower side lobes. With increasing output

power the power content in the central lobe decreases and the lateral beam diameter determined according to second order moments method (Appendix A.1) increases, whereas the  $1/e^2$ -diameter remains unchanged [79, 81]. The near field distribution represents the lateral intensity pattern on the device facet, which becomes less homogeneous with increasing output power due to increasing filamentation and local spatial hole burning effects [87, 88]. These effects have also similar influence on the lateral far field distribution. In addition, the lateral far field angle decreases and the astigmatism relatively to air increases with increasing output power due to the self-focusing effect [89].



# Chapter 3

## Waveguide structures for SHG into the green spectral region

Application of optical waveguides in nonlinear crystals during second-harmonic generation (SHG) leads to an increase in the conversion efficiency compared to bulk crystals due to light confinement. This confinement, which can be maintained in one or in two directions over the total length of a nonlinear crystal, induces a high intensity inside of the waveguide and, therefore, enables an enhancement of the conversion efficiency.

SHG in optical waveguides has been introduced for the first time around forty years ago [90, 91, 92]. Since then, both channel waveguides [93, 94, 95] as well as planar waveguides [96, 97, 98, 99] have been progressively applied to generate visible laser radiation. Due to intensive research in the fields of doping and phase-matching in nonlinear crystals as well as due to application of ridge waveguides, output powers and opto-optical conversion efficiencies during SHG in excess of 100 mW and 50 %, respectively, were achieved several years ago [100, 101]. Over the last years, output powers have increased beyond 300 mW and 1 W in ridge waveguides [102, 103] and planar waveguides [104, 105], respectively. Recently, state-of-the-art results on SHG in ridge and planar waveguides with maximum output powers in the green spectral region of 466 mW [106] and 1.6 W [107], respectively, have been presented.

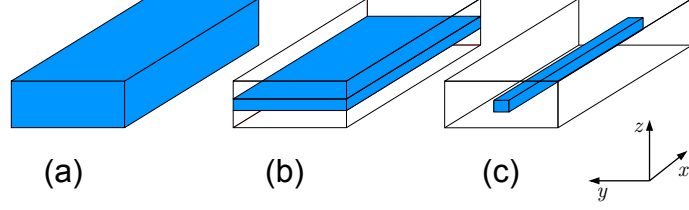
In this chapter the concepts of integrated optics and nonlinear optics are introduced in Sect. 3.1 and Sect. 3.2, respectively. In the former section the mode discretization, the mode field distributions and propagation loss, in the latter the SHG process, quasi phase-matching (QPM) and corresponding conversion efficiency and power dependency are discussed. Finally, in Sect. 3.3 the waveguide structures, applied in this work for frequency doubling of diode lasers, are described.

### 3.1 Introduction to integrated optics

Dielectric waveguides confine light by means of multiple total internal reflexions at the interface between waveguide core and cladding [48, p. 193]. For this

purpose the refractive index of core  $n_g$  needs to be larger than the refractive index of cladding  $n_c$ . A planar waveguide is composed of a core layer enclosed by two cladding layers as presented in Fig. 3.1 (b). Hence, the light is confined

**Figure 3.1:**  
Schematic depiction  
of a bulk crystal (a),  
a planar waveguide  
(b) and a channel  
waveguide (c)



in one direction and can propagate freely in other two directions. In a channel waveguide cladding interfaces in an additional direction are present, as can be observed in Fig. 3.1 (c) and the light is confined in two directions. Thus, a kind of an optical wire is created.

The propagation of radiation in an optical waveguide can be described by a ray optic model, which provides a simplified approach to the understanding of waveguide modes discretization based on the constructive interference principle [44, Fig. 7.2, p. 148]. The electro-magnetic model, which requires the solution of wave equation in the core and cladding region while taking boundary conditions into consideration, provides, additionally to propagation constants, the electric field distributions. These are relevant, for example, for the calculation of coupling efficiency into a particular waveguide mode.

### 3.1.1 Propagation constant and effective refractive index

A discrete planar waveguide mode  $m$  is characterized by a discrete propagation constant  $\beta^{(m)}$ , which is defined as

$$\beta^{(m)} = N^{(m)} \cdot \frac{\omega}{c_0} \quad (3.1)$$

with accordance to [108, Eqs. 2.4 and 2.9, p. 10 and 11], where  $m = 0, 1, 2, \dots$  denotes the corresponding mode order,  $N^{(m)}$  is the corresponding effective refractive index,  $\omega$  is the radiation frequency and  $c_0$  is the light velocity in vacuum.

Conform to the electro-magnetic model the following eigenvalue equations corresponding to [44, Eqs. 7.59 and 7.60, p. 167] have to be solved in order to calculate the effective refractive index  $N^{(m)}$  in a symmetric planar waveguide structure with a height  $h$ :

$$0 = h \frac{\omega}{c_0} \sqrt{n_g^2 - (N^{(m)})^2} - m\pi - 2 \arctan \left( \sqrt{\frac{(N^{(m)})^2 - n_c^2}{n_g^2 - (N^{(m)})^2}} \right) \quad (3.2)$$

for transverse electric (TE) modes and

$$0 = h \frac{\omega}{c_0} \sqrt{n_g^2 - (N^{(m)})^2} - m\pi - 2 \arctan \left( \left( \frac{n_g}{n_c} \right)^2 \sqrt{\frac{(N^{(m)})^2 - n_c^2}{n_g^2 - (N^{(m)})^2}} \right) \quad (3.3)$$

for transverse magnetic (TM) modes. Solutions in the range  $n_g > N^{(m)} > n_c$  correspond to modes propagating in the waveguide structure [108, Fig. 2.5, p. 15].

In channel waveguides, in which the radiation is confined in two directions, a discrete waveguide mode  $mn$  is characterized by a propagation constant  $\beta^{(mn)}$  defined as

$$\beta^{(mn)} = N^{(mn)} \cdot \frac{\omega}{c_0}, \quad (3.4)$$

where  $m = 0, 1, 2, \dots$  and  $n = 0, 1, 2, \dots$  denote the corresponding mode order in the vertical and lateral direction, respectively, and  $N^{(mn)}$  is the corresponding effective refractive index.

The analytical calculation of the effective refractive index in channel waveguides is, in general, possible only by means of approximate techniques. In this work, an effective index approximation described in detail in [44, p. 183] is used for this purpose.

### 3.1.2 Electric field distributions

In case of planar waveguides, solving of the wave equation in the core and cladding region while taking boundary conditions into consideration, enables an analytical calculation of the electric field distribution  $\mathfrak{E}^{(m)}(z)$  for a given waveguide mode  $m$ , as has been presented for instance in [44, p. 165].

The characterization of a channel waveguide with regard to its discrete modes requires a solution of a 2-dimensional problem, which cannot be accomplished analytically [108, p. 15]. It is for this reason, that real channel waveguide structures, such as for example ridge waveguides, are analyzed by numerical simulations. For the purpose of this work, a commercial mode solver software FIMMWAVE from Photon Design is applied in order to determine the electric field distributions of the channel waveguide modes  $\mathfrak{E}^{(mn)}(y, z)$ . Mode distributions  $\mathfrak{E}^{(m)}(z)$  for planar waveguide structures are also calculated with this software tool. Please note, that in the coordinate system chosen,  $x$  represents the propagation direction (Fig. 3.1).

### 3.1.3 Loss

#### Input coupling loss

The coupling efficiency into the  $mn$  mode of a channel waveguide can be calculated mathematically by the overlap integral

$$\eta_c^{(mn)} = \frac{\left| \iint \mathcal{E}(y, z) \mathfrak{E}^{(mn)}(y, z)^* dydz \right|^2}{\iint |\mathcal{E}(y, z)|^2 dydz \iint |\mathfrak{E}^{(mn)}(y, z)|^2 dydz} \quad (3.5)$$

in accordance with [109, Eq. (5.4.6), p. 242], where  $\mathcal{E}(y, z)$  is the electric field distribution of the incident laser beam on the waveguide facet and  $\mathfrak{E}^{(mn)}(y, z)$  is

the electric field distribution of the  $mn$  waveguide mode. For a planar waveguide a 1-dimensional coupling efficiency can be defined analog to Eq. (3.5)

$$\eta_c^{(m)} = \frac{\left| \int \mathcal{E}(z) \mathfrak{E}^{(m)}(z)^* dz \right|^2}{\int |\mathcal{E}(z)|^2 dz \int |\mathfrak{E}^{(m)}(z)|^2 dz} \quad (3.6)$$

with electric field distribution of the laser radiation on the input facet  $\mathcal{E}(z)$  and the electric field distribution  $\mathfrak{E}^{(m)}(z)$  of the waveguide mode  $m$ .

### Propagation loss

Power of an optical mode propagating in a waveguide structure experiences attenuation due to waveguide optical loss. In dielectric waveguides, additionally to the intrinsic material absorption  $\alpha$ , which is present in bulk crystals as well, scattering of the electro-magnetic radiation resulting from roughness of the waveguide structure accounts for the propagation loss. The decrease in the intensity  $\mathcal{J}$  along the propagation direction  $x$  can be described by Lambert-Beer law defined as

$$\mathcal{J}(x) = \mathcal{J}(0)e^{-\delta x} \quad (3.7)$$

with accordance to e.g. [110, Eq. 7.16, p. 195], where  $\delta$  [1/cm] is the propagation loss coefficient,  $\mathcal{J}(0)$  is the intensity present at the beginning of the waveguide,  $\mathcal{J}(x)$  is the intensity at the distance  $x$ . The optical loss in waveguide structures can be also described by  $\delta_{dB}$  [dB/cm] [100, 111], which is defined as

$$\delta_{dB} x = -10 \log \frac{\mathcal{J}(x)}{\mathcal{J}(0)}. \quad (3.8)$$

A following relation between  $\delta$  and  $\delta_{dB}$  can be determined according to [44, p. 197, Eq. 8.29]:

$$\delta = \frac{\ln(10)}{10} \cdot \delta_{dB}. \quad (3.9)$$

### Fresnel loss

Fresnel reflexion at each facet in an absence of an anti-reflexion (AR) coating accounts for additional loss during radiation transition through a dielectric waveguide. The corresponding reflexion  $R_{\text{facet}}$  at a waveguide facet can be described by the Fresnel equations [48, p. 114, 115, 120]

$$R_{\text{facet},\parallel} = \left( \frac{n_t \cos(\theta_i) - n_i \cos(\theta_t)}{n_t \cos(\theta_i) + n_i \cos(\theta_t)} \right)^2 \quad (3.10)$$

and

$$R_{\text{facet},\perp} = \left( \frac{n_i \cos(\theta_i) - n_t \cos(\theta_t)}{n_i \cos(\theta_i) + n_t \cos(\theta_t)} \right)^2 \quad (3.11)$$

for electric field oscillating parallel and perpendicular to the incidence plane, respectively, where  $n_i$  and  $n_t$  are the refractive indices of the medium on each side of the interface,  $\theta_i$  is the incidence angle and  $\theta_t$  is the angle of the transmitted (and refracted) wave, which can be calculated according to Snell's law [48, p. 101]

$$n_i \cdot \sin(\theta_i) = n_t \cdot \sin(\theta_t). \quad (3.12)$$

The corresponding Fresnel transmission is given by the relation:

$$T_{\text{facet}} = 1 - R_{\text{facet}}. \quad (3.13)$$

## 3.2 Nonlinear optics

Nonlinear optics comprises phenomena which occur as a consequence of an optical properties modification in matter, induced by the presence of light. It describes interactions between light and matter, which occur when the material reaction depends nonlinearly upon the optical field strength. In general, only laser light provides intensities high enough to effect nonlinear response. Consequently, the observation of SHG in crystalline quartz by Franken *et al.* in 1961 [60], which is considered as the beginning of the field of nonlinear optics [112, p. 1], occurred shortly after the demonstration of laser emission by Maiman in 1960 [1].

In this section the principles of nonlinear optics are presented and the main focus is laid on the SHG process. In Sect. 3.2.1 the general aspects of nonlinear polarization are discussed. Subsequently, the theoretical description of SHG for plane waves is presented in Sect. 3.2.2, including the system of coupled equations, first derived by Armstrong *et al.* [61] and Achmanov and Chochlov [62]. In Sect. 3.2.3 the principle of quasi phase-matching (QPM) for SHG process in comparison to birefringent phase-matching (BPM) is discussed. Finally, the SH power dependency on the fundamental power including the normalized SHG conversion efficiency in planar and channel waveguides is provided in Sect. 3.2.4.

### 3.2.1 Dielectric polarization and nonlinear coefficient

The reaction of matter to incident light is described by polarization  $\vec{\mathcal{P}}(t)$ , which represents electric dipole moment per unit volume. In case of linear optics, the induced polarization depends linearly on the electric field strength  $\vec{\mathcal{E}}(t)$  according to [112, p. 591, Eq. (A.6a)] and is given for an instantaneously responding medium by the relation

$$\vec{\mathcal{P}}(t) = \epsilon_0 \underline{\underline{\chi}}^{(1)} \vec{\mathcal{E}}(t). \quad (3.14)$$

The constant of proportionality consists of the vacuum permittivity  $\epsilon_0$  and the first-order relative electric susceptibility  $\chi_{ij}^{(1)}$  in form of a second-rank tensor. For large electric fields in order to describe the nonlinear response

the polarization  $\vec{\mathcal{P}}(t)$  needs to be expressed as a power series in electric field strength  $\vec{\mathcal{E}}(t)$ , which results in a relation

$$\vec{\mathcal{P}}(t) = \epsilon_0 \underline{\underline{\chi}}^{(1)} \vec{\mathcal{E}}(t) + \epsilon_0 \underline{\underline{\chi}}^{(2)} \vec{\mathcal{E}}(t) \vec{\mathcal{E}}(t) + \dots \quad (3.15)$$

$$= \vec{\mathcal{P}}^{(1)}(t) + \vec{\mathcal{P}}^{(2)}(t) + \dots, \quad (3.16)$$

where  $\chi_{ijk}^{(2)}$  is the second-order electric susceptibility in form of a third-rank tensor. In further course the second-order polarization of the form

$$\vec{\mathcal{P}}^{(2)}(t) = \epsilon_0 \underline{\underline{\chi}}^{(2)} \vec{\mathcal{E}}(t) \vec{\mathcal{E}}(t) \quad (3.17)$$

will be considered. An extensive discussion of nonlinear optical phenomena including the third-order susceptibility can be found for instance in [113].

In general, due to loss and dispersion, the second-order susceptibility components  $\chi_{ijk}^{(2)}$  are complex functions depending on the optical frequencies of the electric fields participating in the interaction. However, if optical frequencies lying far below the resonance frequency of the nonlinear material are considered, the second-order susceptibility is practically independent of frequency, the medium responds essentially instantaneously to applied field and can be regarded as lossless [112, Sect. 1.5, p. 33]. Under these circumstances, the relation from Eq. (3.17) with a constant value of  $\chi_{ijk}^{(2)}$  is justified.

For the contracted notation, known from the literature, the nonlinear coefficient  $d_{ijk}$  is defined:

$$d_{ijk} = \frac{1}{2} \chi_{ijk}^{(2)}. \quad (3.18)$$

Due to intrinsic permutation symmetry [112, p. 34] the nonlinear coefficient  $d_{ijk}$  is symmetrical in two last indices, which enables a contracted notation based on the principle of consolidation of the indices  $j$  and  $k$  to an index  $l$  according to the schema

$$\begin{array}{rccclll} jk: & 11 & 22 & 33 & 23,32 & 31,13 & 12,21 \\ l: & 1 & 2 & 3 & 4 & 5 & 6 \end{array} ,$$

which results in a matrix

$$d = \begin{bmatrix} d_{11} & d_{12} & d_{13} & d_{14} & d_{15} & d_{16} \\ d_{21} & d_{22} & d_{23} & d_{24} & d_{25} & d_{26} \\ d_{31} & d_{32} & d_{33} & d_{34} & d_{35} & d_{36} \end{bmatrix} \quad (3.19)$$

with 18 independent elements. In addition, Kleinman's symmetry condition requires that the indices  $ijk$  permute freely [112, p. 38], which leads to 10 independent components of the nonlinear coefficient. Further reduction of independent components is possible for diverse crystal classes due to structural symmetry [114, p. 26], as will be presented on the example of MgO doped lithium niobate in Sect. 3.3.1.

By reason of the contracted notation Eq. 3.17 can be written down as a matrix equation in the form:

$$\begin{bmatrix} \mathcal{P}_x^{(2)}(t) \\ \mathcal{P}_y^{(2)}(t) \\ \mathcal{P}_z^{(2)}(t) \end{bmatrix} = 2\epsilon_0 \begin{bmatrix} d_{11} & d_{12} & d_{13} & d_{14} & d_{15} & d_{16} \\ d_{16} & d_{22} & d_{23} & d_{24} & d_{14} & d_{12} \\ d_{15} & d_{24} & d_{33} & d_{23} & d_{13} & d_{14} \end{bmatrix} \cdot \begin{bmatrix} \mathcal{E}_x^2(t) \\ \mathcal{E}_y^2(t) \\ \mathcal{E}_z^2(t) \\ 2\mathcal{E}_y(t)\mathcal{E}_z(t) \\ 2\mathcal{E}_x(t)\mathcal{E}_z(t) \\ 2\mathcal{E}_x(t)\mathcal{E}_y(t) \end{bmatrix}. \quad (3.20)$$

If the polarization and propagation directions of participating waves are known, an effective nonlinear coefficient  $d_{\text{eff}}$  can be calculated, e.g. according to Midwinter and Warner [115] for a birefringent phase-matching (Sect. 3.2.3), and the Eq. (3.17) can be denoted with scalar values:

$$\mathcal{P}^{(2)}(t) = 2\epsilon_0 d_{\text{eff}} \mathcal{E}^2(t). \quad (3.21)$$

### 3.2.2 Second-harmonic generation

In general, the electric field from Eq. (3.21) can comprise components at diverse frequencies leading to multiple nonlinear interactions, such as for example sum-frequency generation [112, Eq. 1.2.7, p. 7]. For efficient energy transfer, every of these interactions requires a certain phase-matching, which, in general, can be fulfilled only for one of them at a time. The focus of this work lies on the second-harmonic generation.

In further course a monochromatic plane wave

$$\mathcal{E}_1(x, t) = \mathcal{A}_1 \cdot \cos(k_1 x - \omega_1 t + \phi_1) \quad (3.22)$$

propagating along the  $x$  axis with the electric field amplitude  $\mathcal{A}_1$ , propagation constant  $k_1$ , frequency  $\omega_1$  and phase  $\phi_1$  is considered according to [61, Eq. (4.4), p. 1927]. With  $\mathcal{E}_1(x, t)$  from Eq. (3.22) the nonlinear polarization from Eq. (3.21) reads

$$\mathcal{P}^{(2)}(x, t) = 2\epsilon_0 d_{\text{eff}} [\mathcal{A}_1 \cos(k_1 x - \omega_1 t + \phi_1)]^2 \quad (3.23)$$

in accordance to [116, Eq. (2.3), p. 23] and can be rewritten to

$$\mathcal{P}^{(2)}(x, t) = 2\epsilon_0 d_{\text{eff}} \frac{\mathcal{A}_1^2}{2} [1 + \cos(2k_1 x - 2\omega_1 t + 2\phi_1)] \quad (3.24)$$

through a simple trigonometrical transformation. This formulation shows clearly the presence of an optical rectification term and of a second-harmonic term. The latter can become a source of a new monochromatic wave

$$\mathcal{E}_2(x, t) = \mathcal{A}_2 \cdot \cos(k_2 x - \omega_2 t + \phi_2) \quad (3.25)$$

according to a corresponding inhomogeneous wave equation [112, Eq. 1.1.5, p. 4]

$$\frac{\partial^2}{\partial x^2} \mathcal{E}_2(x, t) - \frac{n_2^2}{c_0^2} \frac{\partial^2}{\partial t^2} \mathcal{E}_2(x, t) = \frac{1}{\epsilon_0 c_0^2} \frac{\partial^2}{\partial t^2} \mathcal{P}^{(2)}(x, t). \quad (3.26)$$

In other words, the second-order polarization  $\mathcal{P}^{(2)}(x, t)$  effected by the electric field  $\mathcal{E}_1(x, t)$  oscillating at a frequency  $\omega_1$  drives another electric field  $\mathcal{E}_2(x, t)$  at a frequency  $\omega_2 = 2\omega_1$ . Throughout this work,  $\mathcal{E}_1(x, t)$  and  $\mathcal{E}_2(x, t)$  will be referred to as fundamental and second-harmonic (SH) wave, respectively. The interaction of both waves during SHG process can be described by a system of coupled equations for electric field amplitudes, originally derived in [61, p. 1930] and [62, p. 160],

$$\frac{d\mathcal{A}_0}{dx} = \Delta k - \left(2\sigma_1\mathcal{A}_2 - \sigma_2\frac{\mathcal{A}_1^2}{\mathcal{A}_2}\right) \cos \mathcal{A}_0 \quad (3.27)$$

$$\frac{d\mathcal{A}_1}{dx} = -\sigma_1\mathcal{A}_1\mathcal{A}_2 \sin \mathcal{A}_0 \quad (3.28)$$

$$\frac{d\mathcal{A}_2}{dx} = \sigma_2\mathcal{A}_1^2 \sin \mathcal{A}_0 \quad (3.29)$$

with  $\mathcal{A}_0 = 2\phi_1 - \phi_2 + \Delta k x$ ,  $\sigma_1 = \omega_1 d_{\text{eff}}/c_0 n_1$ ,  $\sigma_2 = \omega_1 d_{\text{eff}}/c_0 n_2$ , where  $\Delta k$  is the phase mismatch parameter defined as

$$\Delta k = 2k_1 - k_2, \quad (3.30)$$

according to [61, p. 1930]. In order to calculate the intensity of each wave the relation

$$\mathcal{J} = \frac{nc_0\epsilon_0}{2}\mathcal{A}^2 \quad (3.31)$$

in accordance to [112, p. 12] is applied.

### 3.2.3 Quasi phase-matching

In order to efficiently transfer energy between waves participating in a nonlinear interaction their relative phase needs to be maintained constant over the propagation length in the nonlinear medium [117]. It means that in case of plane waves the phase mismatch parameter  $\Delta k$  from Eq. (3.30) needs to be minimized:

$$\Delta k = 0, \quad (3.32)$$

which can be achieved, when the refractive indices of the fundamental and SH wave are equal to each other:

$$n_2 = n_1. \quad (3.33)$$

By nature, this condition is not fulfilled due to material dispersion [48, Sect. 3.5.1, p. 67], which induces the phase velocity difference and the consequent phase shift. Multiple methods to compensate phase mismatch have been proposed in the past, among which the birefringent phase-matching (BPM) and the quasi phase-matching (QPM) have found the most widespread application.

Although QPM was proposed by Armstrong *et al.* [61, Fig. 10 a, p. 1937] and Franken and Ward [113, Sect. III.2, p. 29] at the same time as the BPM (described e.g. in [116, p. 57]), it did not find widespread application until the end of 1980s due to technological difficulties in lithography controlled patterning of nonlinear media [118, 119, 120]. Since then it has been investigated theoretically

in-depth [121, 122, 123, 124] and it has become the phase-matching method of choice due to its numerous advantages.

In comparison to BPM, QPM enables phase-matching for arbitrary wavelength combinations at an arbitrary temperature in the transparency range of the nonlinear medium. Furthermore, through the free choice of wave polarization and propagation direction, it allows to activate the largest nonlinear coefficient tensor component  $d_{ij}$  and it provides a walk-off free interaction. In addition, QPM opens further possibilities regarding the shaping of SHG tuning curves and broadening of spectral and thermal acceptance bandwidths, as has been presented, for instance, in [125, 126, 127]. The main disadvantage of QPM, on the other hand, is its limitation to provide phase-matching for arbitrarily small wavelengths due to technological issues [128, 129].

### QPM principle

In a medium where the phase-matching is not provided the energy flow between the fundamental and the second-harmonic wave depends on their continuously and periodically changing relative phase difference. The energy transfer from

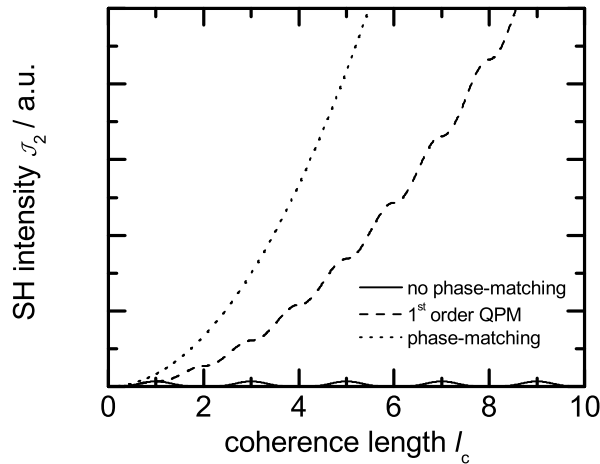


**Figure 3.2:** Comparison of second-harmonic wave growth along the propagation direction  $x$  for no phase-matching (solid curve), QPM (dashed curve) and phase-matching (dotted curve)

one wave to another occurs along a coherence length  $l_c$ , after which the sign of the phase difference and therefore also the energy flow direction changes (Fig. 3.2 - solid curve). The coherence length is defined e.g. in [117] as

$$l_c = \frac{\pi}{|\Delta k|} \quad (3.34)$$

with the phase mismatch parameter  $\Delta k$  from Eq. (3.30). QPM is based on a periodical modification in the nonlinear medium, which corrects the relative phase at fixed intervals and does not provide full matching of phase velocities along the propagation direction [117]. Very effective for this purpose is the modulation of the sign or magnitude of the nonlinear coefficient  $d_{\text{eff}}$  [123], which can be achieved through alternating periodically oriented ferroelectric domains [118, 119, 120] with a period  $\Lambda$ , where

$$\Lambda = 2 \cdot l_c. \quad (3.35)$$

The inversion of the polarization direction at every coherence length  $l_c$  leads to a  $\pi$  phase shift in the generated second-harmonic wave [116, Fig. 2.41, p. 76], which results in continuous but not constant energy transfer from the fundamental to second-harmonic wave over the whole crystal length (Fig. 3.2 - dashed curve). Since the energy flow is not constant, QPM is characterized by a reduced conversion efficiency compared to persistent phase-matching (Fig. 3.2 - dotted curve). The corresponding effective nonlinear coefficient for a first order QPM grating can be calculated according to [56, p. 415] with

$$d_{\text{eff,QPM}} = \frac{2}{\pi} \cdot d_{\text{eff}}, \quad (3.36)$$

where  $d_{\text{eff}}$  is the material specific nonlinear coefficient for given radiation polarization and propagation direction. That being so, the resulting phase mismatch parameter for plane waves, defined as

$$\Delta k_{\text{QPM}} = \Delta k + \frac{2\pi}{\Lambda}, \quad (3.37)$$

needs to be minimized in order to maximize the SHG conversion efficiency.

### QPM tolerances

A deviation from the QPM condition presented in Eq. (3.32) leads to a distorted energy flow between the fundamental and the SH wave and therefore to a lower SH intensity  $\mathcal{J}_2$  accumulated over the entire interaction length  $L_{\text{QPM}}$  in the given QPM structure. The corresponding SH intensity  $\mathcal{J}_2$  distribution can be determined by solving the system of coupled equations from Eqs. (3.27 - 3.29) for an alternating parameter  $\Delta k_{\text{QPM}}$ . The resulting normed SH intensity  $\mathcal{J}_2/L_{\text{QPM}}^2$  in dependence on the  $\Delta k_{\text{QPM}}L_{\text{QPM}}$ , which is thereby independent of the QPM region length  $L_{\text{QPM}}$ , is depicted in Fig. 3.3. This distribution corresponds to the sinc<sup>2</sup> function introduced e.g. in [116, Eq. 2.21, p. 34] and is valid for nonlinear interactions characterized by a low conversion efficiency below 10 % (compare Sect. 3.2.4). The presented dependency shows clearly,

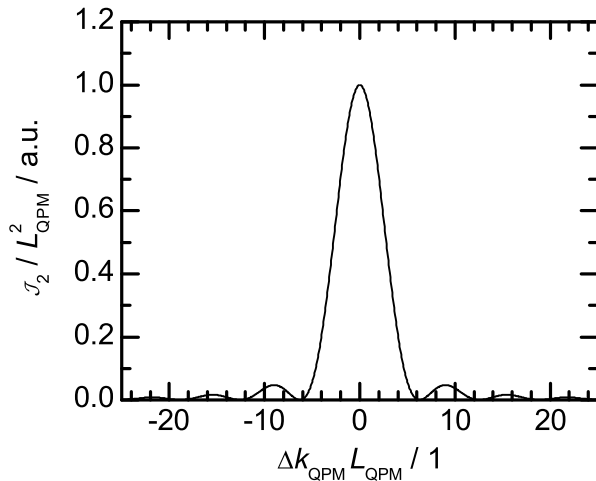


**Figure 3.3:**  
Normed SH intensity  $\mathcal{J}_2/L_{\text{QPM}}^2$  for plane-waves vs.  $\Delta k_{\text{QPM}}L_{\text{QPM}}$  parameter

that for plane-waves the generated SH intensity  $\mathcal{J}_2$  increases quadratically

with the interaction length  $L_{\text{QPM}}$ . However, additionally to the increase in the conversion efficiency, also the sensitivity to detuning from the optimum phase mismatch parameter  $\Delta k_{\text{QPM}} = 0$  increases due to the constant product  $\Delta k_{\text{QPM}} L_{\text{QPM}}$  depicted on the abscissa of Fig. 3.3. This means that in case of longer nonlinear crystals, the phase mismatch parameter  $\Delta k_{\text{QPM}}$  needs to be adjusted and maintained with a higher accuracy.

The refractive index  $n_j$  and therefore also the propagation constant  $k_j$  for the fundamental and SH wave depend on the crystal temperature  $T$  and fundamental wavelength  $\lambda_1$ . In addition, the QPM period  $\Lambda$  is affected by the temperature of the nonlinear crystal. Hence, the phase mismatch parameter  $\Delta k_{\text{QPM}}$  alters also with the crystal temperature  $T$  and the fundamental radiation wavelength  $\lambda_1$  and the corresponding relation from Eq. (3.37) can be rewritten to

$$\Delta k_{\text{QPM}}(\lambda_1, T) = 2k_1(\lambda_1, T) - k_2(\lambda_1, T) + \frac{2\pi}{\Lambda(T)}. \quad (3.38)$$

Please note, that here a homogeneous distribution of temperature  $T$  in the nonlinear crystal is preconditioned. Both parameters, the crystal temperature and the fundamental wavelength, need to be adjusted and controlled during the SHG process in order to ensure a maximum conversion efficiency. In general, the detuning ratio from the optimal phase mismatch parameter  $\Delta k_{\text{QPM}}$  due to refractive index change with temperature is one order of magnitude larger than due to thermal expansion of the QPM period  $\Lambda$  [127].

### QPM condition in waveguide structures

For interactions in optical waveguides the phase mismatch parameter reads

$$\Delta k_{\text{QPM}} = 2\beta_1 - \beta_2 + \frac{2\pi}{\Lambda}, \quad (3.39)$$

where  $\beta_j = N_j \omega_j / c_0$  is the waveguide lowest-order mode propagation constant,  $N_j$  is the effective refractive index,  $\Lambda$  is the QPM period with  $j = 1$  for fundamental,  $j = 2$  for SH wave.

For channel waveguides the SHG conversion efficiency is maximized, when the phase mismatch parameter from Eq. (3.39) is minimized:

$$\Delta k_{\text{QPM}} = 0. \quad (3.40)$$

In planar waveguides the optimum phase mismatch parameter depends upon focusing strength of a Gaussian beam. The maximum SHG conversion efficiency is reached, when the condition

$$\Delta k_{\text{QPM}} = \sigma_{\max, \xi} \frac{2 \cdot \xi}{L_{\text{QPM}}} \quad (3.41)$$

is fulfilled, with  $\xi$  and  $\sigma_{\max, \xi}$  defined below in Eq. (3.52) and Eq. (3.54), respectively.

### QPM errors

The effective nonlinear coefficient  $d_{\text{eff,QPM}}$  for an ideal first order QPM structure is defined according to Eq. (3.36). However, in real QPM devices deviations of the domain length from the coherence length  $l_c$  may occur [130, 131]. Such irregularity induces phase errors and leads to a decrease in the effective nonlinear coefficient  $d_{\text{eff,QPM}}$  and therefore also limits the conversion efficiency for a given nonlinear interaction. In [123] the quantitative influence of QPM grating errors on the conversion efficiency was studied in detail. As a result of theoretical evaluation a number of possible cases was addressed, for which the corresponding results are presented here.

Missing reversals after a poling process are one of the fabrication problems. The nominal conversion efficiency  $\eta_{\text{ideal}}$  of a nonlinear process in a QPM structure is reduced due to missing domains as

$$\eta = \eta_{\text{ideal}} \cdot (1 - 2f)^2, \quad (3.42)$$

where  $f$  denotes the fraction of domains with an opposite polarization than intended. In order to reach a conversion efficiency  $\eta > 95\%$ , a fraction  $f < 1.3\%$  must be ensured.

In case of random domain border errors it can be distinguished between period errors and duty cycle errors. For QPM structures defined e.g. by lithography, only the latter case is relevant, since the average position of boundaries is maintained with uniform accuracy across the entire device. However, local boundary errors may still occur and the nominal conversion efficiency  $\eta_{\text{ideal}}$  is reduced according to

$$\eta = \eta_{\text{ideal}} \cdot \exp\left(-\frac{\pi^2 \sigma_{l_c}^2}{2 l_c^2}\right), \quad (3.43)$$

where  $l_c$  is the coherence length and  $\sigma_{l_c}$  is its standard deviation. In this case in order to achieve a conversion efficiency  $\eta > 95\%$ , the ratio  $\sigma_{l_c}/l_c < 0.10$  must be ensured.

#### 3.2.4 SH power dependency on the fundamental power

The system of coupled equations describing the energy flow between fundamental and SH plane waves during frequency doubling (Eqs. (3.27-3.29)) has been solved in the past, resulting in a direct SH power dependence on the fundamental power given by the SHG conversion efficiency [21, 114]. A corresponding dependence has also been derived for Gaussian beams [21, 132], enabling to calculate the normalized SHG conversion efficiency in dependence on the fundamental laser beam parameters and geometric properties of the nonlinear crystal.

In this section the theoretical considerations required to determine the SH power dependency on the fundamental power during frequency doubling of a Gaussian beam in a planar and a channel waveguide are presented.

### Theoretical relation between SH and fundamental power

The SH power dependence on the fundamental power is defined as

$$P_2 = \eta_{\text{SHG}}(P_1) P_1 \quad (3.44)$$

similarly to [116, Eq. 2.25, p. 38], where  $P_2$  is the SH power at the end of the nonlinear crystal,  $\eta_{\text{SHG}}$  is the SHG conversion efficiency and  $P_1$  is the fundamental power coupled into the nonlinear crystal. Due to the nonlinear character of the interaction, the SHG conversion efficiency  $\eta_{\text{SHG}}$  is not constant and increases with increasing fundamental power  $P_1$ . The scope of this work lies on a high conversion efficiency during the SHG process, which involves a strong depletion of the fundamental wave. Therefore, the SHG conversion efficiency

$$\eta_{\text{SHG}}(P_1) = \bar{\eta}_{\text{SHG}} P_1, \quad (3.45)$$

derived theoretically for plane waves as well as for Gaussian beams in the undepleted case [21], will not be applied. Instead, an empiric relation

$$\eta_{\text{SHG}}(P_1) = \tanh^2 \left( \sqrt{\bar{\eta}_{\text{SHG}} P_1} \right), \quad (3.46)$$

which has until now been only proven analytically for plane waves [114, p. 87] (channel waveguides), but has been experimentally observed in bulk crystals [9] and planar waveguides [104, 133] as well, will be applied in order to calculate the SH power dependence on the fundamental power. The normalized SHG conversion efficiency  $\bar{\eta}_{\text{SHG}}$  represents a constant parameter characteristic for a given SHG device, which is independent of fundamental power  $P_1$ . The definition of this parameter for a channel and planar waveguide is presented in the following section.

Both functions from Eq. 3.45 and 3.46 are presented in Fig. 3.4 in dependence on the product  $\bar{\eta}_{\text{SHG}} P_1$ . In contrast to the  $\tanh^2$  relation from Eq. (3.46), the

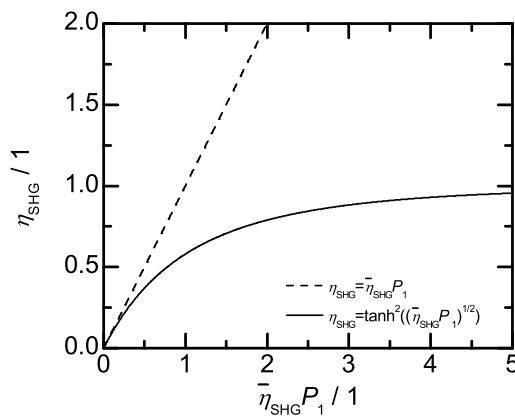


**Figure 3.4:** SHG conversion efficiency  $\eta_{\text{SHG}}$  dependence on the product of normalized SHG conversion efficiency  $\bar{\eta}_{\text{SHG}}$  and fundamental power coupled into the nonlinear crystal  $P_1$

linear relation from Eq. (3.45) does not take the fundamental power depletion into account, which results in a good agreement with the  $\tanh^2$  function only for low SHG conversion efficiencies  $\eta_{\text{SHG}}$  in the range of 10 %. Furthermore, for  $\bar{\eta}_{\text{SHG}} P_1 > 1$  the SHG conversion efficiency would exceed 100 %, which violates the law of conservation of energy [116, p. 39].

### Normalized SHG conversion efficiency

The frequency doubling of a Gaussian beam in a nonlinear crystal with a planar waveguide structure was investigated theoretically by Fluck [132]. The corresponding normalized SHG conversions efficiency  $\bar{\eta}_{\text{SHG}}$  is defined as

$$\bar{\eta}_{\text{SHG}} = \frac{8\pi^2}{\epsilon_0 c_0 \lambda_1^2} \frac{d_{\text{eff,QPM}}^2}{N_2 N_1^2} \frac{1}{S_z} \sqrt{\frac{2N_1}{\lambda_1}} L_{\text{QPM}}^{3/2} e^{-\alpha_+ L_{\text{cr}}} g_1 \quad (3.47)$$

with

$$g_1 = g(\sigma, \beta, \kappa, \xi, \mu) = \frac{\pi^2}{\xi^{\frac{3}{2}}} e^{\mu \Delta \alpha L_{\text{cr}}} F(\sigma, \beta, \kappa, \xi, \mu), \quad (3.48)$$

$$F(\sigma, \beta, \kappa, \xi, \mu) = \frac{2}{\sqrt{\pi}} \int_{-\infty}^{+\infty} ds |H(\sigma + 4\beta s, \kappa, \xi, \mu)|^2 e^{-4s^2}, \quad (3.49)$$

$$H(\sigma', \kappa, \xi, \mu) = \frac{1}{2\pi} \int_{-\xi(1-\mu)}^{+\xi(1+\mu)} d\tau' \frac{e^{-\kappa\tau'} e^{i\sigma'\tau'}}{\sqrt{1+i\tau'}}. \quad (3.50)$$

Please note, that in general, the QPM region length  $L_{\text{QPM}}$  and the waveguide length  $L_{\text{cr}}$  can differ. In Eq. (3.47),  $N_1$  and  $N_2$  are the effective refractive indices in the planar waveguide structure for fundamental and SH wave, respectively,  $S_z$  is the effective cross-section [108, Eq. 3.32, p. 42] between the fundamental and the SH electric field distributions  $\mathfrak{E}_1$  and  $\mathfrak{E}_2$  defined as

$$S_z = \frac{\left[ \iint |\mathfrak{E}_2(z)|^2 dz \right] \left[ \iint |\mathfrak{E}_1(z)|^2 dz \right]^2}{\left| \iint [\mathfrak{E}_2(z)]^* [\mathfrak{E}_1(z)]^2 dz \right|^2}. \quad (3.51)$$

Furthermore,  $\alpha_+ = \alpha_1 + \alpha_2/2$ , where  $\alpha_1$  and  $\alpha_2$  are the material absorption values for the fundamental and the SH wave, respectively. The function  $g(\sigma, \beta, \kappa, \xi, \mu)$  defined in Eq. (3.48) depends on the parameters  $\sigma$ ,  $\xi$  and  $\mu$ , representing the phase mismatch, the strength of focusing and the focal position, respectively. They are defined as

$$\sigma = \frac{1}{2} b \Delta k_{\text{QPM}}, \quad \xi = \frac{L_{\text{QPM}}}{b}, \quad \mu = 1 - \frac{2x_o}{L_{\text{QPM}}}, \quad (3.52)$$

where  $b = k_1 w_0^2$  is the confocal parameter,  $\Delta k_{\text{QPM}}$  is the phase mismatch,  $L_{\text{QPM}}$  is the length of the periodically poled region and  $x_o/L_{\text{QPM}}$  is the position of beam waist relative to the periodically poled region. The two additional parameters  $\beta$  and  $\kappa$  introduce the double refraction and the absorption influence, respectively. They are defined as follows

$$\beta = \frac{B}{\sqrt{\xi}}, \quad \kappa = \frac{1}{2} \Delta \alpha b, \quad (3.53)$$

where  $B = \rho \sqrt{L_{\text{QPM}} k_1} / 2$  is the double refraction parameter with walk-off angle  $\rho$  and  $\Delta \alpha = \alpha_1 - \alpha_2/2$ . In this work, SHG in periodically poled nonlinear

crystals is considered, where the propagation direction of both fundamental and SH waves is chosen perpendicular to the optical axis  $Z$ , therefore no walk-off is present and  $\beta = B = \rho = 0$ . Furthermore, the optimum phase mismatch parameter  $\sigma$  during SHG in a planar waveguide structure changes with the alternating focusing strength. Optimum parameter  $\sigma_{max,\xi}$  for a given focusing parameter  $\xi$  is defined according to [132, Eq. 19]

$$\sigma_{max,\xi} = \sigma(\xi) = \frac{1}{\xi\sqrt{2}} \arctan\left(\frac{\xi}{\sqrt{2}}\right). \quad (3.54)$$

Fluck [132] investigated also the normalized SHG conversion efficiency in channel waveguides, which reads

$$\bar{\eta}_{\text{SHG}} = \frac{8\pi^2}{\epsilon_0 c_0 \lambda_1^2} \frac{d_{\text{eff,QPM}}^2}{N_2 N_1^2} \frac{1}{S_{yz}} L_{\text{QPM}}^2 e^{-\alpha + L_{\text{cr}}} g_2 \quad (3.55)$$

with

$$g_2 = f(\sigma, \kappa, \xi) = \frac{\sinh^2(\kappa\xi) + \sin^2(\sigma\xi)}{(\kappa\xi)^2 + (\sigma\xi)^2}. \quad (3.56)$$

Eq. (3.56) can be rewritten according to Eq. (3.52) and Eq. (3.53) into

$$g_2 = f(\Delta k, \Delta\alpha) = \frac{\sinh^2\left(\frac{1}{2}\Delta\alpha L_{\text{QPM}}\right) + \sin^2\left(\frac{1}{2}\Delta k L_{\text{QPM}}\right)}{\left(\frac{1}{2}\Delta\alpha L_{\text{QPM}}\right)^2 + \left(\frac{1}{2}\Delta k L_{\text{QPM}}\right)^2}. \quad (3.57)$$

In case of a channel waveguide the effective cross-section is defined as

$$S_{yz} = \frac{\left[ \iint |\mathfrak{E}_2(y, z)|^2 dy dz \right] \left[ \iint |\mathfrak{E}_1(y, z)|^2 dy dz \right]^2}{\left| \iint [\mathfrak{E}_2(y, z)]^* [\mathfrak{E}_1(y, z)]^2 dy dz \right|^2} \quad (3.58)$$

according to [108], similarly to Eq. (3.51), and is related to the effective mode overlap  $\Gamma_{yz}$  [132] as  $S_{yz} = \Gamma_{yz}^{-1}$ .

### Relation between SH and NIR pump power in the experiment

During an SHG experiment only the NIR pump power  $P_{\text{pump}}$  in front of the nonlinear crystal, the transmitted NIR power  $P_{\text{NIR}}$  and the generated SH power  $P_{\text{SH}}$  behind the crystal can be measured. Hence, the coupling efficiency, Fresnel loss and optical loss in the waveguide structure need to be considered, in order to determine the normalized conversion efficiency  $\bar{\eta}_{\text{SHG}}$  experimentally. For the end-user of a SHG waveguide structure, it is often not possible to estimate every loss factor separately, due to lack of equipment and sufficient number of SHG devices to conduct measurements facilitating e.g, the cut-back technique. It is however possible to measure the overall transmission through the waveguide, which reads

$$\tau = \eta_c e^{-\delta L_{\text{cr}}} \quad (3.59)$$

with the coupling efficiency  $\eta_c$ , loss coefficient  $\delta$  and crystal length  $L_{cr}$ , provided that the crystal facets possess AR coating. The transmission can be determined experimentally according to

$$\tau = \frac{P_{NIR}}{P_{pump}} \quad (3.60)$$

by measuring the values of  $P_{NIR}$  and  $P_{pump}$ , when the phase-matching condition is not fulfilled (Sect. 3.2.3, p. 22). This can be achieved by detuning the crystal temperature or laser wavelength from the optimum value.

Consequently, in this work the relation between SH power  $P_{SH}$  behind and NIR pump power  $P_{pump}$  in front of the nonlinear crystal resulting from Eq. (3.44) and Eq. (3.46) is supplemented by the measured transmission value  $\tau$  in accordance with

$$P_{SH} = \tau P_{pump} \tanh^2 \left( \sqrt{\bar{\eta}_{SHG} \tau P_{pump}} \right). \quad (3.61)$$

Hence, the normalized conversion efficiency  $\bar{\eta}_{SHG}$  can be calculated from the measured values of  $P_{pump}$ ,  $\tau$  and  $P_{SH}$  according to the relation

$$\bar{\eta}_{SHG} = \frac{1}{\tau P_{pump}} \operatorname{arctanh}^2 \left( \sqrt{\frac{P_{SH}}{\tau P_{pump}}} \right) \quad (3.62)$$

resulting from a transformation of Eq. (3.61).

The opto-optical conversion efficiency is defined as

$$\eta_{opt.} = \frac{P_{SH}}{P_{pump}} \quad (3.63)$$

with the SH power  $P_{SH}$  behind and NIR pump power  $P_{pump}$  in front of the nonlinear crystal. Due to nonlinear character of the interaction the opto-optical conversion efficiency is expected to increase with increasing NIR pump power  $P_{pump}$ . The electro-optical conversion efficiency is defined as

$$\eta_{el.} = \frac{P_{SH}}{P_{el.}} \quad (3.64)$$

with the SH power  $P_{SH}$  behind the crystal and the electrical power  $P_{el.}$  applied to bias the active section or sections of the diode laser. Please note that the power applied for cooling of the laser and for the adjustment of the nonlinear crystal temperature is not taken into consideration in this expression.

### 3.3 Design and selection of waveguide SHG devices

In this work, frequency doubling of diode lasers in pure crystal waveguides of MgO doped lithium niobate is investigated. Optical lenses are applied in order to couple the diode laser radiation into the waveguide SHG devices due to high efficiency and required flexibility of this method. The collimated laser

beam is focused onto the waveguide facet in a manner which maximizes the overlap integral (Eq. 3.5 and 3.6) with the waveguide lowest-order mode of the fundamental wave.

Since the phase-matching condition of a nonlinear process in a waveguide structure can only be fulfilled between one discrete waveguide mode of the fundamental and of the SH wave at a time, it is important to couple the incidence radiation into only one mode to the highest possible extent. Nonlinear interactions between waveguide lowest-order modes are preferable, since they not only provide a high mode overlap between the fundamental and SH wave, which increases the normalized SHG conversion efficiency (Eq. (3.47) and (3.55)), but also enable a high input coupling efficiency of nearly diffraction limited diode laser radiation [44, p. 195].

Lithium niobate is used as nonlinear medium due to its highest nonlinear coefficient among ferroelectric crystals available [134]. Furthermore, pure crystal waveguides are applied in the experiments, since, in contrast to annealed proton exchanged waveguides [135, 136], they are characterized by a non-degraded nonlinear coefficient [137, 138, 139] and provide large mode overlap between the fundamental and the SH wave [140, 141, 100]. In addition, compared to Ti diffused waveguides [93, 94], pure crystal waveguides are less susceptible to photorefractive [96, 142].

Below, in Sect. 3.3.2 and 3.3.3, the manufacturing process and the properties of the ridge waveguide and planar waveguide structures, respectively, applied in the experiments, are described. In advance, the characteristics of MgO doped lithium niobate are discussed in detail in Sect. 3.3.1.

### 3.3.1 MgO doped lithium niobate

MgO doped lithium niobate (MgO:LN) is commonly applied for SHG into the visible spectral range due to its large nonlinear coefficient component  $d_{33} = 25$  pm/V [143] and its increased resistance to the photorefractive [144, 145, 146, 147] and the photochromic [145, 148, 149] effects.

The photorefractive effect in lithium niobate (LN) [150] becomes noticeable through a distortion of a laser beam propagating through a crystal sample. This phenomenon, which occurs and dissolves not instantaneously with the begin and cease of the laser illumination, respectively, originates from optical ionization of undesired donor impurities present in the crystal, e.g.  $\text{Fe}^{+2}/\text{Fe}^{+3}$  ions. The released charges move from the illuminated region to the surrounding dark parts of the crystal, where they are trapped by acceptor impurities. The electrooptic effect, induced by the arisen electric field between the donors and acceptors, leads to a refractive index change and a consequent beam distortion.

The photochromic effects, which are also induced by laser light illumination, lead to absorption changes [117]. The most significant photochromic effect in LN is the green-induced infrared absorption [151], whose origin has not been defined unambiguously until now. Furthermore, the linear absorption [152] as well as the two-photon absorption [153, 154, 155] need to be taken into

consideration during high-power SHG experiments into the visible spectral region.

The photorefractive effect can be significantly reduced by heating the crystal above the annealing temperature ( $T \approx 180^\circ\text{C}$ ) [116, p. 102] or doping with specific impurities, such as for instance  $\text{Mg}^{+2}$  [156, 157], both of which enable high-power SHG into the green spectral region [158, 159]. The influence of  $\text{Mg}^{+2}$  doping in LN has been studied quantitatively in the past, showing that unlike undoped LN, 5 mol% doped  $\text{MgO:LN}$  is less prone to photorefraction [146, 147] and green-induced infrared absorption [148, 149]. In addition, it has been shown that stoichiometrically grown crystals require smaller doping concentrations to suppress the photorefractive and photochromic effects [144, 145].

$\text{MgO:LN}$  is an uniaxial crystal with a distinguished optical axis  $Z$ , which is characterized by an ordinary and extraordinary refractive index. For the purpose of this work, temperature dependent Sellmeier equations determined experimentally in [160, 161, 162] are applied. Furthermore,  $\text{MgO:LN}$  belongs to the symmetry class  $3m$ , which leads to three independent components in the matrix representing the nonlinear coefficient [112, p. 46]

$$d = \begin{bmatrix} 0 & 0 & 0 & 0 & d_{31} & -d_{22} \\ -d_{22} & d_{22} & 0 & d_{31} & 0 & 0 \\ d_{31} & d_{31} & d_{33} & 0 & 0 & 0 \end{bmatrix}. \quad (3.65)$$

The largest component  $d_{33}$  can be efficiently utilized by means of QPM for electric fields oscillating along the optical axis  $Z$  (Sect. 3.2.3) leading to an effective nonlinear coefficient

$$d_{\text{eff,QPM}} = 16 \text{ pm/V} \quad (3.66)$$

in accordance with Eq. (3.36). Furthermore, QPM enables the nonlinear interactions in the whole transparency range of  $\text{MgO:LN}$ , i.e. from 400 nm to approx. 5  $\mu\text{m}$  [134, p. 159].

Further information regarding  $\text{MgO:LN}$  properties and its versatile applications can be found in [134, p. 159] and [163].

#### 3.3.2 Ridge waveguide

The ridge waveguide applied in this work is a pure crystal waveguide from Panasonic [111]. The QPM structure for SHG from 1061 to 530.5 nm was obtained from a 500  $\mu\text{m}$ -thick  $5^\circ$  off-axis  $Y$ -cut 5 mol%  $\text{MgO:LN}$  wafer through a 2-dimensional application method with multiple high-voltage pulses [164]. In the bottom surface of the wafer 0.3  $\mu\text{m}$  deep groves were dry-etched along the  $X$  axis forming an air gap after direct bonding of the wafer to a LN substrate [165, 166]. Subsequently to grinding and polishing of the wafer upper surface to a thickness of approx. 4  $\mu\text{m}$ , 5  $\mu\text{m}$  wide ridge waveguide structures were formed over the air-gaps by inductively coupled plasma etching. A schematic of this novel ridge waveguide structure is presented in Fig. 3.5, an SEM image can be found in [111].

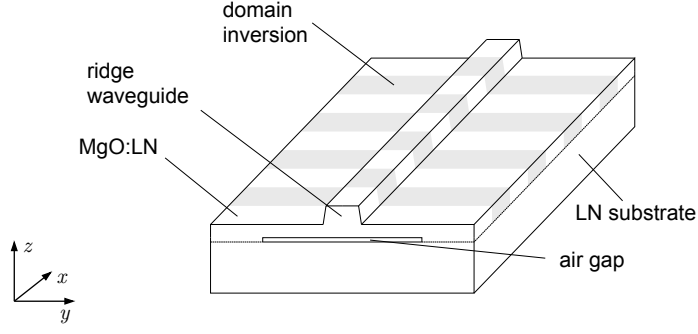


**Figure 3.5:** Schematic of the ridge waveguide structure applied in the experiments

The 11.5 mm-long ridge waveguide applied in the experiments contains facets laterally angled under  $10^\circ$  and coated with  $\text{SiO}_2$ , which results in a reflectivity of  $< 0.001$  and  $0.143$  for the fundamental and the SH wave, respectively.

In Fig. 3.6 the distributions of the amplitude  $\mathfrak{A}^{(00)}(y, z)$  and the corresponding phase  $\varphi^{(00)}(y, z)$  for the waveguide lowest-order mode of the fundamental and SH wave simulated with FIMMWAVE are presented. The real electric field distribution  $\mathfrak{E}^{(00)}(y, z)$  is defined through the relation:

$$\mathfrak{E}^{(00)}(y, z) = \mathfrak{A}^{(00)}(y, z) \cdot \cos\left(\varphi^{(00)}(y, z)\right). \quad (3.67)$$

Calculation of the corresponding effective mode overlap according to Eq. (3.58) results in a value  $S_{yz} = 13.7 \mu\text{m}^2$ , which leads to an expected maximum normalized SHG conversion efficiency of  $\bar{\eta}_{\text{SHG}} = 630 \text{ \% W}^{-1}$  calculated according to Eq. (3.55) for a neglected absorption ( $\alpha_+ = 0 \text{ cm}^{-1}$ ). Due to this high value, fundamental power under one Watt is required to reach an opto-optical conversion efficiency of more than 50 % in a ridge waveguide SHG device [101, 102]. Therefore, a DBR-RWL described in Sect. 2.3.2 (p. 11) is well suited for

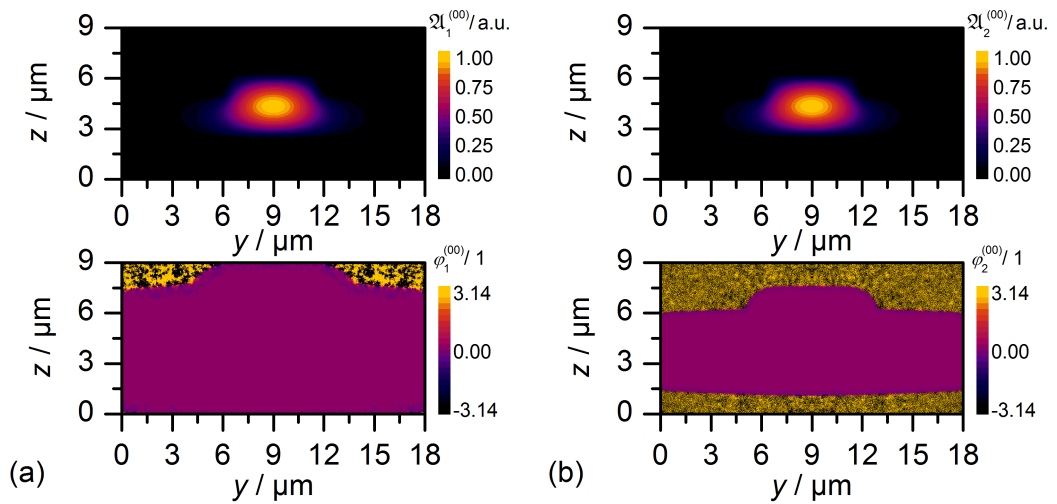


**Figure 3.6:** Simulated ridge waveguide lowest-order mode amplitude  $\mathfrak{A}^{(00)}(y, z)$  and phase  $\varphi^{(00)}(y, z)$  for the fundamental (a) and SH (b) wave

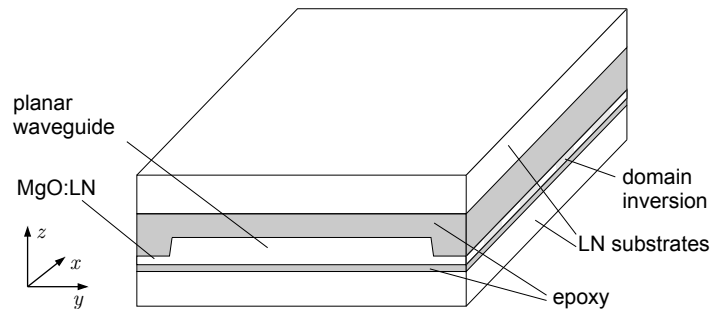
efficient frequency doubling in this geometry.

Due to laterally angled front and rear facet, the ridge waveguide crystal sample is mounted in the experimental setup under an lateral angle of  $11.8^\circ$  in order to obtain maximum coupling efficiency into the waveguide lowest-order mode.

#### 3.3.3 Planar waveguides

The planar waveguide-integrated QPM structures for SHG from 1064 to 532 nm were manufactured by Commax Co., Ltd and Korea Electronics Technology Institute (KETI). The samples were obtained from a 500  $\mu\text{m}$ -thick *Z*-cut 5 mol% MgO:LN wafer. The wafer had one side polished down to 150  $\mu\text{m}$  and was prepared for periodical poling, as described in [167]. The periodical poling was performed in a poling jig with electrolyte electrodes [168] at room temperature by applying an external electric field generated by a voltage of 0.7 kV over 120 ms. Sample examination with a polarization microscope and chemical etching of identical samples made it possible to determine the structure duty cycle to be very close to 50 %. Subsequently, the polished surface was bonded to an LN substrate using an epoxy, which was the bottom cladding layer in the final waveguide structure. The other side of the bonded wafer was secondarily

**Figure 3.7:**  
Schematic of the planar waveguide structure applied in the experiments



polished to have a thickness of 7  $\mu\text{m}$ , with a thickness uniformity better than 0.1  $\mu\text{m}$ . Subsequently, the wafer was 5  $\mu\text{m}$  deep dry-etched by a modified reactive ion etching technique, forming ridge waveguides with different widths and a thickness of 7  $\mu\text{m}$ . The residual slab thickness of 2  $\mu\text{m}$  on both waveguide sides results in a better sample reliability and a lower propagation loss for channel waveguides [169, 170]. Finally, another LN substrate was bonded to the waveguide core top surface with an epoxy, which formed the upper cladding layer. A schematic of the planar waveguide structure is presented in Fig. 3.7.

The SHG experiments are conducted in 13 and 15 mm-long samples, all of which consist of a 12 mm-long periodically poled region and a vertical waveguide structure described above. In Fig. 3.8 the electric field distribution  $\mathcal{E}^{(m)}(z)$  of three first modes for the fundamental and SH wave simulated with FIMM WAVE are presented. The large number of supported modes as well as their strong confinement within the waveguide core result from high refractive index step between the cladding and the core region. For the SHG process only the

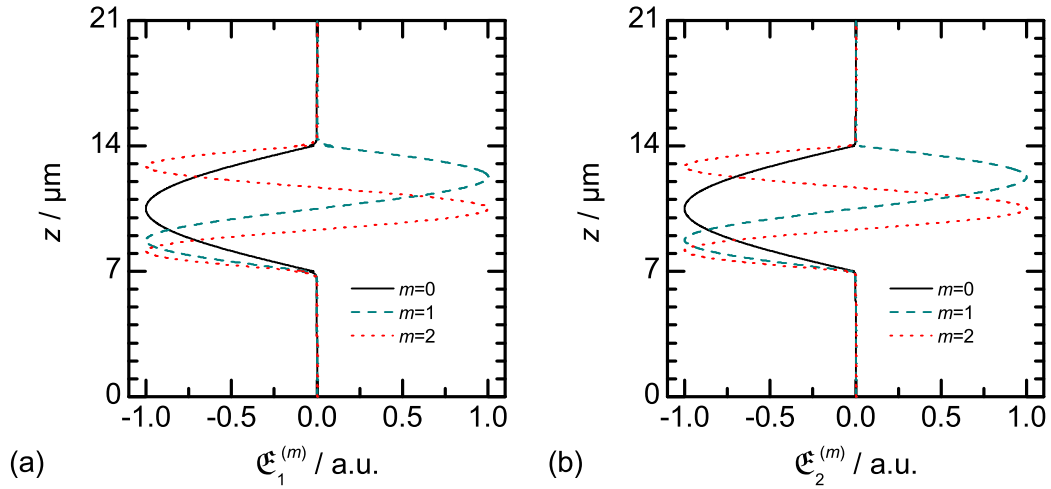


**Figure 3.8:** Simulated planar waveguide mode distributions  $\mathfrak{E}^{(m)}(z)$  of three first modes ( $m = 0, 1, 2$ ) for the fundamental (a) and SH (b) wave

waveguide lowest-order modes of both waves are of relevance, for which the corresponding effective mode overlap  $S_z = 4.9 \mu\text{m}$  is determined according to Eq. (3.51). With this value, with neglected absorption ( $\alpha_+ = 0 \text{ cm}^{-1}$ ) and with optimally focused Gaussian beam, a maximum normalized SHG conversion efficiency of  $\bar{\eta}_{\text{SHG}} = 36 \text{ \% W}^{-1}$  calculated according to Eq. (3.47) is expected for the planar waveguide structures manufactured for the purpose of this work. For this value a fundamental power of more than 2 W is required to achieve an opto-optical conversion efficiency of 50 % [107]. Therefore, a DBR-TPL (Sect. 2.3.2, p. 12), providing higher output power than a DBR-RWL, is better suited for efficient frequency doubling in a planar waveguide structure.

The 13 mm-long waveguides with a width of 160 and 190  $\mu\text{m}$ , denoted as L13-W160 and L13-W190, respectively, have facets angled laterally under  $5.4^\circ$  and AR coated for the fundamental and SH radiation. 15 mm-long samples with a width of 300  $\mu\text{m}$  (L15-W300-WG1 and L15-W300-WG2) and with a width of 500  $\mu\text{m}$  (L15-W500-WG1 and L15-WG500-WG2) possess a lateral facet wedge angle of  $2.5^\circ$  and a broadband AR coating for the fundamental and SH wave.

Due to the lateral wedge angle of the facets, the 13 mm and 15 mm-long planar waveguide samples are placed in the experimental setup at a lateral angle of  $6.3^\circ$  and  $2.9^\circ$ , respectively, in order to obtain beam propagation direction inside of the waveguide perpendicular to the QPM grating and parallel to the waveguide axis.



# Chapter 4

## Diode laser frequency doubling in a ridge waveguide

Frequency doubling of NIR diode lasers in periodically poled MgO doped LiNbO<sub>3</sub> (ppMgO:LN) channel waveguides is well suited to realize highly efficient and compact green laser modules with moderate output power and good beam quality [4, 103, 171, 172]. Channel waveguides are superior to bulk crystals during SHG with NIR diode lasers in terms of conversion efficiency and beam quality of the SH radiation [19, 20, 136, 172]. High conversion efficiency allows to apply shorter crystals and to enlarge the spectral and the temperature acceptance bandwidths (Sect. 3.2.3). However, SHG in channel waveguides requires higher adjustment accuracy in order to maximize the coupling efficiency [4, 103], which are not required in bulk crystals [19, 20]. Furthermore, the highest SH output power until now reported with a ridge waveguide was limited to 350 mW [103], while in bulk crystals green powers in excess of 1.5 W and almost 4 W were reached through second-harmonic [9, 10] and sum-frequency generation [173], respectively.

In a number of works on SHG in channel waveguides a saturation of the conversion efficiency at high output powers has been observed [100, 174, 175, 176], resulting from optical absorption, heat generation and a temperature gradient along the waveguide axis. In addition, it has been shown, that inhomogeneities in the crystal composition, QPM period or waveguide structure along the light propagation direction lead to a decrease in the SHG conversion efficiency [94, 125, 126, 167, 175, 176, 177, 178]. Therefore, the influence of these effects needs to be studied extensively, in order to understand the limitations of the SHG process in channel waveguides in terms of maximum accessible conversion efficiency and SH power.

In this chapter, highly efficient, high-power single-pass frequency doubling of a DBR ridge waveguide diode laser (DBR-RWL) is demonstrated. In particular, the limitations of the SHG process in a ppMgO:LN ridge waveguide due to nonlinear device imperfections, optical absorption and subsequently induced thermal load are investigated in-depth. Additionally to an extensive experimental study, a theoretical model for SHG in a ridge waveguide combining a system of coupled equations and a 1-dimensional, steady-state heat diffusion

equation is applied to describe qualitatively and quantitatively the influence of the geometrical inhomogeneities on the SHG conversion efficiency, as well as the influence of the optical absorption on the observed saturation of the SH power.

This chapter is organized as follows: in Sect. 4.1 the experimental setup for frequency doubling in a ridge waveguide is described. The experimental results including the characteristics of NIR radiation and the SHG process are presented in Sect. 4.2 and 4.3, respectively. In Sect. 4.4 the extended theoretical model applied to simulate the SHG process is described. The results of simulations are analyzed and compared with experiments in Sect. 4.6. Finally, in Sect. 4.7 a brief summary of the chapter is presented.

## 4.1 Experimental setup

The schematic diagram of the experimental setup for frequency doubling in a ridge waveguide is presented in Fig. 4.1. The DBR-RWL applied in this experiment as a pump laser is described in detail in Sect. 2.3. The laser chip is mounted p-side up on a c-mount holder and operated at  $T = 27^\circ\text{C}$ . Setup

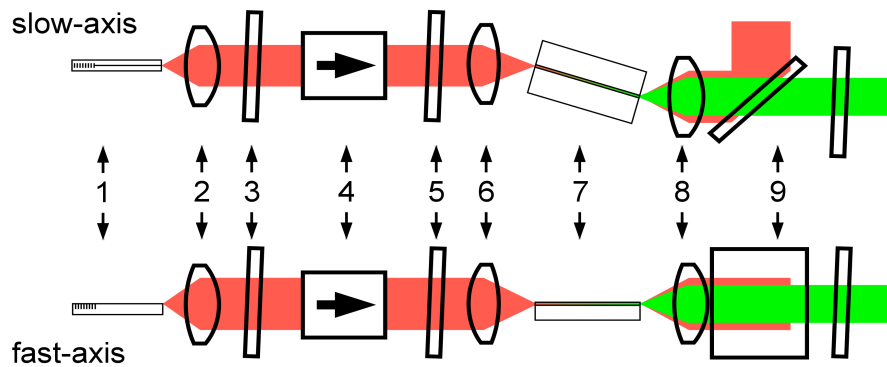


**Figure 4.1:** Schematic diagram of the frequency doubling setup: 1, DBR diode laser; 2, aspheric lens L1; 3, half-wave plate H1; 4, optical isolator; 5, half-wave plate H2; 6, aspheric lens L2; 7, nonlinear crystal with a ridge waveguide; 8, aspheric lens L3; 9, dichroic mirror system

lens combination applied in this experiment is chosen accordingly to optical simulations in order to maximize the coupling efficiency into the waveguide lowest-order mode of the fundamental wave. For this purpose the beam propagation is simulated with WINABCD, a ray transfer matrix analysis software from Ferdinand-Braun-Institut, based on the measured spatial emission characteristics of the diode laser. An aspheric lens with a numerical aperture value  $\text{NA} = 0.55$  is chosen for collimation in order to minimize aberration errors and in order to set the diameter of the collimated beam to approx. one half of the smallest aperture diameter in the setup. An aspheric lens is chosen for focussing in order to generate a beam waist diameter on the crystal facet conform to the waveguide lowest-order mode of the fundamental wave.

As presented in Fig. 4.1, the divergent beam is collimated with an aspheric lens,

L1 (C230TME-B from Thorlabs,  $f = 4.5$  mm). The half-wave plate (HWP), H1, in front of the 60 dB optical isolator allows to adjust the NIR power without changing the properties of the laser beam. The HWP behind the isolator, H2, is used to adjust the polarization of the NIR radiation. The laser beam is focused into the waveguide with another aspheric lens, L2 (C110TME-B from Thorlabs,  $f = 6.2$  mm). All optical elements applied in front of the crystal have a broadband anti-reflective (AR) coating around 1064 nm.

The radiation behind the crystal is collimated with an aspheric lens L3 (C240TME-A from Thorlabs,  $f = 8.0$  mm) AR coated for the SH radiation. The dichroic mirror set (F73-767 from AHF analysentechnik AG) used to separate the SH and NIR wave is characterized by a total transmission of 0.87 and  $10^{-6}$  for the SH and NIR radiation, respectively, linearly polarized along the slow-axis. All experimental results in this chapter are presented without the losses originating from the collimating lens L3 and the dichroic mirror set.

## 4.2 Diode laser characteristics

The power-voltage-current (PUI) characteristics of the diode laser applied in the experiment is presented in Fig. 4.2. Laser operation begins at a threshold current of  $I_{RW, th} = 0.11$  A and the optical power increases linearly with increasing current at a slope of 0.77 W/A. The undulations visible in the

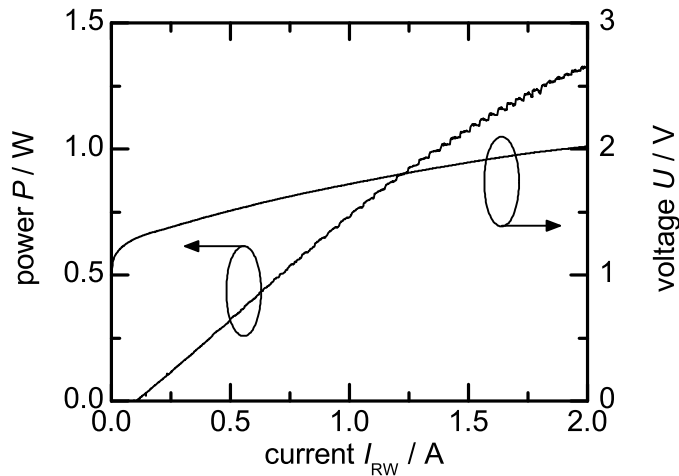


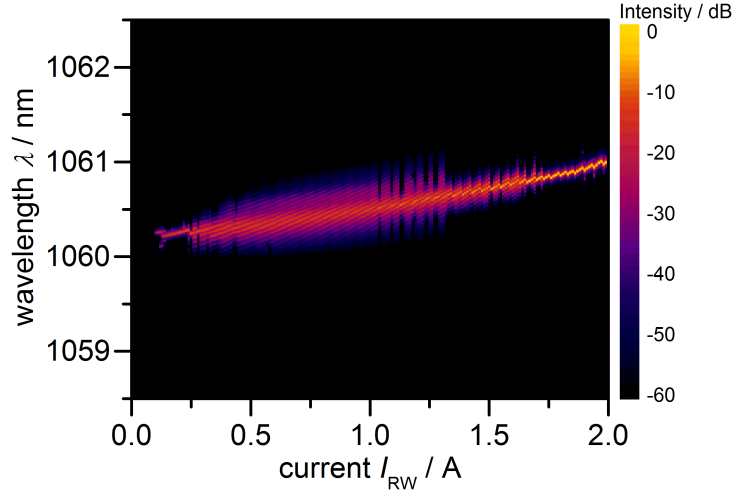
**Figure 4.2:** PUI-characteristics of the DBR-RWL applied in the experiment ( $T = 27^\circ\text{C}$ ,  $\Delta I_{RW} = 0.002$  A)

power distribution above a power level of 0.7 W originate from mode-hops characteristic for DBR lasers. The measured voltage-current distribution is typical for a p-n junction.

The spectral mapping presented in Fig. 4.3 was measured with optical spectrum analyzer Q8384 from Advantest in 0.01 A steps. The central wavelength lies at 1060.25 nm at the threshold and increases with the increasing RW current at a rate of 0.40 nm/A.

During the frequency doubling experiment, the DBR-RWL is biased with  $I_{RW} = 2.0$  A. The transmission of the optical isolator in the range of 90 %

**Figure 4.3:** Spectral mapping of the DBR-RWL applied in the experiment ( $T = 27^\circ\text{C}$ ,  $\Delta I_{\text{RW}} = 0.01\text{ A}$ )



and the residual reflections of optical surfaces result in a maximal NIR pump power of  $P_{\text{pump}} = (1.01 \pm 0.03)\text{ W}$  in front of the nonlinear crystal. The laser emits at a central wavelength of 1061.0 nm in a longitudinal single-mode, as can be seen in Fig. 4.4 (a). The measured side mode suppression ratio of approx. 40 dB and a spectral bandwidth of 10 pm (FWHM) correspond to the maximum signal-to-noise ratio and minimum resolution of the applied DEMON spectrometer (Appendix A.1). The beam quality of the NIR beam is determined

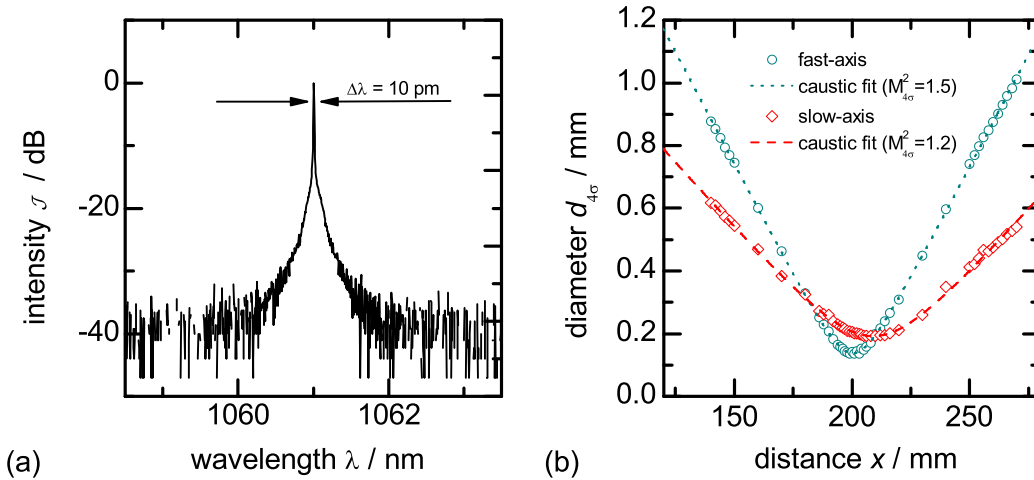


**Figure 4.4:** Spectrum (a) and caustic (b) of the DBR-RWL beam at  $T = 27^\circ\text{C}$ ,  $I_{\text{RW}} = 2.0\text{ A}$

through a caustic measurement (Appendix A.1) behind the half-wave plate H2. The corresponding caustic measured according to second order moments is presented in Fig. 4.4 (b). A beam propagation ratio  $M_{4\sigma}^2$  of 1.5 and 1.2 for the fast- and slow-axis, respectively, are determined. When  $1/e^2$ -level method is applied to determine the beam diameters, beam propagation ratio  $M_{1/e^2}^2$  of 1.0 and 1.1 result in the fast- and slow-axis, respectively.

The ridge waveguide crystal applied in the experiment is described in detail in

Sect. 3.3.2. The waveguide lowest-order mode intensity profile resulting from FIMMWARE simulations is presented in Fig. 4.5 (a) on linear and logarithmic scale. It is characterized by a  $1/e^2$  threshold diameter of 3.0 and 5.6  $\mu\text{m}$  in the

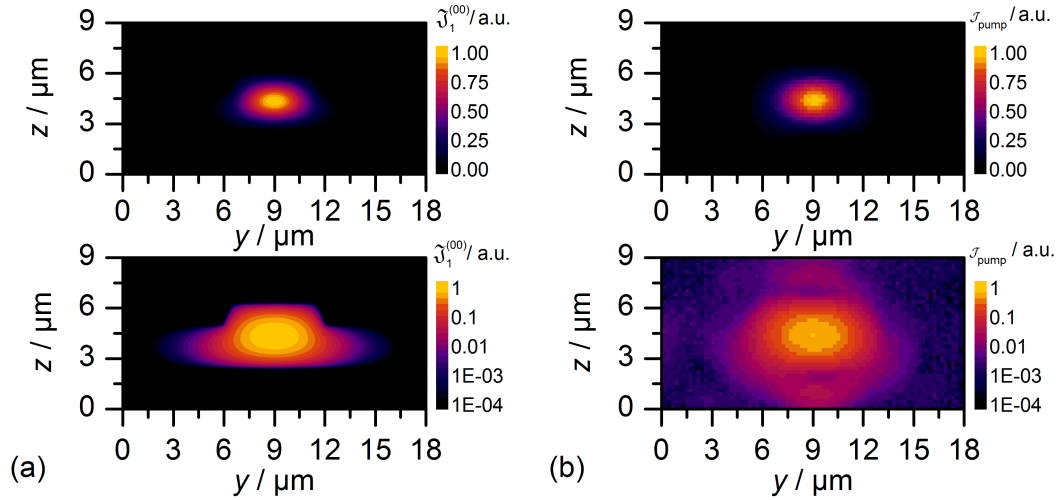


**Figure 4.5:** Simulated lowest-order mode intensity of the ridge waveguide  $\mathcal{J}_1^{(00)}$  (a) and measured pump intensity distribution in the beam waist  $\mathcal{J}_{\text{pump}}$  (b)

vertical and lateral direction, respectively. The intensity distribution of the pump beam measured with a microscope objective (Appendix A.1) in the beam waist behind the aspheric lens L2 is presented in Fig. 4.5 (b). The vertical and lateral  $1/e^2$  threshold beam waist diameters of  $(3.2 \pm 1.1)$  and  $(6.0 \pm 1.1)$   $\mu\text{m}$ , respectively, agree well with the diameters of the simulated waveguide lowest-order mode. The measured distribution contains finite intensity values lying far beyond the beam diameter, as can be seen on the logarithmic scale. Based on these two distributions the coupling efficiency into the waveguide lowest-order mode can be approximated theoretically. Calculation of the overlap integral from Eq. (3.5) results in a coupling efficiency of 85 %.

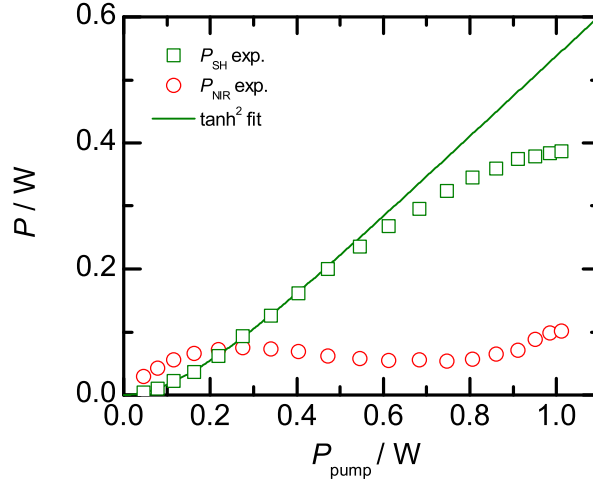
### 4.3 Experimental results

In advance to SHG experiments the transmission through the waveguide structure is determined by measuring the NIR power behind and in front of the crystal. For this purpose the crystal mount temperature is set to 20  $^\circ\text{C}$ , at which the QPM condition for the SHG process is not fulfilled. The measured transmission at the extraordinary polarization in dependence of the NIR pump power is presented in Fig. 4.7 (a). In the investigated power range the transmission remains constant and results in an average value of  $\tau = (69 \pm 1)$  %. With the optical loss of 0.8 dB/cm from [111] the coupling efficiency at the extraordinary polarization can be determined to  $\eta_c = (86 \pm 1)$  %. This value agrees well with the prediction from Sect. 4.1 on page 41.

Subsequently, the frequency doubling experiments are performed. Firstly, the

SH power and the NIR power behind the crystal are studied in dependence on the NIR pump power in front of the nonlinear crystal. The corresponding results are presented in Fig. 4.6. Theoretically, the SH power follows the

**Figure 4.6:** Measured power behind vs. NIR pump power in front of the nonlinear crystal. The crystal mount temperature is adjusted for every NIR pump power as presented in Fig. 4.7 (b) in order to maximize the corresponding SH power



$\tanh^2$  distribution, derived for example in [114]. The following extended  $\tanh^2$  function (solid curve) is fitted to the SH power values (open squares) below  $P_{\text{SH}} = 50$  mW:

$$P_{\text{SH}} = (1 - R_{\text{SH}}) \cdot \tau P_{\text{pump}} \cdot \tanh^2 \left( \sqrt{\bar{\eta}_{\text{SHG}} \cdot \tau P_{\text{pump}}} \right), \quad (4.1)$$

where  $P_{\text{SH}}$  is the SH power behind the crystal,  $R_{\text{SH}} = 14$  % is the crystal back facet reflectivity for the SH wave,  $\tau = 69$  % is the transmission through the ridge waveguide,  $P_{\text{pump}}$  is the NIR pump power in front of the nonlinear crystal. The normalized SHG conversion efficiency  $\bar{\eta}_{\text{SHG}}$  is the fitting parameter, which results in a value of  $(496 \pm 15)$  %  $\text{W}^{-1}$ .

As can be seen in Fig. 4.6, the measured SH power shows a good agreement with the  $\tanh^2$  distribution until  $P_{\text{SH}} \approx 200$  mW (corresponding to an SH and fundamental wave power density of  $\mathcal{J}_2 \approx 1.7$   $\text{MW}/\text{cm}^2$  and  $\mathcal{J}_1 \approx 3.0$   $\text{MW}/\text{cm}^2$ , respectively). Above this value the measured SH power departs from the theoretical distribution with increasing NIR pump power until a saturation of the SHG process can be observed above  $P_{\text{SH}} \approx 360$  mW (corresponding to an SH and fundamental wave power density of  $\mathcal{J}_2 \approx 3.1$   $\text{MW}/\text{cm}^2$  and  $\mathcal{J}_1 \approx 5.4$   $\text{MW}/\text{cm}^2$ , respectively). In the experiment a maximum SH power of  $P_{\text{SH}} = (386 \pm 15)$  mW is reached at a corresponding opto-optical and electro-optical conversion efficiency of  $\eta_{\text{opt.}} = (38 \pm 2)$  % and  $\eta_{\text{el.}} = (9.6 \pm 0.4)$  %, respectively. A maximum conversion efficiency of  $\eta_{\text{opt.}} = (44 \pm 2)$  % is reached at an NIR pump power of  $P_{\text{pump}} = (611 \pm 18)$  mW.

The residual NIR power behind the nonlinear crystal (open circles) increases initially with increasing NIR pump power until it reaches its local maximum value of  $P_{\text{NIR}} \approx 73$  mW at  $P_{\text{pump}} = (275 \pm 8)$  mW. It decreases subsequently to a level of  $P_{\text{NIR}} \approx 50$  mW and remains constant until the saturation of the SHG process begins, when it increases for a second time and reaches its maximum

value of  $P_{\text{NIR}} \approx 100$  mW at  $P_{\text{pump}} = (1.01 \pm 0.03)$  W.

The SH and NIR power measured behind the crystal enable the calculation of the corresponding overall transmission. Fig. 4.7 (a) shows measured overall transmission through the ridge waveguide during SHG process (open circles), defined as

$$\tau^{\text{SHG}} = \frac{(1 - R_{\text{SH}})^{-1} P_{\text{SH}} + P_{\text{NIR}}}{P_{\text{pump}}}, \quad (4.2)$$

in dependence on the increasing NIR pump power. Please note, that in this definition the influence of the SH facet reflectivity  $R_{\text{SH}}$  is taken into account. Unlike the transmission of the NIR radiation (filled circle) the overall trans-

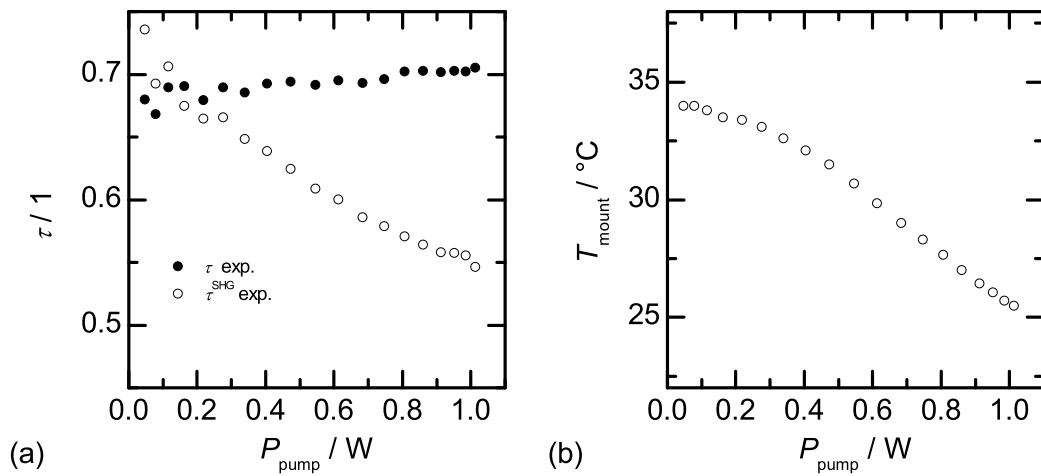
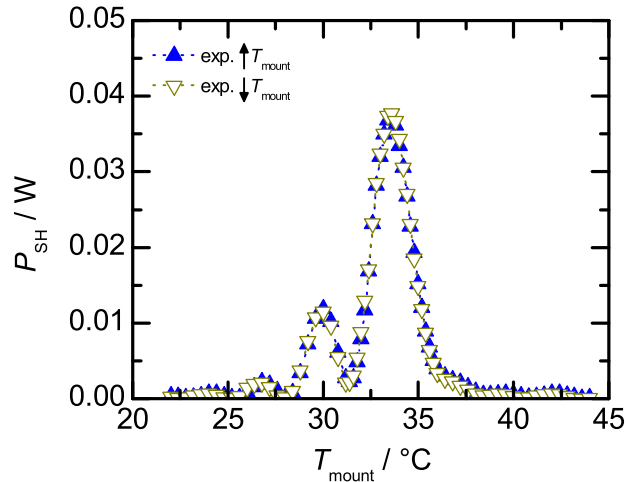


**Figure 4.7:** Experimentally determined transmission through the ridge waveguide with and without quasi phase-matching (a) and the crystal mount temperature  $T_{\text{mount}}$  (b) during SHG process vs. NIR pump power  $P_{\text{pump}}$  in front of the nonlinear crystal corresponding to results presented in Fig. 4.6

mission during SHG decreases linearly with the increasing NIR pump power in front of the nonlinear crystal from around 70 % to 54 % in the investigated range. Hence, the loss in the ridge waveguide during SHG increases nearly linearly with the increasing NIR pump power in front of the nonlinear crystal. The crystal mount temperature is adjusted at each NIR pump power value in order to optimally satisfy the QPM condition from Eq. (3.40) and maximize the SH output power. As can be seen in Fig. 4.7 (b), initially, the maximum SH power is reached at a crystal mount temperature of 34.0 °C. With increasing NIR pump power, the crystal mount temperature (open circles) has to be gradually reduced by 8.5 K over the investigated power range and reaches its minimum value of 25.5 °C at  $P_{\text{pump}} = (1.01 \pm 0.03)$  W. This behavior indicates that the temperature inside of the ridge waveguide increases due to optical absorption with increasing NIR and SH power.

Subsequently, the influence of crystal mount temperature on the SH power

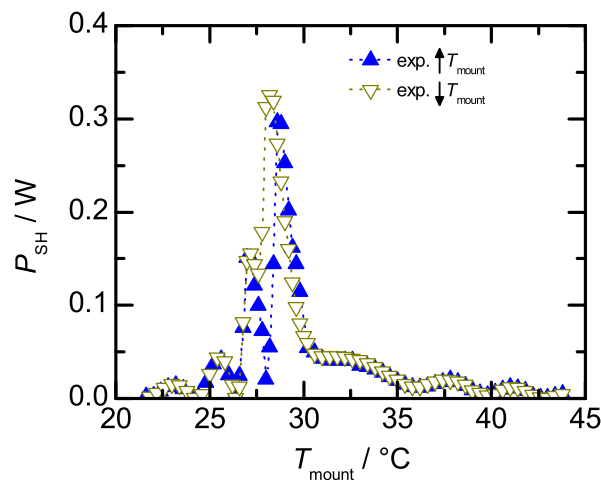
**Figure 4.8:** Measured SH power dependence on the crystal mount temperature  $T_{\text{mount}}$  at an NIR pump power  $P_{\text{pump}} = (162 \pm 5)$  mW



is investigated. Two tuning curves for crystal mount being cooled down and heated up at  $P_{\text{pump}} = (162 \pm 5)$  mW are presented in Fig. 4.8. Both curves (open and filled triangles) match very well each other, deviate however from the theoretical  $\text{sinc}^2$  distribution. The maximum SH power of 37.7 mW is reached at a crystal mount temperature of 33.6°C. The measured acceptance bandwidth of  $\Delta T = 2.4$  K (FWHM) independent of the temperature modification direction corresponds well to the waveguide length. The measured curves are asymmetric and exhibit a distinctive side-peak at 30.0°C, which indicates an inhomogeneity in the SHG waveguide device structure discussed below in Sect. 4.6.

Analog measurements are carried out at an NIR pump power of  $P_{\text{pump}} = (747 \pm 22)$  mW and the corresponding results are presented in Fig. 4.9. The maximum SH power of  $P_{\text{SH}} = (325 \pm 10)$  mW is reached at a crystal mount temperature of 28.2°C while the crystal mount is being cooled down (open triangles). The corresponding acceptance bandwidth lies at 1.1 K (FWHM)

**Figure 4.9:** Measured SH power dependence on the crystal mount temperature  $T_{\text{mount}}$  at an NIR pump power  $P_{\text{pump}} = (747 \pm 22)$  mW



and is more than two times smaller than in case of the low NIR pump power (Fig. 4.8). The main peak and the side peak cannot be clearly separated, since both peaks are located closer together. A distinct hysteresis in data distribu-

tions can be observed between cooling down and heating up. This phenomenon has been previously reported and discussed by Dmitriev *et al.* in [179]. When the crystal mount temperature is being increased (filled triangles), a maximum SH power of  $P_{\text{SH}} = (296 \pm 8)$  mW at a crystal mount temperature of  $28.6^\circ\text{C}$  is reached. The side-peak at  $27.0^\circ\text{C}$  is separated from the main peak by a distinct minimum at  $28.0^\circ\text{C}$ . Furthermore, the width (FWHM) of the main peak can be determined to 1.3 K. Both curves exhibit a plateau over a range of 4.0 K on the right hand side of the main peak, which is not visible at a lower NIR pump power (Fig. 4.8).

The SH spectrum at  $P_{\text{SH}} = (325 \pm 10)$  mW measured with ELIAS spectrometer (Appendix A.1) in double pass is presented in Fig. 4.10 (a). The determined

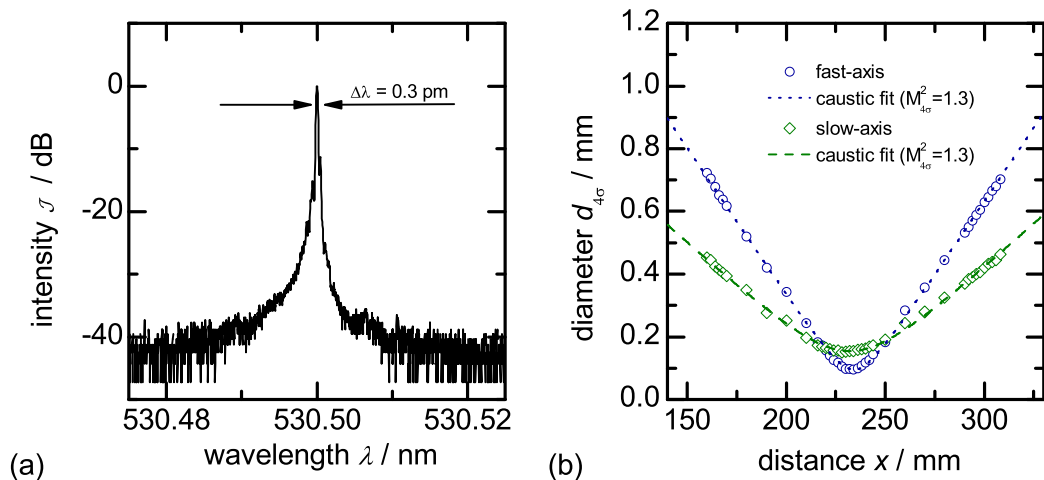


**Figure 4.10:** Spectrum (a) and caustic (b) of the SH beam at  $P_{\text{SH}} = (325 \pm 10)$  mW

spectral bandwidth of 0.3 pm (FWHM) as well as a noise level of  $-40$  dB are limited by the spectral resolution and the maximum signal-to-noise ratio of the applied spectrometer, respectively.

The SH beam quality is predetermined by the ridge waveguide structure. Results of a SH caustic measurement according to second order moments method at an SH power level of  $P_{\text{SH}} = (325 \pm 10)$  mW are presented in Fig. 4.10 (b). A beam propagation ratio  $M_{4\sigma}^2$  of 1.3 in both fast- and slow-axis is determined. For  $1/e^2$ -level diameters a beam propagation ratio  $M_{1/e^2}^2$  of 1.0 is determined.

## 4.4 Development of a tailored theoretical model

The coordinate system chosen in the theoretical model differs from the crystallographic axes of the ridge waveguide nonlinear crystal. Here and throughout this work,  $x$  corresponds to light propagation direction parallel to the waveguide axis,  $y$  to lateral direction and  $z$  to vertical direction. Physical quantities holding a subscript index  $j$  are assigned either to the NIR wave for  $j = 1$  or to the SH wave for  $j = 2$ .

### 4.4.1 System of coupled equations

The simulated electric field distributions  $\mathfrak{E}_j(y, z)$  of the waveguide lowest-order mode for the fundamental ( $j=1$ ) and SH ( $j=2$ ) wave presented in Fig. 3.6 allow to determine the effective cross-section  $S_{yz}$  according to Eq. (3.58). A relation between the optical power  $P_j$  and a scalar value of electric field amplitude  $\mathcal{A}_j$  can then be determined according to [180]:

$$\mathcal{A}_j = \sqrt{\frac{P_j}{S_{yz}} \cdot \frac{2}{n_j \epsilon_0 c_0}}, \quad (4.3)$$

provided that the definition of intensity  $\mathcal{J}_j$  from Eq. (3.31) is applied. The scalar value of the electric field amplitude  $\mathcal{A}_j$  from Eq. (4.3) is then applied in the system of coupled equations (Eqs. (3.27-3.29)) in Sect. 3.2.2:

$$\frac{d\mathcal{A}_0}{dx} = \Delta k_{\text{QPM}} - \left(2\sigma_1 \mathcal{A}_2 - \sigma_2 \frac{\mathcal{A}_1^2}{\mathcal{A}_2}\right) \cos \mathcal{A}_0 \quad (4.4)$$

$$\frac{d\mathcal{A}_1}{dx} = -\sigma_1 \mathcal{A}_1 \mathcal{A}_2 \sin \mathcal{A}_0 - \frac{1}{2} (\delta_1 + \delta_{\text{GRIIRA}} \mathcal{A}_2^4) \mathcal{A}_1 \quad (4.5)$$

$$\frac{d\mathcal{A}_2}{dx} = \sigma_2 \mathcal{A}_1^2 \sin \mathcal{A}_0 - \frac{1}{2} (\delta_2 + \delta_{2 \text{ Ph.}} \mathcal{A}_2^2) \mathcal{A}_2, \quad (4.6)$$

which is additionally supplemented by absorption coefficients:  $\delta_j$  is the linear loss coefficient [111],  $\delta_{\text{GRIIRA}} = \alpha_{\text{GRIIRA}} (n_2 \epsilon_0 c_0 / 2)^2$  where  $\alpha_{\text{GRIIRA}}$  is the green induced infrared absorption (GRIIRA) coefficient [151, 148],  $\delta_{2 \text{ Ph.}} = \beta_{2 \text{ Ph.}} n_2 \epsilon_0 c_0 / 2$  where  $\beta_{2 \text{ Ph.}}$  is the two-photon absorption coefficient for the SH wave [154]. Please note, that in case of GRIIRA the loss increases quadratically and in case of the two-photon absorption the loss increases linearly with increasing SH intensity, as described in [151] and [154], respectively.

### 4.4.2 Quasi phase-matching condition

The phase mismatch parameter from Eq. (3.39) has to be supplemented by further dependencies. The deviation from the sinc<sup>2</sup> function in Fig. 4.8 results from an inhomogeneity in the waveguide height  $h$ , as has been indicated by the crystal manufacturer. Therefore, a variation of this parameter at a homogeneous temperature  $T$  along the  $x$  coordinate is assumed in the theoretical model. Its distribution is discussed below in Sect. 4.6. The resulting phase mismatch parameter is presented in Eq. (4.7):

$$\Delta k_{\text{QPM}}(x, T) = 2\beta_1(h, T) - \beta_2(h, T) + \frac{2\pi}{\Lambda(x, T)}. \quad (4.7)$$

In the experiment the fundamental wavelength does not change and it can be considered as a constant in the above formula.

### 4.4.3 Heat and temperature distribution

The temperature  $T_{\text{RW}}$  inside of the waveguide structure may change along the crystal length due to heat generation resulting from the optical absorption.

Since waveguide height  $h$ , QPM period  $\Lambda$  as well as the effective refractive index  $N_j$  depend on the temperature, the  $T_{\text{RW}}$  distribution can influence the QPM condition from Eq. (4.7). In order to estimate the influence of the optical absorption on the temperature distribution along the propagation direction, a 1-dimensional steady-state heat transfer model is introduced in the theoretical model.

For this purpose, a 1-dimensional structure presented in Fig. 4.11 (a) is considered, which represents in a simplified manner the ridge waveguide and the slab of the SHG waveguide device (please compare Fig. 3.5). Due to the air gap present below the slab, a 1-dimensional consideration of the thermal problem is justified. The parameters  $w_{\text{RW}}$  and  $w_{\text{slab}}$  denote the ridge waveguide width

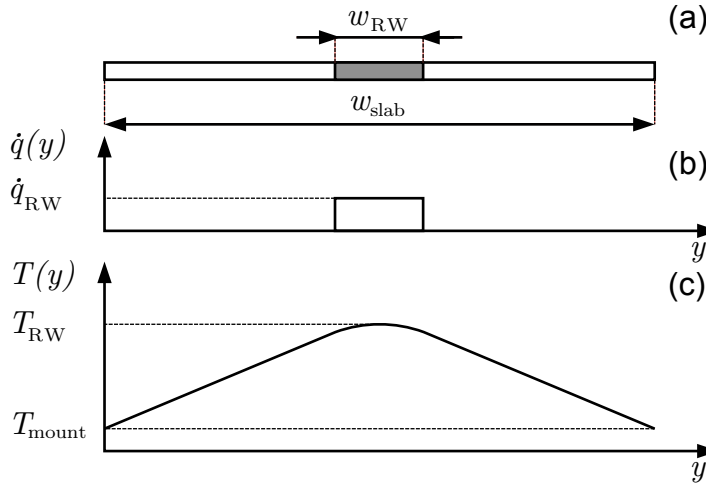


**Figure 4.11:** Schematic of the 1-dimensional structure representing in a simplified manner the ridge waveguide and the slab (a), the distribution of the heat source density (b), the resulting qualitative distribution of the temperature (c)

and the slab width, respectively. For this model a 1-dimensional, steady-state heat diffusion equation [181] of the form:

$$-k_{\text{cr}} \frac{\partial^2 T(y)}{\partial y^2} = \dot{q}(y) \quad (4.8)$$

is defined, with the Dirichlet boundary conditions

$$T(y = 0) = T(y = w_{\text{slab}}) = T_{\text{mount}}, \quad (4.9)$$

where  $k_{\text{cr}}$  is the crystal heat conductivity,  $T$  is the crystal temperature,  $y$  is the lateral coordinate. The heat source density is defined as a boxcar function for simplicity:

$$\dot{q}(y) = \begin{cases} \dot{q}_{\text{RW}} & \text{for } \frac{w_{\text{slab}} - w_{\text{RW}}}{2} < y < \frac{w_{\text{slab}} + w_{\text{RW}}}{2} \\ 0 & \text{otherwise} \end{cases} \quad (4.10)$$

and is restricted to the ridge waveguide interval, as can be seen in Fig. 4.11 (b).

Eq. (4.8) can be solved by applying the Green's function ansatz [182] and the qualitative solution is presented in Fig. 4.11 (c). The temperature in the middle of the slab, defined as

$$T\left(\frac{w_{\text{slab}}}{2}\right) = \frac{\dot{q}_{\text{RW}}}{4k_{\text{cr}}} \left[ w_{\text{slab}} w_{\text{RW}} - \frac{w_{\text{RW}}^2}{2} \right] + T_{\text{mount}}, \quad (4.11)$$

is applied in the system of coupled equations (Eqs. (4.4-4.6)) as the temperature of the ridge waveguide  $T_{\text{RW}}$  for simplification. A substitution of the boxcar function from Eq. (4.10) with a Gaussian distribution leads to a marginally small deviation from this value.

The temperature of the ridge waveguide can be calculated independently for every  $x$  position along the propagation direction:

$$T_{\text{RW}}(x) = \frac{\dot{q}_{\text{RW}}(x)}{4k_{\text{cr}}} \left[ w_{\text{slab}} w_{\text{RW}} - \frac{w_{\text{RW}}^2}{2} \right] + T_{\text{mount}}. \quad (4.12)$$

Please note, that the heat diffusion along the propagation direction  $x$  is not included in the introduced model. The heat source density depends on the NIR and SH intensity and is defined according to [154] by:

$$\dot{q}_{\text{RW}}(x) = -\frac{d}{dx}(\mathcal{J}_1(x) + \mathcal{J}_2(x)) \quad (4.13)$$

$$= (\alpha_1 + \alpha_{\text{GRIIRA}} \mathcal{J}_2^2) \mathcal{J}_1 + (\alpha_2 + \beta_{2\text{Ph}} \mathcal{J}_2) \mathcal{J}_2, \quad (4.14)$$

where  $\alpha_j$  is the linear optical absorption coefficient [152],  $\alpha_{\text{GRIIRA}}$  and  $\beta_{2\text{Ph}}$  are the GRIIRA coefficient and the two photon absorption coefficient, respectively, introduced in Sect. 4.4.1. Please note that the linear optical absorption coefficient  $\alpha_j$  is, in general, not equal to the linear loss coefficient  $\delta_j$  from Eq. (4.5) and Eq. (4.6), since optical loss in ridge waveguides originates also from scattering [44].

## 4.5 Exemplary simulation models

In this section exemplary simulation models for the present ridge waveguide structure are considered. In particular, the influence of the geometrical inhomogeneity and of the nonlinear absorption on the SHG process is investigated.

Results of simulations reflecting the influence of the geometrical inhomogeneity on the SH power distribution in dependence on the crystal mount temperature are presented in Fig. 4.12 and 4.13. A linear slope in the distribution of the waveguide height  $h$  along the propagation direction  $x$  (Fig. 4.12 (a)) leads to a modification of the SH power distribution in dependence on the crystal mount temperature (Fig. 4.12 (b)). With increasing difference between the waveguide height on both ends of the waveguide, the maximum SH power decreases and multiple side lobes arise symmetrically on both sides of the central peak. In addition, due to an increase of the average waveguide height, the SH power distribution shifts to a higher crystal mount temperature.

A parabolic variation of the waveguide height  $h$  along the propagation direction  $x$  (Fig. 4.13 (a)) also leads to a modification of the corresponding SH power distribution characterized by a decrease in the maximum SH power and a shift to a higher crystal mount temperature (Fig. 4.13 (b)). However, in this case the initially symmetric curve resembling a sinc<sup>2</sup> distribution becomes asymmetric. With increasing waveguide height inhomogeneity, the maximum

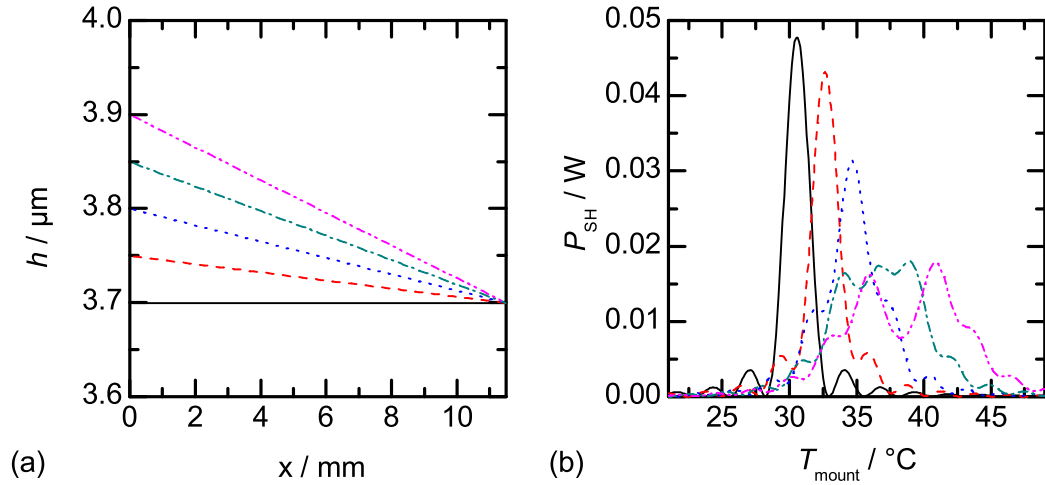


**Figure 4.12:** Simulated waveguide height distribution presented at  $T_{\text{mount}} = 25^\circ\text{C}$  and  $P_{\text{pump}} = 0$  W (a) and corresponding SH power dependence on the crystal mount temperature  $T_{\text{mount}}$  at an NIR pump power  $P_{\text{pump}} = 162$  mW (b); further parameters set according to Tab. 4.1

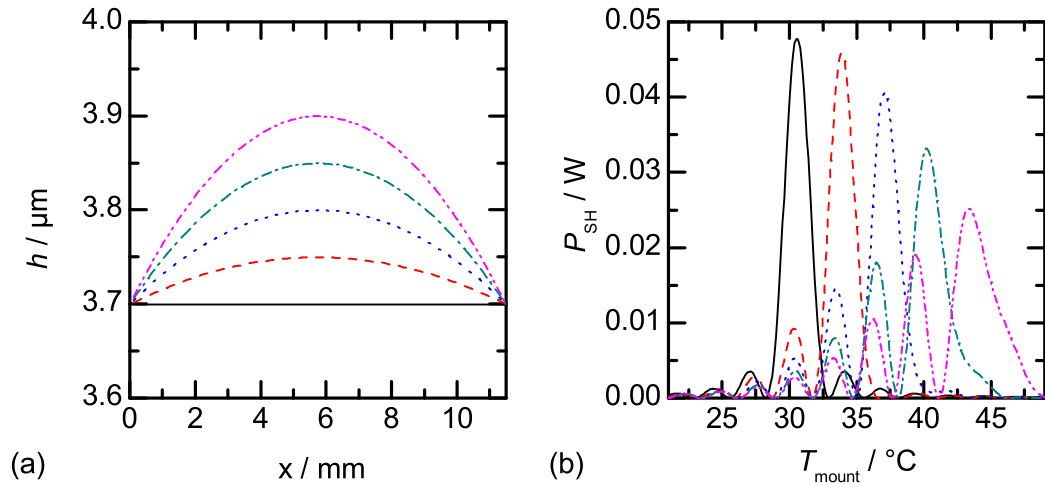


**Figure 4.13:** Simulated waveguide height distribution presented at  $T_{\text{mount}} = 25^\circ\text{C}$  and  $P_{\text{pump}} = 0$  W (a) and corresponding SH power dependence on the crystal mount temperature  $T_{\text{mount}}$  at an NIR pump power  $P_{\text{pump}} = 162$  mW (b); further parameters set according to Tab. 4.1

SH power decreases and multiple side lobes on one side of the main peak arise. These simulation results show clearly, that an experimental investigation of the SH power distribution as a function of the crystal mount temperature provides information about the homogeneity of a given waveguide SHG device.

Results of simulations incorporating increased values of nonlinear absorption coefficients are presented in Fig. 4.14. The SH power in dependence on the

NIR pump power in front of the ridge waveguide for different values of the two-photon absorption coefficient and of the GRIIRA coefficient is shown in Fig. 4.14 (a) and (b), respectively. For every NIR power value an optimum crystal mount temperature is considered in the simulation in order to ensure a maximum corresponding SH power. The increase in the two-photon absorption affects the SHG process in the ridge waveguide at lower SH and NIR pump powers compared to the variation of GRIIRA. However, elevated values of the GRIIRA coefficient lead to a saturation of the SH power with increasing NIR pump power in the investigated range. The adjustment of these two coefficients must be undertaken in order to reproduce the results of measurements, as will be shown in the following section.

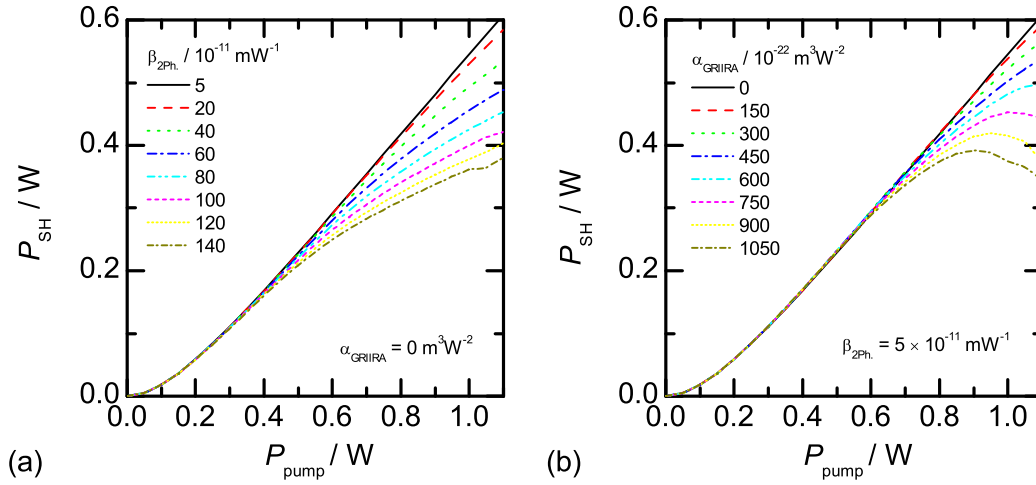


**Figure 4.14:** Simulated maximum SH power vs. NIR pump power for different values of the two-photon absorption coefficient (a) and the GRIIRA coefficient (b); further parameters set according to Tab. 4.1 and Fig. 4.15

## 4.6 Comparison between results of experiment and simulation

Initially, the inhomogeneity distribution, which leads to the SH power dependency on crystal mount temperature (open and filled triangles) at an NIR pump power of 162 mW presented in Fig. 4.8, is detected. At this power level, corresponding to a fundamental and SH power density of  $\mathcal{J}_1 \approx 1.0 \text{ MW/cm}^2$  and  $\mathcal{J}_2 \approx 0.4 \text{ MW/cm}^2$ , the optical absorption and resulting heat load are expected to be marginally small and not to influence the temperature curve distribution. As a result, for an asymmetric, quadratic distribution of the waveguide thickness  $h(x)$  along the waveguide axis, presented in Fig. 4.15, the temperature curve dependency determined experimentally can be exactly reproduced, as can be seen in Fig. 4.16 (a) and (b) in linear and logarithmic scale, respectively. Similar inhomogeneity influence has already been observed

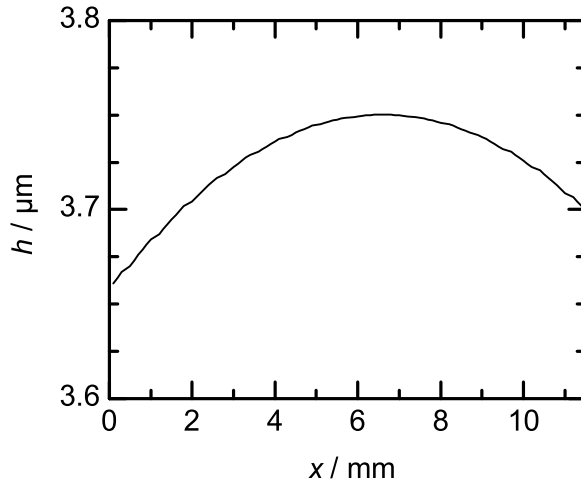


**Figure 4.15:** Theoretical distribution of the waveguide height  $h$  along the propagation direction  $x$  applied in the simulation ( $T_{\text{mount}} = 25^\circ\text{C}$ ,  $P_{\text{pump}} = 0\text{ W}$ )

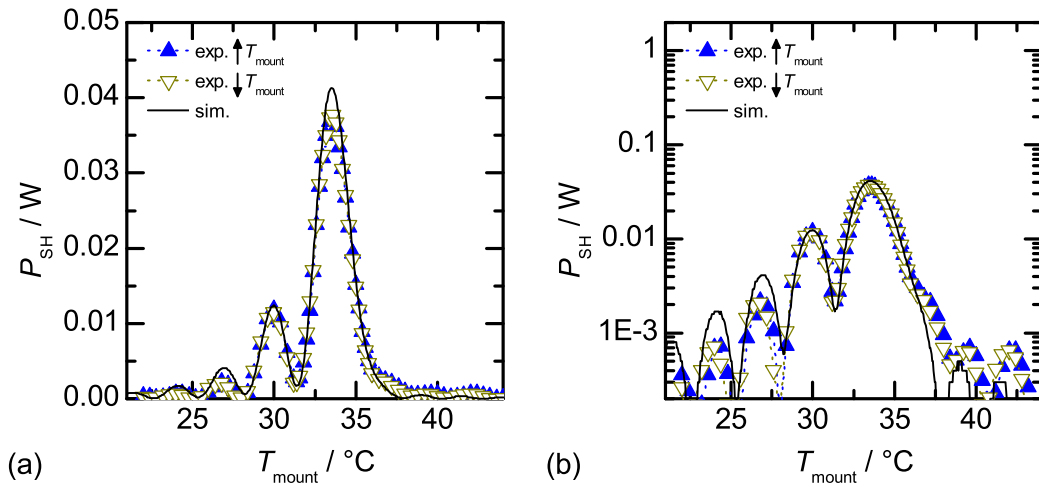
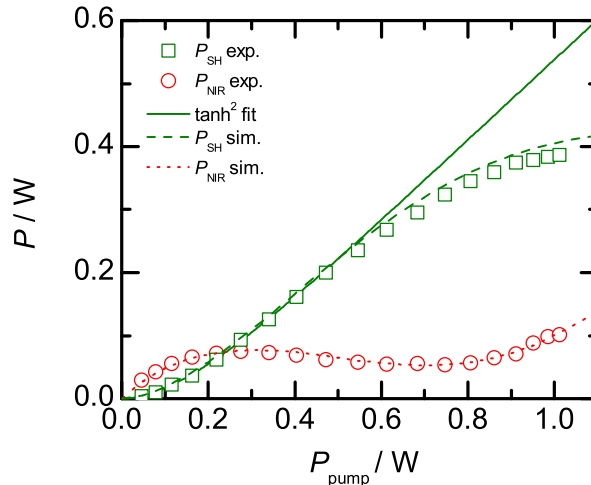


**Figure 4.16:** Measured and simulated SH power dependence on the crystal mount temperature  $T_{\text{mount}}$  at an NIR pump power  $P_{\text{pump}} = 162\text{ mW}$

in [94, 126].

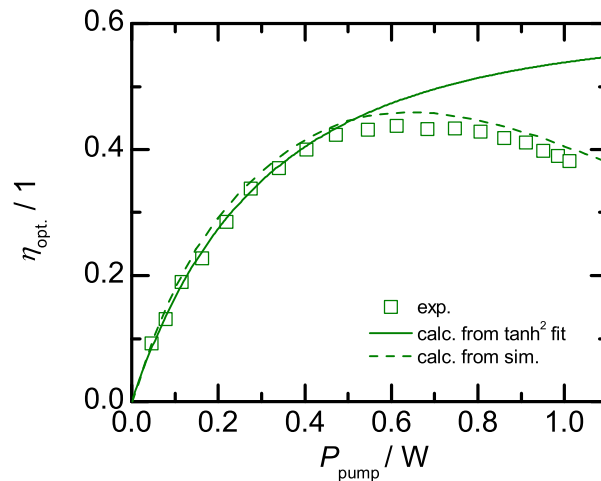
In the following step, the SH and NIR power behind the crystal for increasing NIR pump power in front of the crystal and optimum crystal mount temperature are calculated and compared with the measurements presented in Fig. 4.6. In order to reproduce the experimentally determined dependency, in particular the deviation from the  $\tanh^2$  fit above  $P_{\text{SH}} \approx 200\text{ mW}$ , higher absorption coefficients, than those known from the literature, have to be considered. The two-photon absorption coefficient has to be increased from  $5 \cdot 10^{-11}$  [134, 154] to  $60 \cdot 10^{-11}\text{ m/W}$ . Additionally, the intensity dependent GRIIRA coefficient [151] of  $450 \cdot 10^{-22}\text{ m}^3/\text{W}^2$  has to be applied. Higher nonlinear absorption coefficients lead to a consistency between the simulation and experiment in terms of SH and NIR power (Fig. 4.17; dashed and dotted curve, respectively), of the opto-optical conversion efficiency (Fig. 4.18; dashed curve) and of the overall transmitted power during the SHG process (Fig. 4.19 (a); solid curve).

**Figure 4.17:** Measured and simulated power behind vs. NIR pump power in front of the nonlinear crystal



The presence of intensity dependent GRIIRA [151] can be attributed to very high intensities inside of the ridge waveguide in excess of  $1 \text{ MW/cm}^2$  compared to the intensities, at which GRIIRA has been investigated in ppMgO:LN in the past [144, 148]. The increase in the two-photon absorption coefficient cannot

**Figure 4.18:** Measured and simulated opto-optical conversion efficiency vs. NIR pump power in front of the nonlinear crystal



be explained in the same way, since this coefficient has been determined experimentally in LN at even higher intensities [153]. However, in the introduced theoretical model it is not possible to provide such a good agreement between simulation and experiment by adjusting only one of the nonlinear absorption coefficients. The necessity to increase the two-photon absorption coefficient in the simulation might therefore originate from the simplifications undertaken in the model itself. On the other hand, effects such as newly reported multiphoton absorption [183] or pyroelectrically induced photorefractive damage in MgO:LN [184] could influence the nonlinear absorption in ridge waveguide structures. A systematic investigation of nonlinear absorption in ppMgO:LN is necessary to experimentally confirm the increase in the corresponding coefficients, it is however not the scope of this work.

In addition, the linear absorption coefficients are adjusted in the simulation

based on the experimentally determined optimum crystal mount temperature dependency (open circles) on increasing NIR pump power presented in Fig. 4.7 (b). The linear optical absorption coefficients  $\alpha_1$  and  $\alpha_2$  have to be

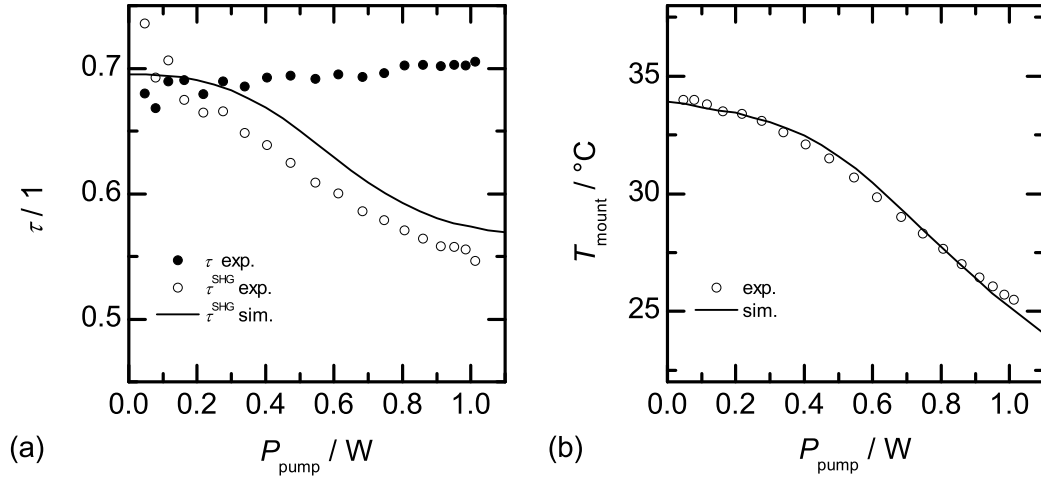


**Figure 4.19:** Transmission through the ridge waveguide with and without quasi phase-matching (a) and the crystal mount temperature  $T_{\text{mount}}$  during SHG process (b) vs. NIR pump power  $P_{\text{pump}}$  in front of the nonlinear crystal

increased from 0.2 1/m [134, p. 159] to 5.2 1/m and from 1.0 1/m [152] to 6.0 1/m, respectively. These elevated values amount to approximately one third part of the linear loss coefficient  $\delta_j$  of 18 1/m determined in [111] for the applied ridge waveguide structure. For these changes the simulated optimum mount temperature (Fig. 4.19 (b); solid curve) shows a good agreement with the experiment.

Consequently, for adjusted absorption coefficients the simulated SH power dependency on crystal mount temperature at an NIR pump power of  $P_{\text{pump}} = 747$  mW (Fig 4.20; solid curve) shows a relatively good agreement with the experimentally determined distributions (open and filled triangles). In particular, the simulated distribution contains similar side peaks at lower temperatures, a plateau at higher temperatures and an acceptance bandwidth (FWHM) of 1.2 K, which lies between the experimentally determined values for heating up and cooling down of the crystal mount (open and filled triangles). However, the introduced theoretical model does not allow to reproduce the experimentally observed hysteresis behavior, which most likely results from the fact, that it does not comprise the heat propagation along the waveguide axis (Sect. 4.4.3).

For parameters listed in Tab. 4.1 and for the inhomogeneity distributions from Fig. 4.15, the simulation is consistent with the experiment in the conservation of optical and thermal energy in the nonlinear crystal. Hence, both in the simulation and in the experiment the temperature of the crystal mount has to be reduced with the increasing SH output power in order to satisfy the QPM condition.

**Table 4.1:** Parameters applied in the simulation. Underlined are the values, which were increased or introduced in the simulation in order to match the experimental results

Symbol	Description	Unit	Value
$c_0$	light velocity in vacuum	m/s	$3 \cdot 10^8$
$\epsilon_0$	free space permittivity	F/m	$8.85 \cdot 10^{-12}$
$L_{\text{cr}}$	crystal length	mm	11.5
$h_{\text{RW}}$	RW thickness	$\mu\text{m}$	3.70
$w_{\text{RW}}$	RW width	$\mu\text{m}$	5.00
$w_{\text{slab}}$	slab width	$\mu\text{m}$	25.0
$k_{\text{cr}}$	heat conductivity	W/Km	4.60 [134]
$\alpha_{\text{CTE}}$	lin. thermal expan. coeff.	1/K	$15.4 \cdot 10^{-6}$
$\Lambda$	QPM period	$\mu\text{m}$	6.54
$d_{33}$	nonlinear coeff.	pm/V	25.2 [143]
$\lambda_1$	NIR wavelength	$\mu\text{m}$	1.061
$\eta_c$	coupling efficiency	1	0.857
$R_{\text{SH}}$	SH facet reflectivity	1	0.143
$S_{\text{eff}}$	eff. cross-section	$\mu\text{m}^2$	13.7
$\alpha_1$	lin. NIR abs. coeff.	1/m	<u>5.2</u> $\leftarrow$ 0.2 [134]
$\delta_1$	lin. NIR loss coeff.	1/m	18.4 [111]
$\alpha_{\text{GRIIRA}}$	GRIIRA abs. coeff.	$10^{-22} \text{ m}^3/\text{W}^2$	<u>450</u>
$\alpha_2$	lin. SH abs. coeff.	1/m	<u>6.0</u> $\leftarrow$ 1.0 [152]
$\delta_2$	lin. SH loss coeff.	1/m	18.4 [111]
$\beta_{2\text{Ph.}}$	two-photon abs. coeff.	$10^{-11} \text{ m}/\text{W}$	<u>60</u> $\leftarrow$ 5 [154]

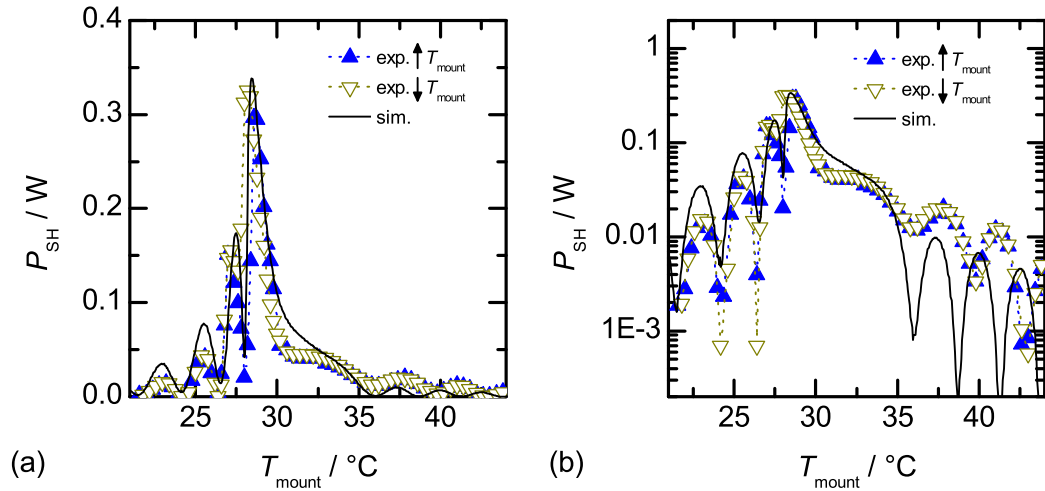


**Figure 4.20:** Measured and simulated SH power dependence on the crystal mount temperature  $T_{\text{mount}}$  at an NIR pump power  $P_{\text{pump}} = 747$  mW

The solution of the system of coupled equations (Eqs. (4.4 - 4.6)) for an NIR pump power  $P_{\text{pump}} = 162$  mW and an optimum crystal mount temperature  $T_{\text{mount}} = 33.5^\circ\text{C}$  is presented in Fig. 4.21 (a). The SH power  $P_{\text{SH}}$  (solid curve)

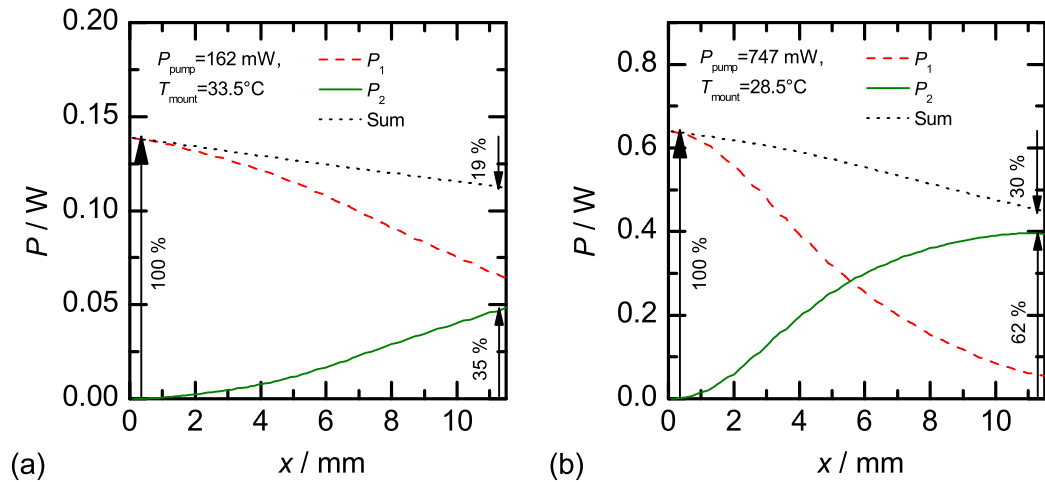


**Figure 4.21:** Simulated power distribution vs. propagation direction  $x$  for a parameter set  $T_{\text{mount}} = 33.5^\circ\text{C}$ ,  $P_{\text{pump}} = 162$  mW (a) and  $T_{\text{mount}} = 28.5^\circ\text{C}$ ,  $P_{\text{pump}} = 747$  mW (b)

increases with the propagation direction  $x$  at a cost of the fundamental power (dashed curve). The sum of both powers (dotted curve) decreases with the propagation distance  $x$  due to linear and nonlinear loss described in Sect. 4.4.1. A corresponding solution for  $P_{\text{pump}} = 747$  mW and  $T_{\text{mount}} = 28.5^\circ\text{C}$  is presented in Fig. 4.21 (b). Due to higher fundamental intensity in the ridge waveguide the energy flow rate from the fundamental (dashed curve) to SH wave (solid curve) is larger than in the example described above. Hence, an increase in

the internal conversion efficiency from 35 to 62 % can be observed. Due to nonlinear loss increasing with the increasing SH power the propagation loss through the waveguide increases from 19 to 30 % (dotted curve).

In Fig. 4.22 (a) the corresponding ridge waveguide temperature distribution along the waveguide axis is presented for NIR pump power value of 162 and 747 mW at a crystal mount temperature of 33.5 and 28.5 °C, respectively, at which the corresponding maximum SH power values are reached (Fig. 4.16 and 4.20). At  $P_{\text{pump}} = 162$  mW the ridge waveguide temperature distribution

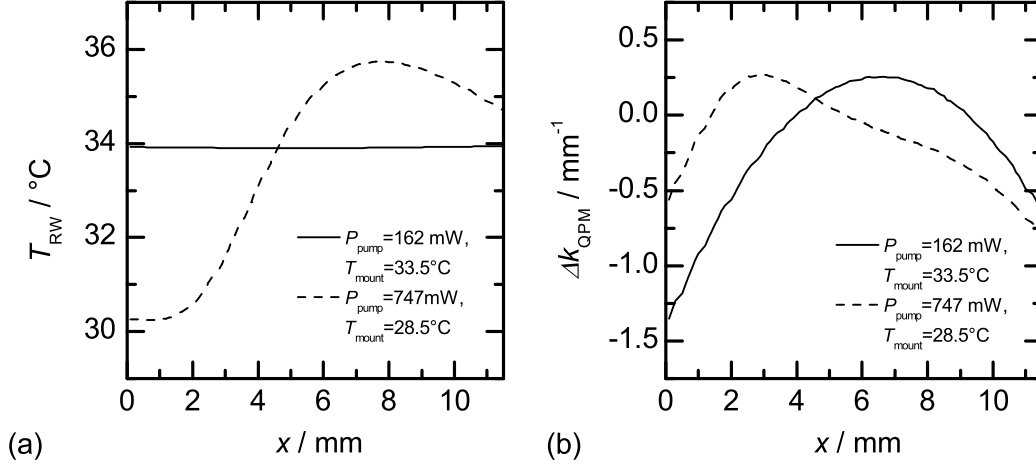


**Figure 4.22:** Simulated ridge waveguide temperature  $T_{\text{RW}}$  (a) and phase mismatch parameter  $\Delta k_{\text{QPM}}$  (b) vs. propagation direction  $x$

(solid curve) is constant around 33.8 °C and the corresponding phase mismatch parameter distribution, presented in Fig. 4.22 (b) as a solid curve, results only from the structural inhomogeneity shown in Fig. 4.15. At  $P_{\text{pump}} = 747$  mW the ridge waveguide temperature is very inhomogeneous (Fig. 4.22 (a), dashed curve) ranging from 30.2 to 35.7 °C, which is induced by the generated SH radiation. This leads to the phase mismatch parameter distribution presented in Fig. 4.22 (b) as a dashed curve and shows clearly that both the geometrical inhomogeneity as well as the temperature distribution inside of the waveguide influence its value at high power levels.

As can be seen in Fig. 4.23, for  $\beta_{2\text{Ph.}} = 5 \cdot 10^{-11}$  m/W [154, 134] and no GRIIRA present, the simulated SH power distribution in dependency on the NIR pump power agrees very well with the  $\tanh^2$  fit from Fig. 4.6. Additionally, in this case, a homogeneous waveguide SHG device with  $h(x) = \text{const.}$  (dash-dotted curve) exhibits slightly higher conversion efficiency over the whole NIR pump power range than an inhomogeneous device with  $h(x)$  from Fig. 4.15 (solid curve). However, if increased nonlinear absorption coefficients, determined in this work, are taken into consideration, higher SH power is reached with the device characterized by an inhomogeneity (dashed curve) than with a perfect device (dotted curve). This results from the interaction between the inhomogeneity distribution and the ridge waveguide temperature distribution along the

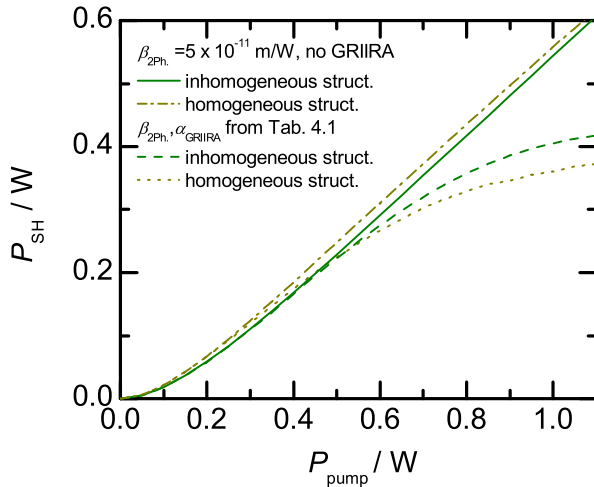


**Figure 4.23:** Simulated SH power  $P_{SH}$  vs. NIR pump power  $P_{pump}$  for a waveguide SHG device with homogeneous and inhomogeneous structure under assumption of absorption coefficients known from the literature or from Tab. 4.1

propagation direction  $x$ , both of which have influence on the phase mismatch parameter distribution, as is exemplarily presented above in Fig. 4.22.

The inhomogeneous distribution of the temperature  $T$  and of the phase mismatch parameter  $\Delta k_{QPM}$  along the waveguide axis due to changing absorption can be partly compensated by proper means. Specially tailored QPM gratings [122, 123] or segmented crystal heating [126, 185] might be applied to compensate the disadvantageous distribution. Embedding the ridge waveguides in materials characterized by high thermal conductivity might also enable higher SH powers, as the example of the experiments presented in [106] and [186] shows. Nonetheless, since the absorption limiting the maximum SH power increases with increasing SH intensity inside of the ridge waveguide, the intensity itself needs to be reduced at a cost of the conversion efficiency in order to provide considerably higher SH powers in the green spectral region. Planar waveguide structures are well suited for this purpose, as will be shown in the following chapter.

## 4.7 Summary

In this chapter, single-pass frequency doubling of a DBR-RWL emitting at 1061.0 nm in a ppMgO:LN ridge waveguide was investigated experimentally and theoretically.

In the experiment a coupling efficiency of  $\eta_c = (86 \pm 1) \%$  into the ridge waveguide was realized. A maximum second-harmonic power of  $P_{SH} = (386 \pm 15) \text{ mW}$  at an opto-optical and electro-optical conversion efficiency of  $\eta_{opt.} = (38 \pm 2) \%$  and  $\eta_{el.} = (9.6 \pm 0.4) \%$  was reached, respectively. An influence of a structural inhomogeneity on the SHG conversion efficiency as well as its gradual saturation at high output powers were observed experimentally.

A theoretical model for SHG in a ridge waveguide incorporating a system of coupled equations and a 1-dimensional, steady-state heat diffusion equation was introduced to describe qualitatively and quantitatively the effects mentioned

above. In this way, the structural inhomogeneity, increased values of absorption coefficients in ppMgO:LN, than reported in the literature up to date, and consequent heat generation and temperature increase in the ridge waveguide structure were considered in the simulation, whose results matched exactly the results obtained experimentally.

Nonlinear absorption increasing with increasing SH intensity is considered the main reason for the SH power saturation during experiments described in this chapter. The two-photon absorption and GRIIRA affect the SHG process starting from an SH wave intensity  $\mathcal{J}_2$  of approx.  $1.7 \text{ MW/cm}^2$ , which is reached at a fundamental wave intensity  $\mathcal{J}_1$  of approx.  $3.0 \text{ MW/cm}^2$  present at the beginning of the ridge waveguide. Above an SH wave intensity  $\mathcal{J}_2$  of approx.  $3.1 \text{ MW/cm}^2$ , reached at a fundamental wave intensity  $\mathcal{J}_1$  of approx.  $5.4 \text{ MW/cm}^2$ , a gradual saturation of the SH output power can be observed. This shows clearly, that for higher output powers in the green spectral region, the effective cross-section between the fundamental and SH wave needs to be enlarged in order to reduce the involved power density. Planar waveguide structures are well suited for this purpose, as will be presented in the following chapter.

## Chapter 5

# Diode laser frequency doubling in planar waveguides

The concept of SHG in a periodically poled MgO doped lithium niobate (ppMgO:LN) planar waveguide combines a free beam propagation in the lateral direction with a wave-guiding in the vertical direction. Planar waveguides enable higher output power compared to channel waveguides due to larger effective cross-section available for the nonlinear interaction and therefore a reduced power density. Opposite to bulk crystals, they provide higher conversion efficiency during the SHG process. Hence, they offer a compromise between a high output power and a high conversion efficiency.

Efficient single-pass SHG in planar waveguide structures has already been demonstrated experimentally [99, 104, 105, 107, 174]. Up to date a maximum SH power of 1.6 W at 532 nm with an opto-optical conversion efficiency of 40 % was reached during frequency doubling of a near-Gaussian pump beam from a solid state laser and a fiber amplifier in a ppMgO:LN planar waveguide [107]. In the same experiment a maximum conversion efficiency of 60 % at a maximum SH power of 1.2 W was achieved when a longer planar waveguide was applied. Though, with diode lasers as NIR pump sources comparable results could not be reached until now. Due to limited coupling efficiency a maximum SH output power of 0.35 W with an opto-optical conversion efficiency of 7.6 % was reported up to date [174]. Therefore, frequency doubling of diode lasers in quasi phase-matched planar waveguides needs to be investigated systematically in terms of optimum non-diffraction limited beam parameters for maximum coupling efficiency and maximum normalized SHG conversion efficiency as well as in terms of maximum accessible output power.

In this chapter, efficient high-power frequency doubling of a DBR tapered diode laser (DBR-TPL) in a ppMgO:LN planar waveguide is demonstrated. Prior to high-power experiments, a comprehensive experimental study of the SHG process subject to NIR pump beam parameters in the slow-axis is carried out. In particular, a consistent quantitative explanation of the inferior normalized SHG conversion efficiency for a DBR-TPL beam compared to a Gaussian beam is provided. In addition, a good agreement with theory for the experimental variation of lateral laser beam parameters is observed for both a near-Gaussian

beam and a DBR-TPL beam. These investigations allow to determine optimum NIR pump beam parameters with corresponding tolerances, which are adopted in subsequent efficient high-power frequency doubling of a DBR-TPL beam in planar waveguide structures.

This chapter is organized as follows: in Sect. 5.1 the frequency doubling of a near-Gaussian NIR pump beam is investigated. The frequency doubling of a DBR-TPL beam is presented in Sect. 5.2, including the description of the experimental setup (Sect. 5.2.1), the characteristics of the DBR-TPL beam (Sect. 5.2.2) and SHG experiments. Subsequent to investigation of SHG process as a function of NIR pump beam parameters in Sect. 5.2.3, the results of high-power frequency doubling of a DBR-TPL beam in planar waveguide structures and the generated SH beam properties are discussed in Sect. 5.2.4 and 5.2.5, respectively. Finally, in Sect. 5.3 a brief summary of this chapter is presented.

## 5.1 Frequency doubling of a near-Gaussian beam

Prior to frequency doubling of a DBR-TPL, SHG in a planar waveguide structure with a near-Gaussian beam is investigated. The experimental setup configured for this purpose and the characteristics of the employed NIR laser light source are presented below in Sect. 5.1.1 and 5.1.2, respectively. The results of frequency doubling of a near-Gaussian beam in planar waveguide structure and the properties of the generated SH beam are discussed in Sect. 5.1.3 and 5.1.4, respectively.

### 5.1.1 Experimental setup

The schematic of the experimental setup for SHG with a near-Gaussian beam in a planar waveguide is presented in Fig. 5.1. The 1 mm long and 5  $\mu\text{m}$  wide DFB ridge waveguide laser applied in this experiment as a pump source makes use of an epitaxial structure grown in two steps by MOVPE. It consists of an InGaAs double-quantum-well (DQW) embedded in a 4.8  $\mu\text{m}$  thick asymmetric AlGaAs waveguide core. The second order Bragg grating with coupling coefficient  $\kappa \approx 2.5 \text{ cm}^{-1}$  is realized by holographic photolithography and wet-chemical etching. The front and back facet are passivated and coated with a resulting reflectivity of 0 and 95 %, respectively. Further particulars on the device can be found in [49]. The laser chip is mounted p-side up on a c-mount holder and operated at  $T = 22.6 \text{ }^\circ\text{C}$ . Its divergent beam is collimated with an aspheric lens, L1 (C230TME-B from Thorlabs,  $f = 4.5 \text{ mm}$ ) followed by a HWP H1, the 60 dB optical isolator and a second HWP H2. In this experiment the NIR pump power is maintained constant whilst the transmission through the optical isolator is set to a maximum value. The laser radiation is coupled into a 2.0 m long polarization maintaining single-mode fiber PM-SMF (P1-980PM-FC-2 from Thorlabs) with an aspheric lens L2 (C240TME-B from Thorlabs,  $f = 8 \text{ mm}$ ). The PM-SMF enables a spatial mode filtration at a maintained polarization

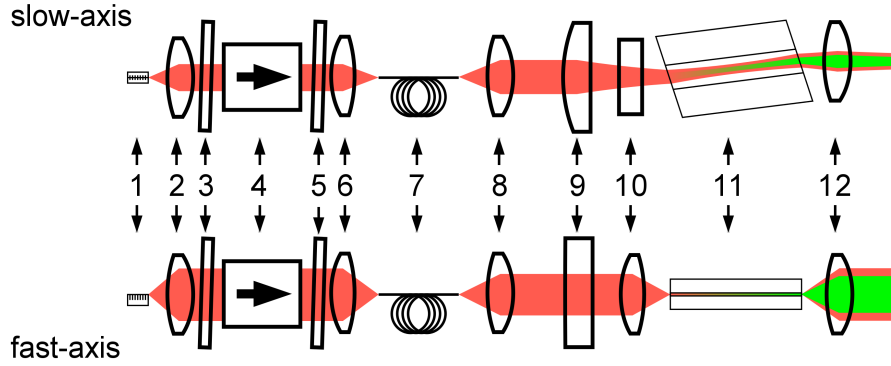


**Figure 5.1:** Schematic diagram of the frequency doubling setup: 1, DFB diode laser; 2, aspheric lens L1; 3, half-wave plate H1; 4, optical isolator; 5, half-wave plate H2; 6, aspheric lens L2; 7, PM-SMF; 8, aspheric lens L3; 9, cylindric lens L4; 10, acylindric lens L5; 11, nonlinear crystal with a planar waveguide; 12, aspheric lens L6

direction. The optics L1 and L2 are chosen according to simulation with WINABCD in order to maximize the coupling efficiency into the PM-SMF. An aspheric lens, L3 (A397TM-B from Thorlabs,  $f = 11$  mm) is used to collimate the laser radiation, which appears at the fiber output. The near-Gaussian beam is then focused into the planar waveguide with a cylindric lens, L4 (LJ1430L1-B from Thorlabs,  $f = 60$  mm), and an acylindric lens, L5 (cylindric lens with corrected surface profile for minimal cylindrical aberration, C10-08HPX from asphericon,  $f = 8$  mm), in the slow- and fast-axis, respectively. All optics applied in front of the crystal make use of a broadband anti-reflective (AR) coating in the range of 1064 nm.

The lenses L3 and L5 behind the PM-SMF are chosen according to simulations in order to maximize the coupling efficiency into the waveguide lowest-order mode. The cylindric lens L4 is chosen to focus the beam laterally in the planar waveguide according to simulations presented in Sect. 3.2.4 in order to reach a maximum SHG conversion efficiency. Additionally, the cylindric lens L4 can be moved along the optical axis or exchanged in order to relocate the lateral beam waist or in order to generate a different lateral beam waist diameter in the planar waveguide, respectively. During all experiments in this section the lateral beam waist is located in the middle of the nonlinear crystal in order to maximize the SHG conversion efficiency.

The planar waveguide sample L15-W500-WG1 applied in the experiment is described in detail in Sect. 3.3.3 (p. 34). A 500  $\mu\text{m}$ -wide waveguide sample is chosen for the experiment in order to ensure an undisturbed propagation in the lateral direction. The radiation behind the crystal is collimated in the fast-axis with an aspheric lens L6 (C240TME-A from Thorlabs,  $f = 8.0$  mm) AR coated for the SH radiation. In the slow-axis a small divergence remains behind this lens, but it does not influence the characterization of the generated SH laser beam. The dichroic mirror set (F73-767 from AHF analysentechnik AG) used to separate the SH and NIR wave is characterized by a total transmission of

0.88 and  $10^{-6}$  for the SH and NIR radiation, respectively, linearly polarized along the fast-axis. All results in this chapter concerning experiments on SHG with a near-Gaussian beam are presented without the losses originating from the collimating lens L6 and the dichroic mirror set.

### 5.1.2 Near-Gaussian beam characteristics

The power-voltage-current (PUI) characteristics of the DFB ridge waveguide diode laser applied in the experiment is presented in Fig. 5.2. Laser operation begins at a DFB threshold current of  $I_{\text{DFB, th}} = 0.020$  A and the optical power increases linearly with increasing current at a slope of 0.89 W/A. At a DFB

**Figure 5.2:** PUI-characteristics of the DFB diode laser applied in the experiment ( $T = 22.6^\circ\text{C}$ ,  $\Delta I_{\text{DFB}} = 0.001$  A)

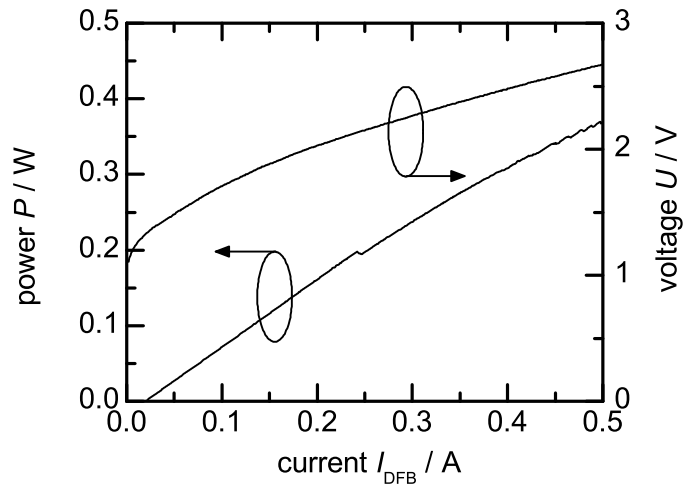
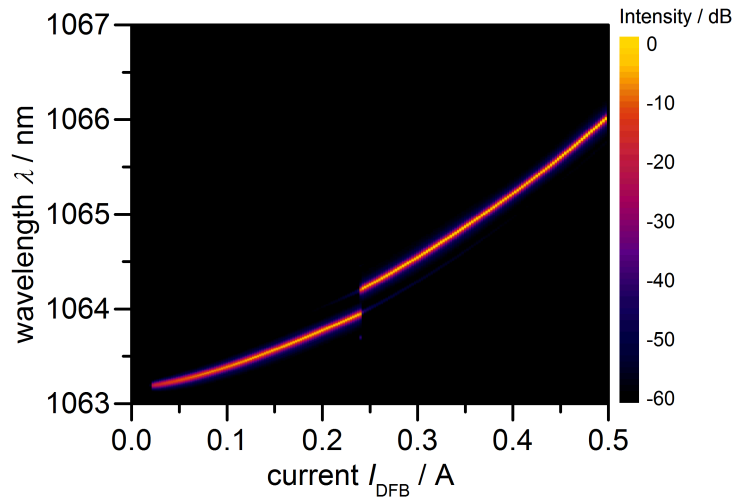


**Figure 5.3:** Spectral mapping of the DFB diode laser applied in the experiment ( $T = 22.6^\circ\text{C}$ ,  $\Delta I_{\text{DFB}} = 0.0025$  A)



current  $I_{\text{DFB}} = 240$  mA a kink in the power curve is visible, which results from a spectral instability.

The spectral mapping measured with an optical spectrum analyzer Q8384 from Advantest in 0.0025 A steps is presented in Fig. 5.3. The central wavelength lies at 1063.19 nm at the threshold and increases initially with the increasing DFB current at a rate of approx. 3.4 nm/A. At a DFB current  $I_{\text{DFB}} = 240$  mA

a spectral mode jump of 0.26 nm to a higher wavelength is visible, which correlates with the stop band width [49] and is consistent with the kink in the power curve from Fig. 5.2. This spectral instability results most likely from the thermally induced gain shift, which is approx. one order of magnitude higher than the thermal shift of DFB modes [49]. At higher output power a thermally induced wavelength drift of approx. 7.0 nm/A can be observed.

During the frequency doubling experiment, the DFB ridge waveguide diode laser is biased with  $I_{\text{DFB}} = 0.500$  A. The laser emits at a central wavelength of

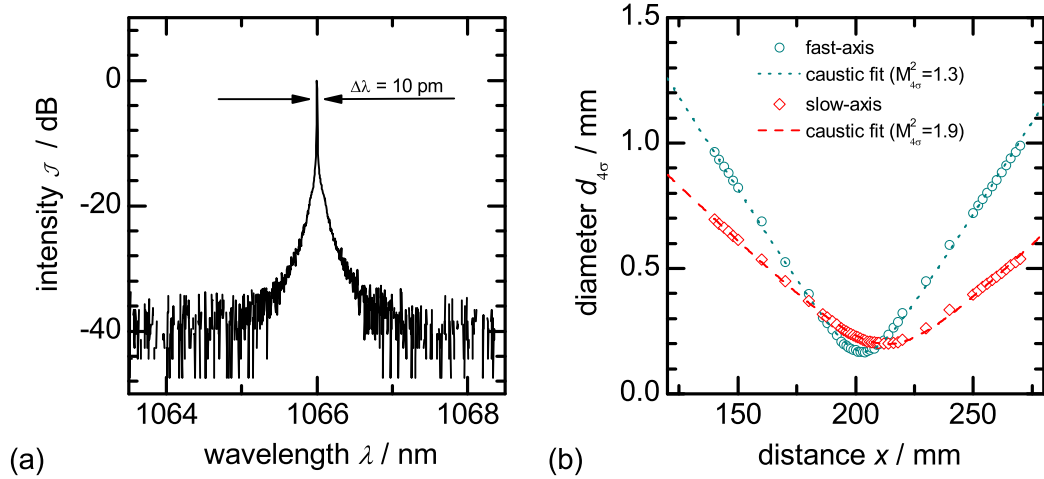


**Figure 5.4:** Spectrum (a) and caustic (b) of the DFB ridge waveguide diode laser beam at  $T = 22.6$  °C,  $I_{\text{DFB}} = 0.5$  A

1066.0 nm in a longitudinal single-mode, as can be seen in Fig. 5.4 (a), where the result of a spectrum measurement with a DEMON spectrometer (Appendix A.1) is presented. The spectral bandwidth of 10 pm (FWHM) as well as a noise level of  $-40$  dB, determined in the measurement, originate from the spectral resolution and the maximum signal-to-noise ratio of the applied spectrometer, respectively. The beam quality of the NIR beam is determined behind the half-wave plate H2. The beam propagation ratio  $M_{4\sigma}^2$  of 1.3 and 1.9 for the fast and slow-axis, respectively, results from a caustic measured according to the second order moments method, which is presented in Fig. 5.4 (b). When  $1/e^2$ -level method is applied to determine the beam diameters, beam propagation ratio  $M_{1/e^2}^2$  of 1.1 and 1.0 results in the fast and slow-axis, respectively.

The overall transmission through PM-SMF and the lenses used for coupling and collimating is determined to approx. 70 % and it remains constant throughout the experiment. The spectrum of the NIR radiation behind the single-mode fiber PM-SMF remains unchanged, as can be seen in Fig. 5.5 (a). The results of the caustic measurement according to second order moments behind the collimating lens L3 are presented in Fig. 5.5 (b). The beam propagation ratio  $M_{4\sigma}^2$  improves to a value of 1.1 in both fast- and slow-axis, compared to the corresponding values in front of the PM-SMF. Beam quality parameter  $M_{1/e^2}^2$  remains the same with values of 1.1 and 1.0 in the fast- and slow-axis, respectively.

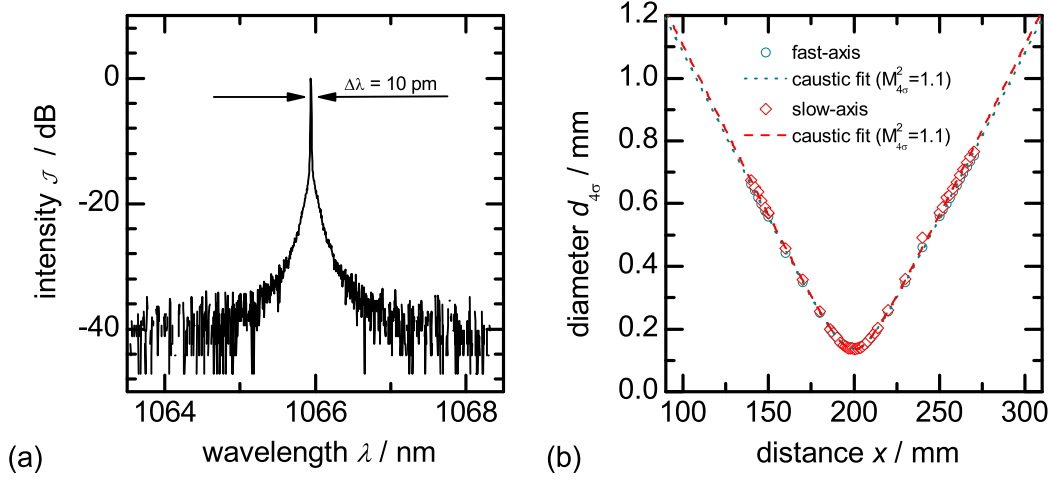


**Figure 5.5:** Spectrum (a) and caustic (b) of the near-Gaussian beam coupled from the single-mode fiber PM-SMF

The transmission through the optical isolator and the single-mode fiber PM-SMF of approx. 90 % and 70 %, respectively, and the residual reflections of optical surfaces result in a NIR pump power in front of the nonlinear crystal of  $P_{\text{pump}} = (0.20 \pm 0.01)$  W. This fundamental power value corresponds to a maximum power density  $\mathcal{J}_1$  inside of the planar waveguide of approx.  $0.1 \text{ MW/cm}^2$  for the optimum lateral focusing, and lies, therefore, in the intensity range, in which the SHG process is not affected by increased nonlinear absorption (compare Sect. 4.6).

The intensity distribution of the pump beam measured through a microscope

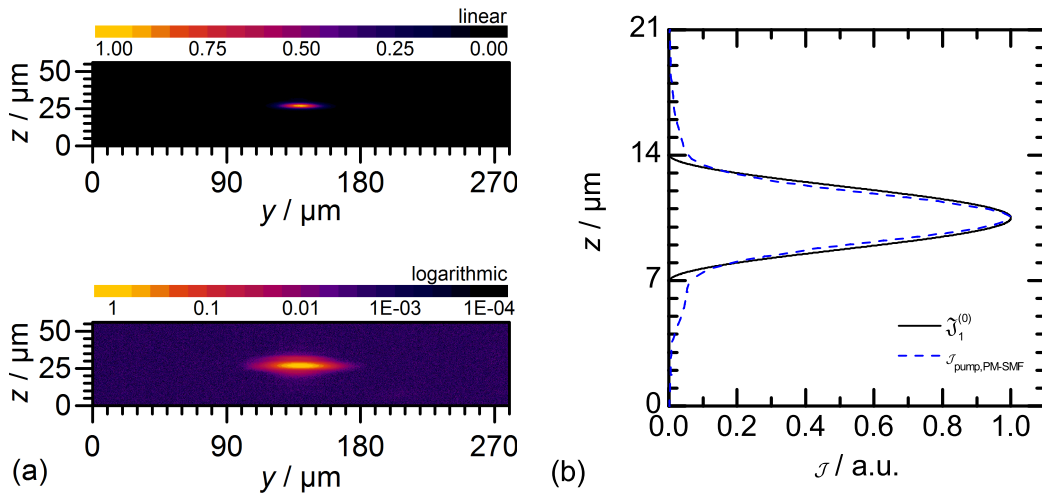


**Figure 5.6:** Measured 2-dimensional intensity distribution of the near-Gaussian beam in the the beam waist in front of the nonlinear crystal on linear and logarithmic scale (a). Projection of the measured intensity in the fast-axis  $\mathcal{J}_{\text{pump,PM-SMF}}$  and the simulated waveguide lowest-order mode intensity  $\hat{\mathcal{J}}_1^{(0)}$  (b)

objective (Appendix A.1) in the focal points of the cylindrical lens L4 and of the acylindrical lens L5 is presented in Fig. 5.6 (a) on linear and logarithmic scale. The vertical and lateral  $1/e^2$  threshold beam waist diameters of  $(5.3 \pm 1.1)$  and  $(39 \pm 4)$   $\mu\text{m}$ , respectively, agree well with the diameters resulting from beam propagation simulation conducted with WINABCD between the PM-SMF output and the nonlinear crystal front facet. The measured distribution contains no intensity values beyond the beam diameter, as can be seen on the logarithmic scale.

The projection of the intensity distribution in the fast-axis measured in the beam waist is presented in Fig. 5.6 (b) as a dashed curve. It agrees well with the 1-dimensional waveguide lowest-order mode intensity profile (solid curve), simulated with FIMMWAVE for the applied waveguide structure. The simulated waveguide lowest-order mode is characterized by a  $1/e^2$  threshold diameter of 5.4  $\mu\text{m}$ . Based on these two distributions the coupling efficiency into the waveguide lowest-order mode can be predicted theoretically. Calculation of the overlap integral from Eq. (3.6) results in a coupling efficiency of 92 %.

Prior to SHG experiments, the transmission through the planar waveguide sample L15-W500-WG1 is determined experimentally by measuring the NIR pump power behind and in front of the nonlinear crystal. For this purpose the crystal mount temperature is set to 20 °C, at which the QPM condition for SHG is not fulfilled. The lateral beam waist is located in the middle of the nonlinear crystal, which leads to maximum conversion efficiency during SHG. As a result a transmission of  $\tau_{\text{Gauss}} = (85 \pm 6)$  % at an extraordinary polarization is determined. The deviation from the calculated coupling efficiency presented above originates most likely from the propagation loss in the planar waveguide structure.

### 5.1.3 SHG with a near-Gaussian beam

The measurement of the generated SH power at the crystal mount temperature providing quasi phase-matching allows to determine the maximum normalized SHG conversion efficiency of  $\bar{\eta}_{\text{SHG}} = (26 \pm 4)$  %  $\text{W}^{-1}$  calculated according to Eq. (3.62). This result corresponds to an effective nonlinear coefficient of  $d_{\text{eff,QPM}} = 13.5$  pm/V, which is in good agreement with values of  $d_{\text{eff,QPM}}$  for QPM SHG devices determined experimentally in other works [73, 158, 159]. The deviation from an expected value of 16 pm/V (Sect. 3.3.1) could originate from imperfections in the QPM structure such as inhomogeneity, missing reversals or boundary position errors (Sect. 3.2.3). An inhomogeneity in waveguide thickness  $h$  or in the crystal composition along the propagation direction could also lead to a decrease in the normalized SHG conversion efficiency.

In order to investigate the homogeneity of the waveguide SHG device L15-W500-WG1, the dependency of the generated SH power on the crystal mount temperature is measured. The resulting dependency of the normalized SHG conversion efficiency  $\bar{\eta}_{\text{SHG}}$  is presented as open squares in Fig. 5.7 (a) and (b) on linear and logarithmic scale, respectively. The measured distribution agrees rela-

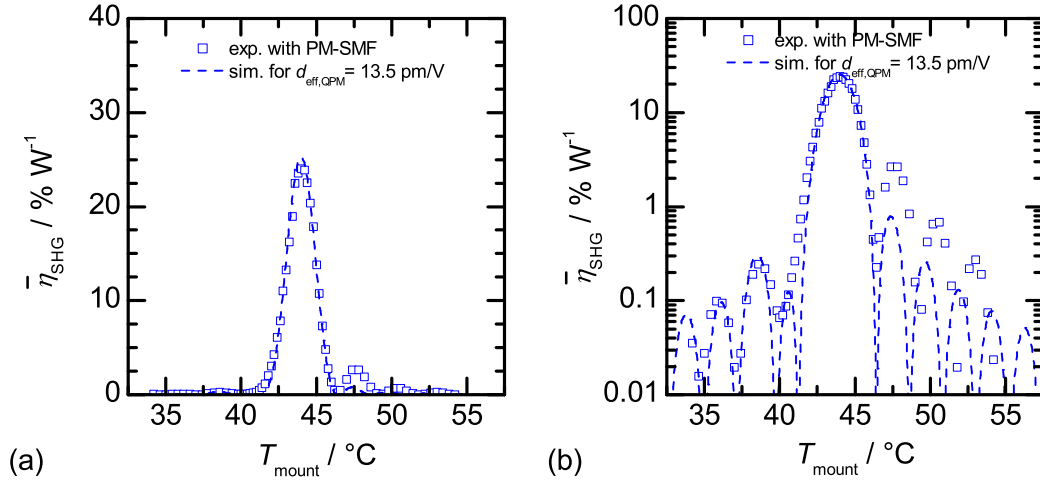


**Figure 5.7:** Simulated and measured normalized SHG conversion efficiency vs. the crystal mount temperature on linear (a) and logarithmic (b) scale

tively well with the results of simulation according to Eq. (3.47) (dashed curve), in which an effective nonlinear coefficient  $d_{\text{eff,QPM}} = 13.5$  pm/V is applied. The experimentally determined temperature bandwidth of  $\Delta T_{\text{FWHM}} = 2.1$  K complies with the theoretical value of 2.2 K and is consistent with the QPM region length. Increased side-peaks in the measured distribution, present at higher crystal mount temperature relative to main peak, indicate a small inhomogeneity in the QPM waveguide structure.

Unlike in bulk crystals, in planar waveguides only the NIR pump beam properties in the slow-axis influence the SHG conversion efficiency directly. The fast-axis beam characteristics determine the coupling efficiency into the waveguide lowest-order mode. The initially set lateral beam waist diameter is chosen according to simulations based on Fluck's theory for maximum SHG conversion efficiency. In order to validate the influence of the lateral focusing on the normalized SHG conversion efficiency in a planar waveguide experimentally, the cylindric lens L4 is exchanged with lenses characterized by different focal lengths. Analog experiments have already been conducted by McGeoch and Smith [64] for the theory of Boyd and Kleinman [21] in bulk crystals. During the experiment the lateral beam waist is placed in the middle of the nonlinear crystal for every successive lens. In Fig. 5.8 the resulting distribution of the normalized SHG conversion efficiency  $\bar{\eta}_{\text{SHG}}$  subject to  $1/e^2$  lateral beam waist diameter is presented as open squares. The measured values are consistent with the theoretical distribution (dashed curve), calculated according to Eq. (3.47) for an effective nonlinear coefficient  $d_{\text{eff,QPM}} = 13.5$  pm/V. The maximum value of  $\bar{\eta}_{\text{SHG}} = (26 \pm 4) \% \text{ W}^{-1}$  is reached at the  $d_{1/e^2,0} = (39 \pm 4) \mu\text{m}$ . Hence, the experiment confirms the theoretical predictions of Fluck's theory [132] and shows that the initially chosen beam waist diameter results in the maximum SHG conversion efficiency.

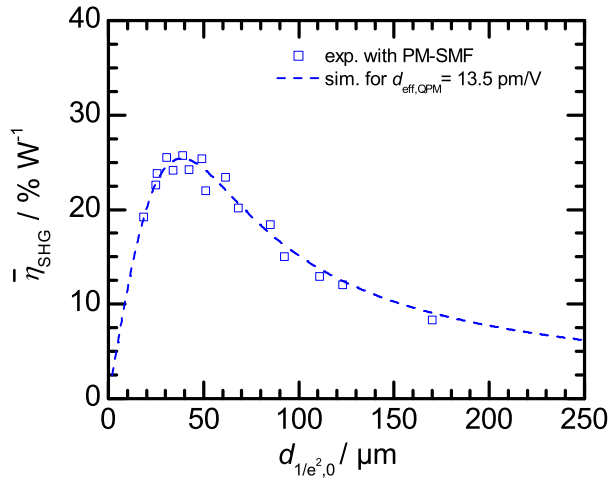


**Figure 5.8:** Simulated and measured normalized SHG conversion efficiency vs. the beam waist diameter

The discrepancy between experimentally determined effective nonlinear coefficient  $d_{\text{eff,QPM}}$  and the theoretical value is therefore attributed mainly to the QPM grating errors, which do not influence the shape of the temperature curve (Sect. 3.2.3, p. 26). Quantitatively, the measured discrepancy could originate from a fraction  $f = 7.9\%$  of domains with wrong orientation (Eq. (3.42)) or a duty cycle error ratio of  $\sigma_{l_c}/l_c = 26\%$  (Eq. (3.43)).

#### 5.1.4 SH beam characteristics

At an SH power  $P_{\text{SH}} = (7.0 \pm 0.4)$  mW, obtained at the maximum normalized SHG conversion efficiency of  $\bar{\eta}_{\text{SHG}} = (26 \pm 4)\% \text{ W}^{-1}$ , the generated SH beam is additionally characterized with respect to spectral and spatial properties.

The optical spectrum of the generated SH radiation measured with an ELIAS spectrometer (Appendix A.1) in double pass is presented in Fig. 5.9 (a). The

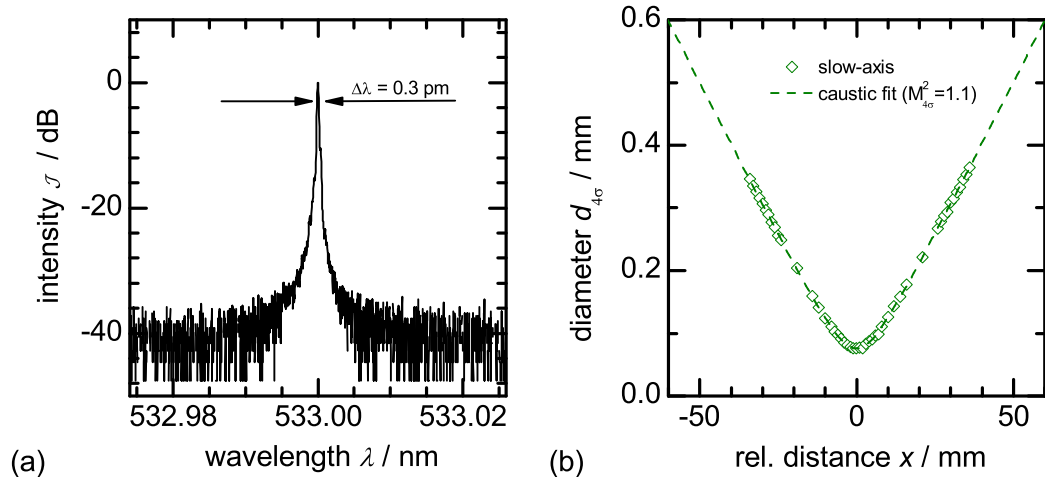


**Figure 5.9:** Spectrum (a) and caustic (b) of the SH beam generated by a near-Gaussian NIR pump beam

determined spectral bandwidth of 0.3 pm (FWHM) as well as a noise level of

–40 dB are limited by the spectral resolution and the maximum signal-to-noise ratio of the applied spectrometer, respectively.

Results of a caustic measurement in the slow-axis according to second order moments method are presented in Fig. 5.9 (b). The corresponding SH beam propagation ratio  $M_{4\sigma}^2$  of 1.1 shows that the beam quality upon SHG of a near-Gaussian beam in a planar waveguide structure remains unchanged. For  $1/e^2$  intensity level diameters a beam propagation ratio  $M_{1/e^2}^2$  of 1.0 is determined. The SH beam quality in the fast-axis is predetermined by the planar waveguide structure and results in a beam propagation ratio  $M_{4\sigma}^2$  and  $M_{1/e^2}^2$  of 1.3 and 1.0, respectively.

## 5.2 Frequency doubling of a DBR-TPL beam

Frequency doubling of a DBR-TPL beam in a planar waveguide is carried out in an experimental setup presented in Sect. 5.2.1. Prior to SHG experiments, in Sect. 5.2.2 the characteristics of the applied diode lasers and the NIR pump beams are described. In Sect. 5.2.3 the SHG process subject to NIR pump beam parameters is discussed based on experimental and theoretical results. Efficient high-power frequency doubling of a DBR-TPL radiation is demonstrated in Sect. 5.2.4. In Sect. 5.2.5 the spatial and spectral properties of the generated SH beam are described.

### 5.2.1 Experimental setup

The schematic of the experimental setup for frequency doubling of a DBR-TPL beam in a planar waveguide is presented in Fig. 5.10. The 6-mm-long DBR-TPLs applied in the experiment are described in detail in Sect. 2.3. The laser chip is mounted p-side up on a CuW heat spreader and assembled on a conduction-cooled packaging (CCP). The laser beam is collimated in the fast-axis with an aspheric lens, L1 (C230TME-B from Thorlabs,  $f = 4.5$  mm). An additional cylindric lens, L2 (LJ1402L2-B from Thorlabs,  $f = 40$  mm), is used to compensate the astigmatism induced by the tapered section while collimating the laser radiation in the slow-axis. The first HWP, H1, and the 60 dB optical isolator allow to adjust the NIR pump power in front of the nonlinear crystal without changing the properties of the laser beam. The second HWP, H2, is used to adjust the polarization of the NIR radiation. The laser beam is focused with a cylindric lens, L3 (LJ1567L1-B from Thorlabs,  $f = 100$  mm), and an acylindric lens, L4 (C10-08HPX from asphericon,  $f = 8$  mm), in the slow- and fast-axis, respectively. All optics applied in front of the nonlinear crystal make use of a broadband AR coating for the NIR range.

For the fast-axis the setup lens combination is chosen accordingly to simulations in order to maximize the coupling efficiency into the waveguide lowest-order mode of the fundamental wave. Taking measured spatial emission characteristics of the diode laser in the fast-axis into consideration, the beam propagation is simulated with WINABCD. An aspheric lens L1 with a numerical aperture

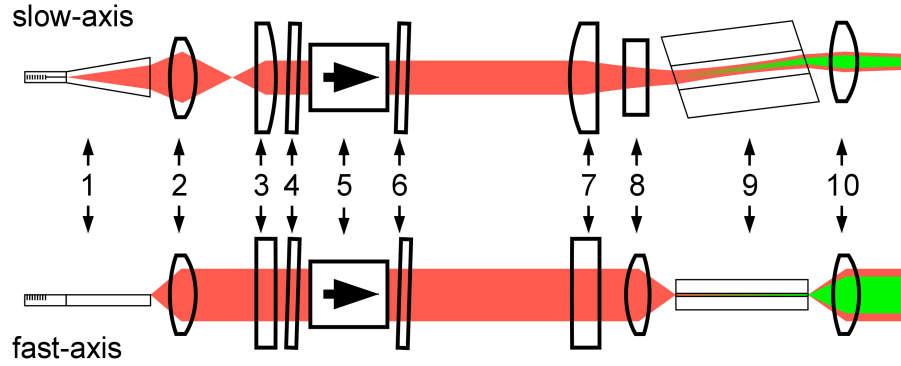


**Figure 5.10:** Schematic diagram of the frequency doubling setup: 1, DBR-TPL; 2, aspheric lens L1; 3, cylindric lens L2; 4, half-wave plate H1; 5, optical isolator; 6, half-wave plate H2; 7, cylindric lens L3; 8, acylindric lens L4; 9, nonlinear crystal with a planar waveguide; 10, aspheric lens L5

value  $NA = 0.55$  is chosen for collimation in order to minimize diffraction effects and in order to set the vertical diameter of the collimated beam to approx. one half of the smallest aperture diameter in the setup. The acylindric lens L4 is chosen in order to generate a beam waist intensity profile on the crystal facet conform to the waveguide lowest-order mode of the fundamental wave.

For the slow-axis the cylindric lens L2 is chosen according to simulations in order to generate a collimated beam with the lateral diameter of approx. one half of the smallest aperture diameter in the setup. The cylindric lens L3 is chosen to focus the beam laterally in the planar waveguide according to calculations discussed in Sect. 3.2.4 in order to reach a maximum SHG conversion efficiency. Additionally, the cylindric lens L3 can be moved along the optical axis in order to relocate the lateral beam waist in the planar waveguide. Furthermore, the cylindric lens L3 can be exchanged to generate a different lateral beam waist diameter in the planar waveguide.

The experiments regarding frequency doubling of a DBR-TPL beam are conducted in the planar waveguide samples described in detail in Sect. 3.3.3. The part of experimental setup behind the crystal resembles the experimental setup for frequency doubling of a near-Gaussian beam presented above in Sect. 5.1.1. All experimental results in this chapter concerning the frequency doubling of a DBR-TPL beam in a planar waveguide are presented without the losses originating from the collimating lens L5 and the dichroic mirror set.

## 5.2.2 Diode laser characteristics

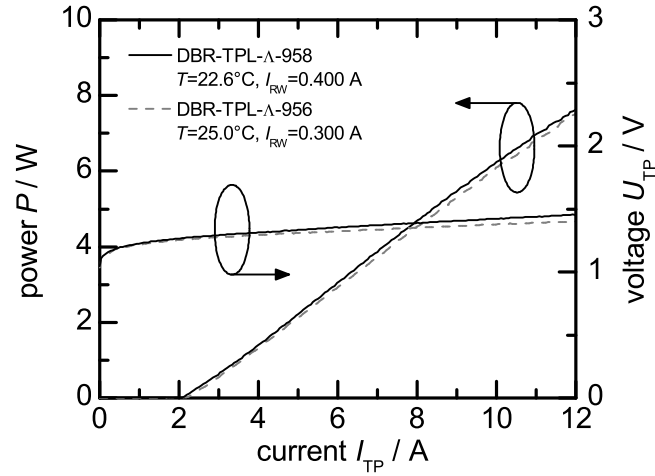
Two 6 mm long DBR-TPLs are applied during SHG experiments in planar waveguide samples. Both devices consist of the same epitaxial structure as well as the same lateral resonator design, which are described in Sect. 2.3. They differ however in the DBR grating period  $\Lambda_{\text{DBR}}$ , which amounts either to 958 or 956 nm. Therefore, the devices are denoted and referred to below as

## 5.2. Frequency doubling of a DBR-TPL beam

DBR-TPL- $\Lambda$ -958 and DBR-TPL- $\Lambda$ -956, respectively, and differ, consequently, in the emission wavelength  $\lambda$ .

The lasers DBR-TPL- $\Lambda$ -958 and DBR-TPL- $\Lambda$ -956 are operated at  $T = 22.6^\circ\text{C}$  and  $T = 25.0^\circ\text{C}$ , respectively, and their ridge waveguide sections are biased with  $I_{\text{RW}} = 0.400$  and  $0.300$  A, respectively. The power-voltage-current (PUI)

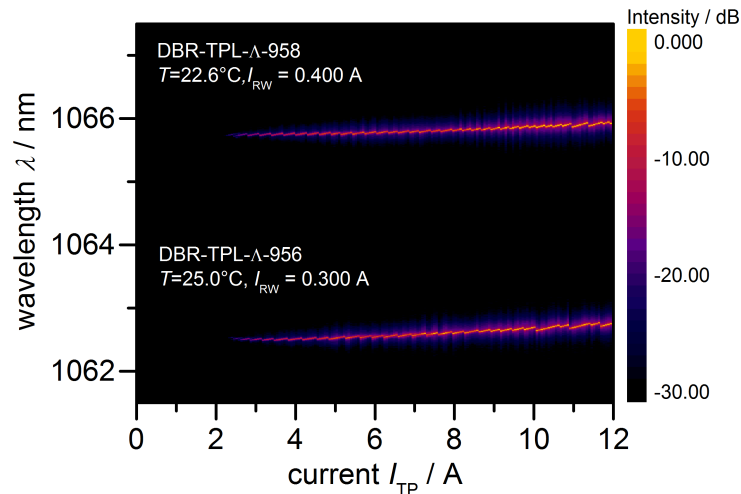
**Figure 5.11:** PUI characteristics of DBR-TPLs applied for SHG experiments in planar waveguide structures



characteristics of both lasers applied in the experiment is presented in Fig. 5.11. Laser operation begins at a taper threshold current of  $I_{\text{TP, th}} = 2.07$  and  $2.20$  A for laser DBR-TPL- $\Lambda$ -958 and DBR-TPL- $\Lambda$ -956, respectively. The optical power increases linearly with increasing current at a slope of approx.  $0.78$  W/A for both lasers.

The spectral mapping measured with DEMON spectrometer (Appendix A.1) in  $0.06$  A steps is presented in Fig. 5.12. The central wavelength lies at  $1065.7$

**Figure 5.12:** Spectral mapping of DBR-TPLs applied for SHG experiments in planar waveguide structures



and  $1062.5$  nm at the threshold current  $I_{\text{TP, th}}$  for laser DBR-TPL- $\Lambda$ -958 and DBR-TPL- $\Lambda$ -956, respectively, and increases with the increasing taper current at a rate of approx.  $0.019$  nm/A for both lasers. In case of both lasers, spectral longitudinal single-mode operation is given between mode-hops specific for

DBR lasers.

During frequency doubling experiments, the laser DBR-TPL- $\Lambda$ -958 is biased with  $I_{RW} = 0.400$  A and  $I_{TP} = 12.0$  A. The transmission of the optical isolator of approx. 90 % and the residual reflections of optical surfaces result in a maximum NIR pump power of  $P_{\text{pump}} = (5.9 \pm 0.2)$  W in front of the nonlinear crystal. The laser emits at a central wavelength of 1066.0 nm in a longitudinal single-mode, as can be seen in Fig. 5.13 (a). The determined spectral emission bandwidth of 10 pm (FWHM) as well as a noise level of  $-40$  dB are limited by the spectral resolution and the maximum signal-to-noise ratio of the applied DEMON spectrometer (Appendix A.1), respectively.

The beam quality of the NIR beam is measured behind the half-wave plate H2 (see setup schematics in Fig. 5.10). The caustic determined according to second

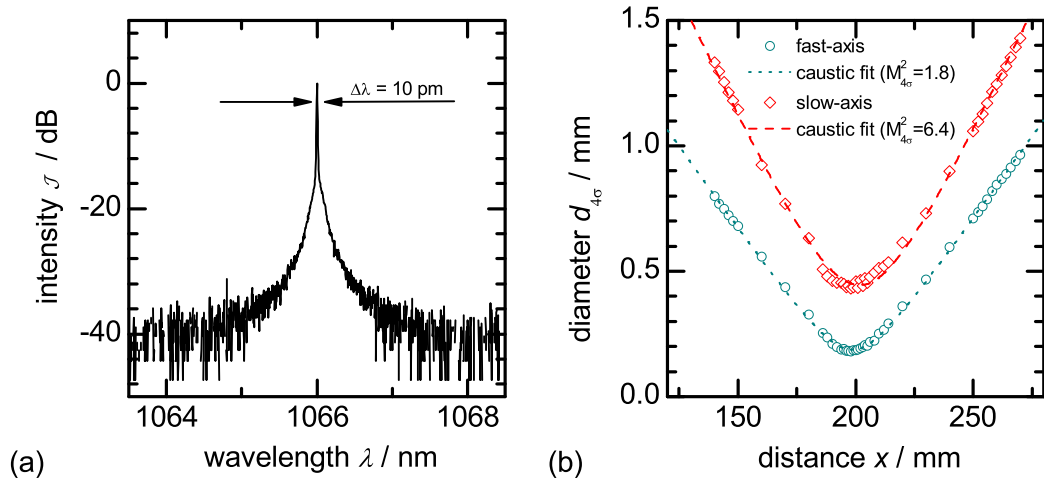


**Figure 5.13:** Spectrum (a) and caustic (b) of the DBR-TPL- $\Lambda$ -958 beam at  $T = 22.6$  °C,  $I_{RW} = 0.400$  A,  $I_{TP} = 12.0$  A

order moments method, presented in Fig. 5.13 (b), results in a corresponding beam propagation ratio  $M_{4\sigma}^2$  of 1.8 and 6.4 for the fast- and slow-axis, respectively. When  $1/e^2$ -level method is applied to determine the beam diameters, beam propagation ratio  $M_{1/e^2}^2$  of 1.1 and 1.0 result in the fast- and slow-axis, respectively. The central lobe power content in the lateral beam waist of 81 % is determined.

Planar waveguide samples with a shorter QPM period are characterized with the DBR-TPL- $\Lambda$ -956. For this purpose the diode laser is biased with  $I_{RW} = 0.300$  A and  $I_{TP} = 9.0$  A, which leads to a maximum NIR pump power of  $P_{\text{pump}} = (4.1 \pm 0.2)$  W in front of the nonlinear crystal. The laser emits in a longitudinal single-mode at a central wavelength of 1062.7 nm, as can be seen in Fig. 5.14 (a).

The caustic presented in Fig. 5.14 (b) is based on second order moments method. A corresponding beam propagation ratio  $M_{4\sigma}^2$  of 1.7 and 6.0 for the fast- and slow-axis, respectively, can be determined. When  $1/e^2$  threshold beam diameters are considered, beam propagation ratio  $M_{1/e^2}^2$  of 1.2 and 1.1 results in the

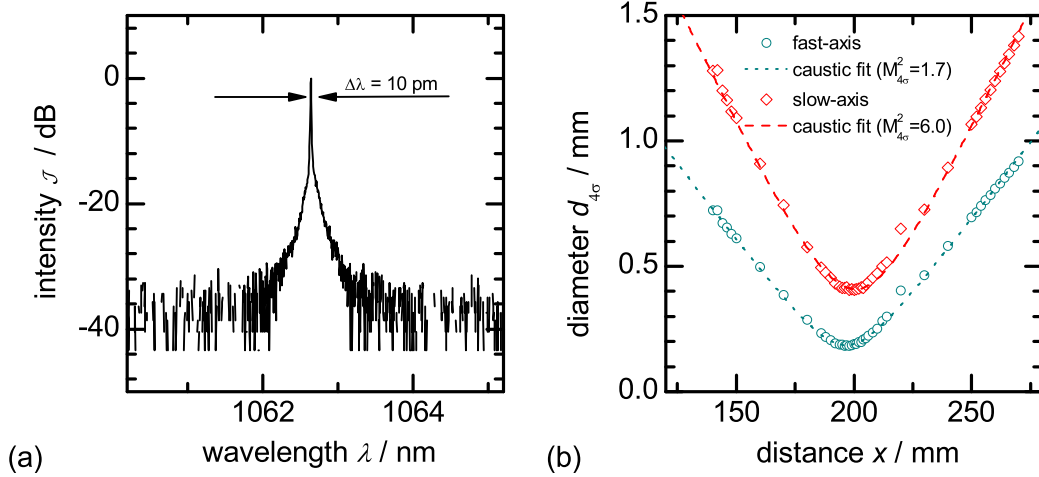


**Figure 5.14:** Spectrum (a) and caustic (b) of the DBR-TPL- $\Lambda$ -956 beam at  $T = 25.0^\circ\text{C}$ ,  $I_{\text{RW}} = 0.300\text{ A}$ ,  $I_{\text{TP}} = 9.0\text{ A}$

fast- and slow-axis, respectively. The central lobe power content in the lateral beam waist is determined to 83 %.

In advance to SHG experiments in planar waveguide samples, the intensity distribution of the focused NIR pump beam in front of the nonlinear crystal is investigated for each laser. Since both lasers possess almost identical beam properties, only the results of measurements and calculations for the diode laser DBR-TPL- $\Lambda$ -958 are presented below. The corresponding results of an intensity distribution measurement with a microscope objective (Appendix A.1) in the focal points of the cylindric lens L3 and the acylindric lens L4 is presented in Fig. 5.15 (a) on a linear and logarithmic scale. The vertical and lateral  $1/e^2$  threshold beam waist diameters of  $(5.5 \pm 1.1)$  and  $(38 \pm 4)\ \mu\text{m}$ , respectively, agree well with the diameters simulated with WINABCD. The measured distribution contains finite intensity values beyond the  $1/e^2$  beam diameter, especially in the slow-axis, as can be seen on the logarithmic scale. This is a typical feature of tapered diode lasers, which influences profoundly the lateral beam quality determined accordingly to second order moments method (Sect. 2.3.2, p. 11).

The vertical projection of the measured intensity distribution in the beam waist is presented in Fig. 5.15 (b) as a dotted curve. It agrees relatively well with the 1-dimensional waveguide lowest-order mode intensity profile (solid curve) simulated with FIMMWAVE, which leads to a coupling efficiency of 88 % determined through a calculation of the corresponding overlap integral (Eq. (3.6)). The calculated coupling efficiency is lower than in case of a Gaussian beam due to intensity lobes visible in the measured distribution above and below the main peak, which are connected with inferior vertical beam quality with  $M_{4\sigma}^2 = 1.8$  compared to  $M_{4\sigma}^2 = 1.1$  determined for the near-Gaussian beam.

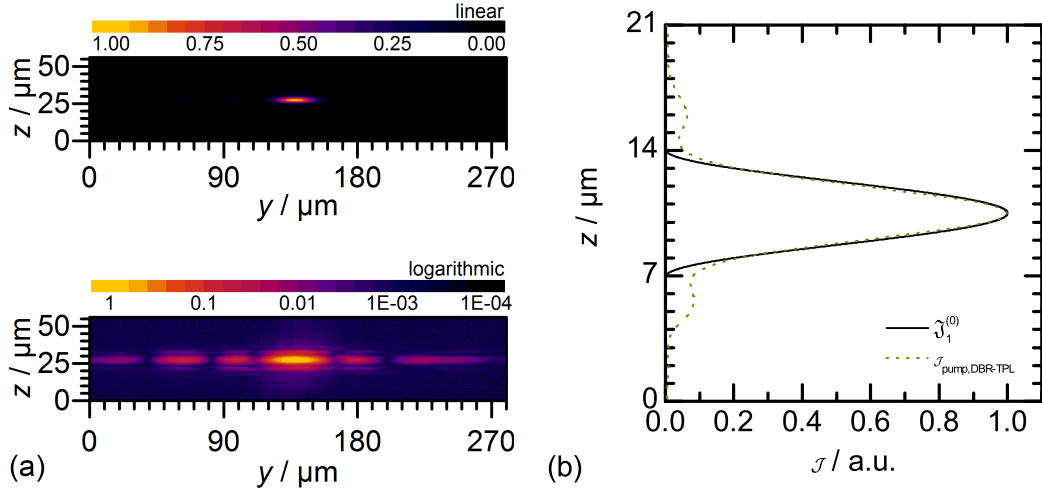


**Figure 5.15:** Measured 2-dimensional intensity distribution of the DBR-TPL- $\Lambda$ -958 beam in the beam waist in front of the nonlinear crystal on linear and logarithmic scale (a). Projection of the measured intensity distribution in the fast-axis  $\mathcal{J}_{\text{pump,DBR-TPL}}$  and the simulated waveguide lowest-order mode intensity distribution  $\mathcal{J}_1^{(0)}$  (b)

### 5.2.3 SHG process subject to pump beam parameters

The investigation of NIR beam parameter influence on the SHG process is conducted with the laser DBR-TPL- $\Lambda$ -958 and the planar waveguide sample L15-W500-WG1. This 500  $\mu\text{m}$ -wide waveguide has already been applied for frequency doubling of a near-Gaussian beam described in Sect. 5.1.3. The NIR pump power in front of the nonlinear crystal is set to a value  $P_{\text{pump}} = (0.67 \pm 0.02)$  W through the adjustment of HWP H1 in experimental setup, which is schematically presented in Fig. 5.10. This fundamental power value corresponds to a maximum power density  $\mathcal{J}_1$  inside of the planar waveguide of approx.  $0.3 \text{ MW}/\text{cm}^2$  for the optimum lateral focusing, and lies, therefore, in the intensity range, in which the SHG process is not affected by increased nonlinear absorption (compare Sect. 4.6). The lateral beam waist is located in the middle of the nonlinear crystal, which leads to a maximum conversion efficiency during SHG. The transmission through the planar waveguide for the DBR-TPL is determined analog to a corresponding measurement conducted with a near-Gaussian beam (Sect. 5.1.3), resulting in a value  $\tau_{\text{DBR-TPL}} = (83 \pm 5)$  % at an extraordinary polarization. The deviation from the coupling efficiency calculated in Sect. 5.2.2 (p. 72) originates most likely from the propagation loss in the planar waveguide structure, as has already been stated in Sect. 5.1.3.

#### Beam quality

The measurement of the SH power at the crystal mount temperature  $T_{\text{mount}} = 44.0^\circ\text{C}$  allows to determine the maximum normalized SHG conversion efficiency for a DBR-TPL pump beam, calculated according to Eq. (3.62). The resulting value of  $\bar{\eta}_{\text{SHG}} = (18 \pm 3)$  %  $\text{W}^{-1}$  corresponds to an effective nonlinear coefficient

of  $d_{\text{eff,QPM}}^{\text{DBR-TPL}} = 11.3 \text{ pm/V}$ , which amounts to 84 % of the waveguide SHG device specific coefficient determined with a near-Gaussian beam (Sect. 5.1.3). This discrepancy originates from an inferior lateral beam quality of the DBR-TPL beam compared to a near-Gaussian beam (compare Figs. 5.5 (b) and 5.13 (b)). Hence, the ratio of 84 % correlates well with the central lobe power content in the lateral beam waist distribution of the DBR-TPL beam, which is calculated to approx. 81 %. Please note, that for a Gaussian beam this power content is theoretically equal to 100 %. For this reason, if the central lobe power instead of the entire NIR pump power is inserted in Eq. (3.62), a normalized SHG conversion efficiency of  $\bar{\eta}_{\text{SHG}} = (27 \pm 5) \% \text{ W}^{-1}$  results, which agrees well with the value determined experimentally for a near-Gaussian pump beam in Sect. 5.1.3.

### Crystal mount temperature

The measured normalized SHG conversion efficiency as a function of the crystal mount temperature for a DBR-TPL is presented in Fig. 5.16 as open circles on linear (a) and logarithmic (b) scale. The measured distribution shows a

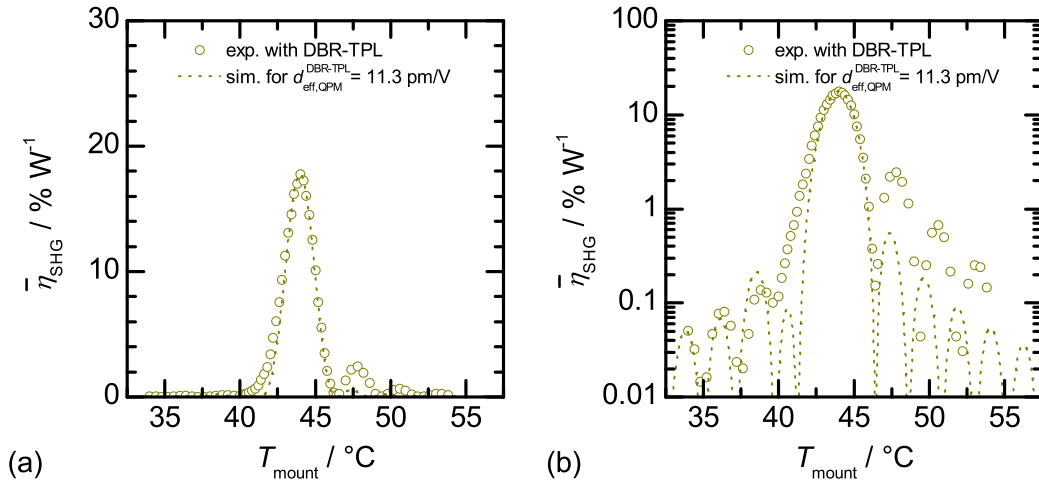


**Figure 5.16:** Simulated and measured normalized SHG conversion efficiency vs. the crystal mount temperature on linear (a) and logarithmic (b) scale

relatively good agreement with results of simulation according to Eq. (3.47) for  $d_{\text{eff,QPM}}^{\text{DBR-TPL}} = 11.3 \text{ pm/V}$  (dotted curve). Additionally to increased side-peaks at higher temperatures relative to main peak, which have already been observed in Fig. 5.7, a slower decrease from the maximum value with decreasing crystal mount temperature can be noticed in case of frequency doubling of DBR-TPL beam (Fig. 5.16 (b)). Consequently, the corresponding experimentally determined acceptance bandwidth of  $\Delta T_{\text{FWHM}} = 2.4 \text{ K}$  is larger than its counterpart during frequency doubling of a near-Gaussian beam (Fig. 5.16). It is assumed, that this phenomenon originates from different intensity distribution in the far field of a DBR-TPL beam, which is similar to top-hat rather than

Gaussian distribution (compare Fig. 2.8 and 2.9). The intensity parts at large divergence angles experience QPM at a lower temperature than the paraxial rays, which leads to a higher SH power and, consequently, to a higher normalized SHG conversion efficiency in this temperature region. In addition, according to the simulation the crystal mount temperature needs to be set to an optimum value with an accuracy of  $\pm 0.3$  K in order to ensure a normalized SHG conversion efficiency higher than 95 % of the maximum reachable value.

### Focusing strength

In order to determine the influence of the lateral focusing of the DBR-TPL beam on the normalized SHG conversion efficiency in a planar waveguide experimentally, the cylindric lens L3 in optical setup (Fig. 5.10) is exchanged with lenses characterized by different focal lengths. The lateral beam waist is placed in the middle of the nonlinear crystal for every successive lens. In Fig. 5.17 the resulting normalized SHG conversion efficiency  $\bar{\eta}_{\text{SHG}}$  as a function of the  $1/e^2$  lateral beam waist diameter is presented as open circles. The measured values

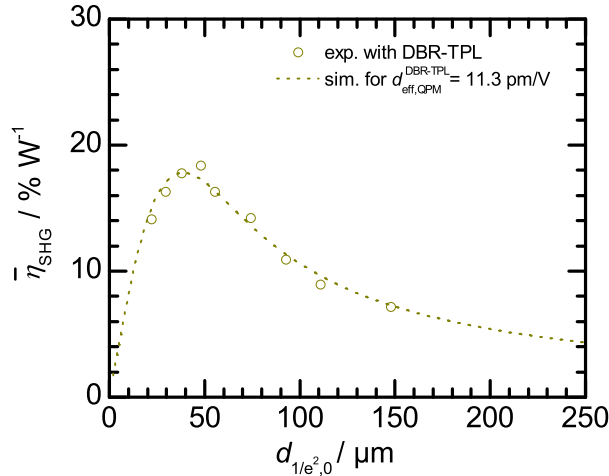


**Figure 5.17:** Simulated and measured normalized SHG conversion efficiency vs. the beam waist diameter

are consistent with the theoretical distribution (dotted curve), calculated according to Eq. (3.47) for an effective nonlinear coefficient  $d_{\text{eff,QPM}}^{\text{DBR-TPL}} = 11.3$  pm/V. Although, in case of a DBR-TPL pump beam the absolute normalized SHG conversion efficiency is lower than for a near-Gaussian beam, the relative change for a variation of the  $1/e^2$  beam waist diameter is still conform to Fluck's theory (Sect. 3.2.4). This good agreement is however conditional upon the DBR-TPL beam characteristics in the slow-axis with a distinctive central lobe in the beam waist distribution characterized by a superior beam quality than the entire beam.

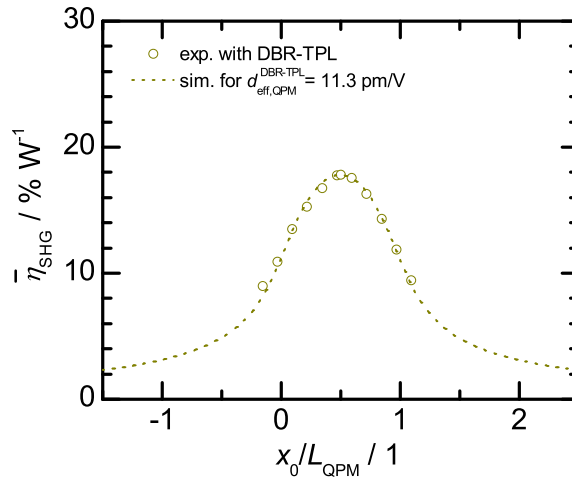
For a beam waist diameter of  $d_{1/e^2,0} = (38 \pm 4)$   $\mu\text{m}$ , closest to the theoretical optimum, a normalized SHG conversion efficiency of  $\bar{\eta}_{\text{SHG}} = (18 \pm 3)$   $\% \text{W}^{-1}$  is reached. In addition, according to the simulation the lateral beam waist diameter needs to be set to a value of 39  $\mu\text{m}$  with an accuracy of  ${}_{-9.7}^{+13}$   $\mu\text{m}$  in order to ensure a normalized SHG conversion efficiency higher than 95 % of the maximum reachable value.

### Focus position

Kleinman and Miller [63] investigated experimentally the influence of the beam waist position along the propagation direction on the SHG conversion efficiency in a bulk crystal. In their experiment they confirmed the theory of Boyd and Kleinman [21], which stated, that the maximum conversion efficiency for an optimally focused Gaussian beam is reached, when the beam waist is placed in the middle of the nonlinear crystal.

Here, an analog experiment for frequency doubling of a DBR-TPL beam in a planar waveguide structure is carried out. The results for an optimum lateral

**Figure 5.18:** Simulated and measured normalized SHG conversion efficiency vs. the relative beam waist position



beam waist diameter  $d_{1/e^2,0} = (38 \pm 4) \mu\text{m}$  are presented in Fig. 5.18. The experimentally determined values (open circles) agree well with the results of simulation according to Eq. (3.47) for  $d_{\text{eff,QPM}}^{\text{DBR-TPL}} = 11.3 \text{ pm/V}$  (dotted curve) and therefore confirm the theory of Fluck (Sect. 3.2.4). The normalized SHG conversion efficiency as a function of the effective lateral beam waist position with regard to the QPM region length ( $x_0/L_{\text{QPM}}$ ) is characterized by a symmetric distribution. The maximum value is reached when the lateral beam waist  $x_0$  is placed in the middle of the QPM region length ( $x_0/L_{\text{QPM}} = 0.5$ ). Dislocation of the lateral beam waist from the optimum position leads to a decrease in conversion efficiency. In order to assure a normalized SHG conversion efficiency greater than 95 % of the maximum value the position of the lateral beam waist needs to be set in the middle of the nonlinear crystal with a relative accuracy of  $\pm 0.175$ , which for a QPM region length  $L_{\text{QPM}} = 12 \text{ mm}$  results in a required absolute accuracy of  $\pm 2.1 \text{ mm}$ . When the lateral beam waist is placed on the ends of the periodically poled region ( $x_0/L_{\text{QPM}} = 0.0$  or  $1.0$ ), the normalized conversion efficiency reaches approx. 60 % of its maximum value.

### Angle of incidence in the fast-axis

NIR laser beam characteristics in the vertical direction also influence the SHG conversion efficiency in the planar waveguide structure. In general, both planar and ridge waveguide structures in nonlinear crystals support a large

number of transversal modes. Due to modal dispersion, the QPM condition in waveguide SHG devices can be fulfilled only for one waveguide mode pair at a time. Nonlinear interactions between fundamental and SH waveguide lowest-order modes are being preferred, since they are most efficient due to large effective mode overlap. Hence, the content of NIR pump power coupled into the waveguide lowest-order mode needs to be optimized in order to maximize the SHG conversion efficiency (compare Sect. 3.2.4). It is self-evident that for efficient coupling the beam waist diameter needs to be adjusted. However, the vertical incidence angle adjustment is also of great importance for the coupling efficiency into the lowest-order mode of a planar waveguide structure, as will be shown below.

In Fig. 5.19 the transmission  $\tau$  through the planar waveguide subject to vertical incidence angle  $\theta_i$  is presented. The measured overall transmission during SHG process  $\tau^{\text{SHG}}$  (closed circles) remains constant over the variation of the angle and is consistent with the value of  $\tau_{\text{DBR-TPL}} = (83 \pm 5) \%$  determined above for perpendicular crystal facet irradiation. Additionally to experimental results, calculated transmission distributions obtained through simulations with FIMMWAVE for a Gaussian beam with an optimum beam diameter in the vertical beam waist are presented in the graph. The transmission of light

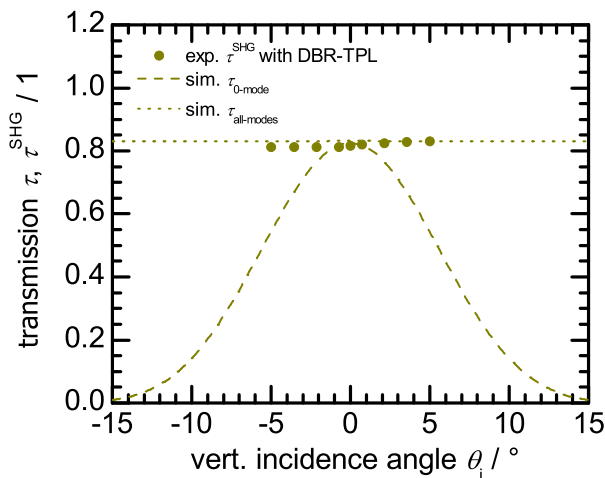


**Figure 5.19:** Simulated and measured transmission vs. vertical incidence angle

coupled into all vertical modes guided in the waveguide structure  $\tau_{\text{all-modes}}$  (dotted curve) is consistent with the experiment and remains constant over the variation of the vertical incidence angle. In contrast, the simulated transmission of the light coupled into the waveguide lowest-order mode  $\tau_{0\text{-mode}}$  (dashed curve) decreases with increasing incidence angle  $\theta_i$  due to decreasing coupling efficiency at the waveguide front facet. Hence, with increasing incidence angle the power coupled into the waveguide structure is distributed among the different vertical modes but its sum remains constant. Please note, that the vertical beam waist diameter, optimized for maximum coupling efficiency into the given waveguide structure, is not being altered deliberately over the investigated vertical incidence angle range both in the simulation and in the experiment.

The fact, that the power content coupled into the lowest-order mode of the

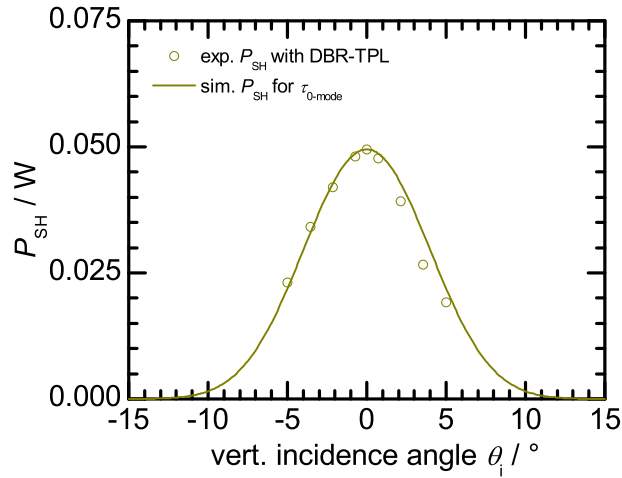


**Figure 5.20:** Measured and calculated SH power vs. vertical incidence angle

fundamental wave decreases with increasing vertical incidence angle, affects the SHG process, as can be observed in Fig. 5.20. Here, the measured (open circles) and simulated (solid line) SH power dependence on the vertical incidence angle is presented. The experimental data shows a very good qualitative and quantitative agreement with the results of calculations conducted according to Eq. (3.61) and incorporating the transmission distribution from Fig. 5.19 for the waveguide lowest-order mode (dashed curve). Consequently, as can be observed in Fig. 5.20, the maximum SH power is reached at an incidence angle  $\theta_i = 0^\circ$  and it decreases with increasing incidence angle, although the overall measured transmission through the waveguide structure remains constant (Fig. 5.19, filled circles).

As a result of this investigation, a tolerance for the vertical incidence angle can be defined. In order to assure a normalized SHG conversion efficiency greater than 95 % of the maximum value, the vertical incidence angle needs to be set to an optimum value with an accuracy of  $\pm 1.2^\circ$ .

#### 5.2.4 High-power generation

Subsequently to investigations of SHG process in a planar waveguide as a function of NIR beam parameters, frequency doubling of DBR-TPL radiation at high-power is studied. The experiments are conducted at optimum NIR laser beam parameters determined in Sect. 5.2.3 in planar waveguide samples described in detail in Sect. 3.3. Depending on the QPM grating period length of the nonlinear crystal either the laser DBR-TPL- $\Lambda$ -958 or DBR-TPL- $\Lambda$ -956 is applied.

The results for 13 mm-long planar waveguide samples are presented in Figs. 5.21 and 5.22. The difference in the maximum NIR pump power for each sample results from an adjusted operating current of the applied laser DBR-TPL- $\Lambda$ -956, which was in this case necessary in order to ensure a stable longitudinal single-mode emission. Both 13 mm-long waveguides are characterized by a transmission  $\tau_{\text{DBR-TPL}}$  in the range of 70 %, which is lower compared to the

15 mm-long samples due to smaller waveguide width and inferior facet AR coating quality. A measurement of the SH power dependency on the crystal mount temperature for both samples confirms a good structural homogeneity.

The generated SH power as a function of the NIR pump power in front of the crystal is presented in Fig. 5.21. The experimental results for both samples

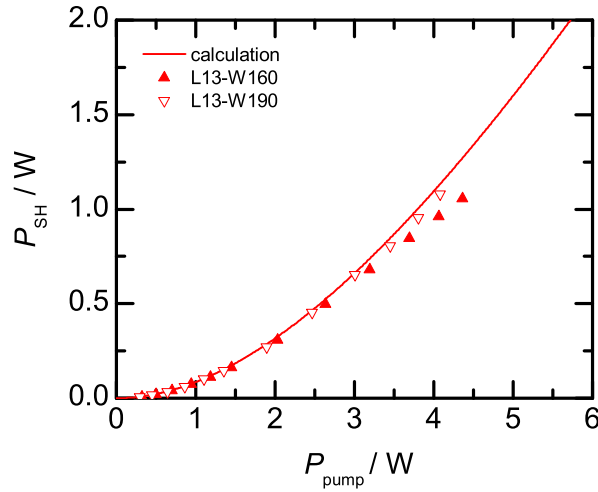


**Figure 5.21:** Calculated and measured SH power vs. NIR pump power for 13 mm-long samples

(open and filled triangles) agree relatively well with calculations (solid curve) according to Eq. (3.61) for  $\tau_{\text{DBR-TPL}} = 72\%$  and  $\bar{\eta}_{\text{SHG}} = 18\% \text{ W}^{-1}$  in the entire investigated range. Only in case of the sample L13-W160, the experimental values depart slightly from the theoretical curve above an NIR pump power of approx. 3 W. With the planar waveguide L13-W190 a maximum SH power of  $P_{\text{SH}} = (1.07 \pm 0.03) \text{ W}$  with an opto-optical and electro-optical conversion efficiency of  $\eta_{\text{opt.}} = (27 \pm 1)\%$  and  $\eta_{\text{el.}} = (8.5 \pm 0.3)\%$  is reached, respectively. Due to a lower transmission  $\tau$  the opto-optical conversion efficiency (Fig. 5.22) increases at a lower rate with increasing NIR pump power compared to the 15 mm-long samples (Fig. 5.24). Nevertheless, a relatively good agreement for both waveguides between measured (open and filled triangles) and calculated (solid curve) values can be observed in the entire investigated range. The minor

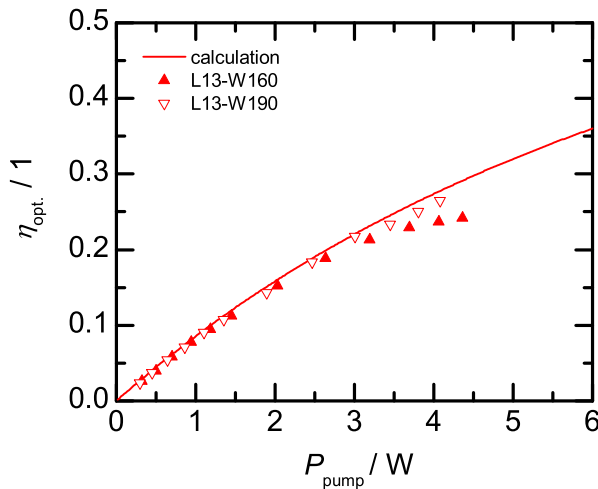


**Figure 5.22:** Calculated and measured opto-optical conversion efficiency vs. NIR pump power for 13 mm-long samples

difference between measured and calculated SH power for the sample L13-W160 observed in Fig. 5.21 leads to a similar deviation in the distribution of the opto-optical conversion efficiency in Fig. 5.22. The overall transmission through the waveguides during the SHG process as well as the optimum crystal mount temperature are presented and discussed below.

The results accomplished with 15 mm-long samples are presented in Figs. 5.23 and 5.24. All waveguides are characterized by a transmission  $\tau$  greater than 80 % which is in good agreement with the transmission value determined above in Sect. 5.2.3 for the sample L15-W500-WG1. In addition, a measurement of the SH power dependency on the crystal mount temperature for each sample confirms a good structural homogeneity.

The generated SH power and the corresponding opto-optical conversion efficiency as a function of the NIR pump power in front of the crystal is presented in Fig. 5.23 and 5.24, respectively. At low NIR pump power the experimental

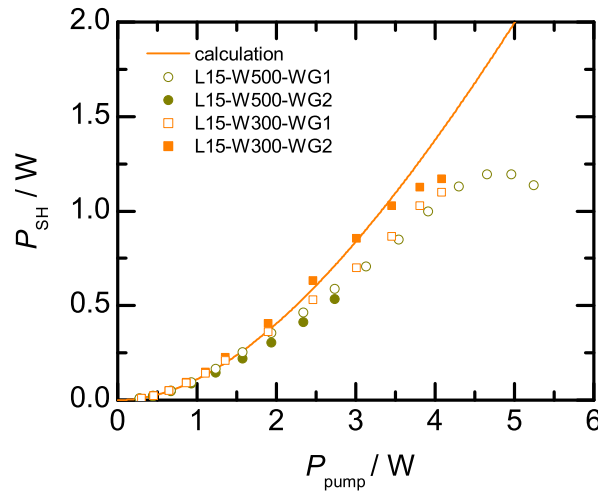


**Figure 5.23:** Calculated and measured SH power vs. NIR pump power for 15 mm-long samples

results (circles for 500  $\mu\text{m}$  and squares for 300  $\mu\text{m}$ -wide waveguides) agree well with calculations (solid curve) according to Eq. (3.61) for  $\tau_{\text{DBR-TPL}} = 83 \%$  and  $\bar{\eta}_{\text{SHG}} = 18 \%$   $\text{W}^{-1}$ . With increasing NIR pump power the experimental data departs from the theoretical distribution. For three samples this deviation occurs between 1 and 2 W, for the fourth sample not before an NIR pump power of approx. 3 W is reached.

With the less susceptible sample, L15-W300-WG2, a maximum SH power of  $P_{\text{SH}} = (1.17 \pm 0.05) \text{ W}$  at an opto-optical and electro-optical conversion efficiency of  $\eta_{\text{opt.}} = (29 \pm 2) \%$  and  $\eta_{\text{el.}} = (9.2 \pm 0.4) \%$  is reached, respectively. A maximum opto-optical conversion efficiency of  $\eta_{\text{opt.}} = (30 \pm 1) \%$  is reached at an NIR pump power of  $P_{\text{pump}} = (3.5 \pm 0.1) \text{ W}$ . Above this value the opto-optical conversion efficiency decreases with increasing NIR pump power, as can be observed in Fig. 5.24.

For the sample L15-W500-WG1 the NIR pump power in front of the nonlinear crystal is increased beyond the value of  $P_{\text{pump}} = (4.1 \pm 0.2) \text{ W}$ . In case of this sample, the maximum opto-optical conversion efficiency of  $\eta_{\text{opt.}} = (26 \pm 1) \%$  is

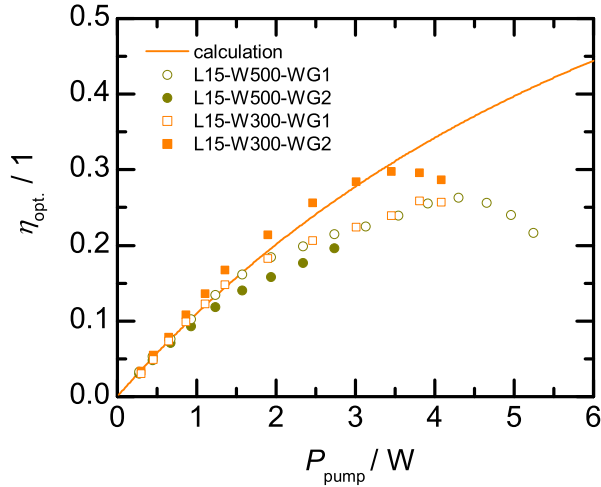


**Figure 5.24:** Calculated and measured opto-optical conversion efficiency vs. NIR pump power for 15 mm-long samples

reached at an NIR pump power of  $P_{\text{pump}} = (4.3 \pm 0.2)$  W, the maximum SH power of  $P_{\text{SH}} = (1.19 \pm 0.05)$  W at an NIR pump power of  $P_{\text{pump}} = (4.7 \pm 0.2)$  W. Above the latter pump power value, both opto-optical conversion efficiency and SH power decrease with increasing NIR pump power. The possible reasons for this limitation of the maximum SH power to approx. 1.2 W are discussed below.

The overall transmission through the planar waveguide structure during SHG process in dependence on the NIR pump power is presented for all investigated samples in Fig. 5.25. The 13 mm-long samples are characterized by a trans-

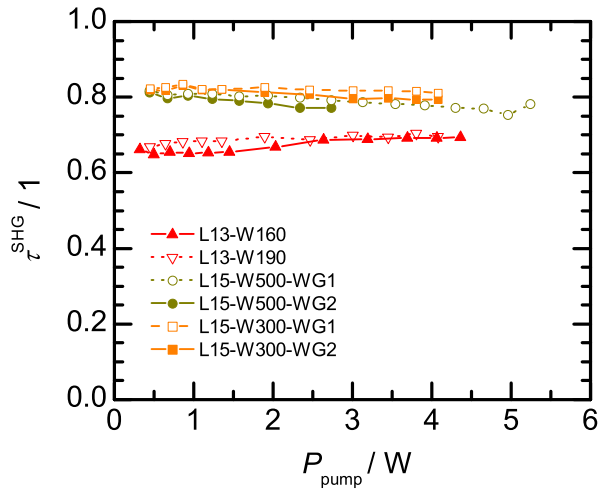


**Figure 5.25:** Measured overall transmission through the planar waveguide during SHG process vs. NIR pump power (lines are guides to the eye)

mission  $\tau^{\text{SHG}}$  in the range of 65 – 70 %. For these samples no decrease with increasing NIR pump power in the investigated power range is observed. The 15 mm-long samples are characterized by an overall transmission during SHG in the range of 80 – 83 % at a low NIR pump power in front of the nonlinear crystal. With increasing NIR pump power the transmission for the sample L15-W500-WG2 decreases strongly, which is most likely caused by an impurity on the waveguide front facet noticed before the experiments. This sample is investigated only to an NIR pump power value of  $P_{\text{pump}} = (2.7 \pm 0.1)$  W and

shows the poorest results (Figs. 5.23 and 5.24). For the samples L15-W500-WG1 and L15-W300-WG2 the overall transmission decreases slightly with increasing NIR pump power. The transmission of the sample L15-W300-WG2 remains unchanged in the investigated NIR pump power range.

For all samples the crystal mount temperature needs to be reduced with increasing NIR pump power in order to maximize the SH power, as can be observed in Fig. 5.26, where the relative mount temperature change is presented. In

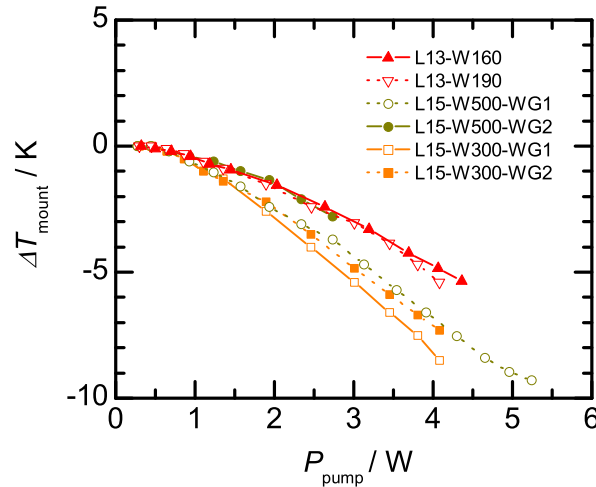


**Figure 5.26:** Relative change in the crystal mount temperature vs. NIR pump power (lines are guides to the eye)

case of the 13 mm-long crystal mount temperature needs to be decreased by approx. 5 K in the investigated NIR pump power range, which most likely originates from waveguide structure heating due to propagation loss and absorption. Similar behavior has already been observed in [107]. In the same power range the crystal mount temperature for 15 mm-long samples needs to be reduced by approx. 8 K. The greater change in the crystal mount temperature compared to 13 mm-long waveguides could be explained by higher transmission through the 15 mm-long samples, higher opto-optical conversion efficiency and, therefore, higher SH power. In addition, higher propagation loss is expected in longer waveguides, which however cannot be verified due to different waveguide width and AR coating quality.

Highest SH power and highest opto-optical and electro-optical conversion efficiency are achieved with 15 mm-long planar waveguides. Although, the best results are obtained with a 300  $\mu\text{m}$ -wide waveguide (L15-W300-WG2), the differences between 300 and 500  $\mu\text{m}$ -wide samples regarding the SHG process are believed to originate from statistical variation of devices quality. Wider waveguides, however, could provide greater tolerances for waveguide position adjustment in the slow-axis.

The normalized SHG conversion efficiency in 13 mm-long samples is less susceptible to high-power operation. However, these samples provide lower maximum SH power and lower opto-optical conversion efficiency due to lower transmission through the waveguide structure. Investigation of the most susceptible sample, L13-W190, at higher NIR pump powers is not possible, since it was damaged due to misalignment of the waveguide position during the experiment. As

a consequence the crystal facet was damaged to an extent of 50 % and the waveguide structure was impaired over the whole crystal length including the rear facet. This critical incident illustrates clearly, that during high-power SHG no change in the waveguide position can be tolerated. In addition, the adjustment of the waveguide structure position needs to be undertaken at low NIR pump power before the power level can be increased.

Theoretically, in the investigated planar waveguide samples an SH power of 2.6 W and an opto-optical conversion efficiency of  $\eta_{\text{opt.}} = 44\%$  could be achieved at the available maximum NIR pump power. In the experiment, however, both the SH power and the opto-optical conversion efficiency are saturated. Since the maximum SH intensity  $\mathcal{J}_2$  present in the planar waveguide is estimated to be less than  $0.3 \text{ W/cm}^2$  and no distinct transmission reduction with increasing power can be observed in Fig. 5.25, the measured saturation is most likely not caused directly by increasing nonlinear absorption in the waveguide core composed of the periodically poled nonlinear crystal material. Instead, the results presented indicate that the epoxy applied as a cladding layer in the waveguide structure could be the reason for the saturation of the SH power observed in the experiment. Due to relatively high fundamental wave power density  $\mathcal{J}_1$  in the range of  $2.0 \text{ MW/cm}^2$  estimated for the lateral beam waist range, the properties of the epoxy in this region, in particular the refractive index, could change, as a result of absorption and consequent heating, to such an extent, that the overall SHG process becomes less efficient due to locally distorted quasi phase-matching. This assumption appears plausible given that a destructive effect during epoxy illumination with the high-power laser beam could be observed, as described above. In order to reach higher SH powers, further improvements of the waveguide structure including cladding layers less prone to high-power operation are needed. With optimized SHG devices, SH power level in the range of 3 W could be realized by applying already available DBR-TPLs. Nevertheless, results on SHG in planar waveguides accomplished in this chapter with diode lasers are already comparable with the results reported in the literature for frequency doubling of solid state lasers in similar structures [107].

### 5.2.5 SH beam characteristics

The generated SH beam is characterized with regard to its spectral and spatial characteristics. The results obtained during frequency doubling of the diode laser DBR-TPL- $\Lambda$ -958 in the planar waveguide sample L15-W500-WG1 are presented in Fig. 5.27. The measurements are conducted at an SH power  $P_{\text{SH}} = (0.52 \pm 0.02) \text{ W}$  reached at optimum NIR laser beam parameters determined in Sect. 5.2.3.

The SH spectrum measured with ELIAS spectrometer (Appendix A.1) in double pass is presented in Fig. 5.27 (a). The determined spectral linewidth of 0.3 pm (FWHM) as well as a noise level of  $-40 \text{ dB}$  are limited by the spectral resolution and the maximum signal-to-noise ratio of the applied spectrometer, respectively.

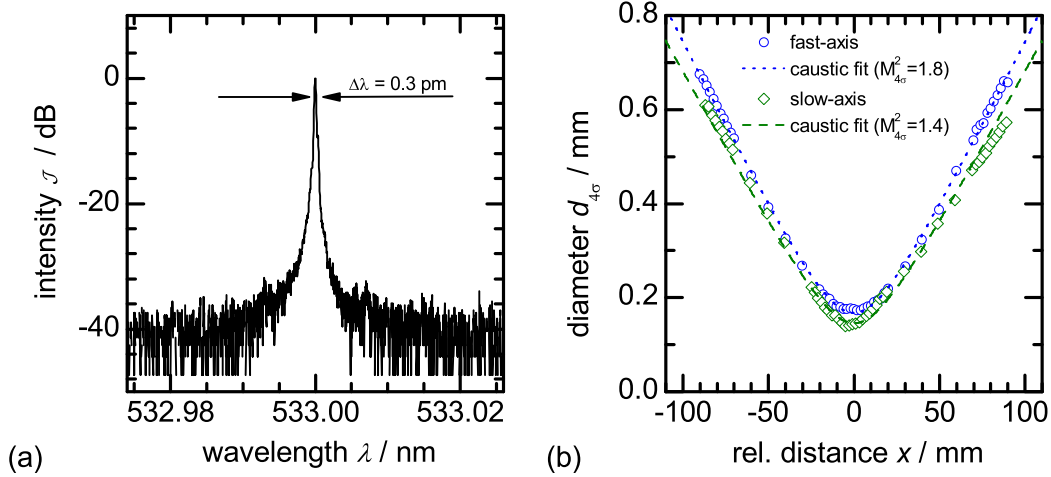


**Figure 5.27:** Spectrum (a) and caustic (b) of the SH beam generated by a DBR-TPL beam

Results of a SH caustic measurement according to second order moments method are presented in Fig. 5.27 (b). A beam propagation ratio  $M_{4\sigma}^2$  of 1.4 determined for the slow-axis demonstrates an improvement compared to the lateral beam propagation ratio  $M_{4\sigma}^2$  of the DBR-TPL beam, which is discussed above in Sect. 5.2.2. Similar behavior has already been observed during frequency doubling of a DBR-TPL beam in a bulk crystal [19]. The improvement results most likely from the fact, that the side-lobes present in DBR-TPL beam waist reach lower intensity levels than the central lobe and are, therefore, less efficiently converted. In addition, for  $1/e^2$ -level diameters a beam propagation ratio  $M_{1/e^2}^2$  of 1.0 is determined in the slow-axis with a central lobe power content in the beam waist of 98 %.

The SH beam quality in the fast-axis is predetermined by the planar waveguide structure, as has already been observed in Secs. 4.3 and 5.1.4. However, the  $M_{4\sigma}^2$  of 1.8 resulting from the caustic presented in Fig. 5.27 is larger compared to the value determined for SH radiation generated from a near-Gaussian NIR beam (Sect. 5.1.4). This difference results from finite intensity values outside of the beam diameter, which most likely originate from scattering inside of the waveguide structure. Nonetheless, an  $M_{1/e^2}^2$  of 1.0 is determined for the SH beam with a central lobe power content in the beam waist of 98 %.

### 5.3 Summary

In this chapter, efficient high-power single-pass frequency doubling of a DBR-TPL beam in a ppMgO:LN planar waveguide was investigated theoretically and experimentally.

Initial characterization of the planar waveguide structure with a near-Gaussian beam provided reference values for subsequent experiments with a DBR-TPL. This way, the effective nonlinear coefficient of  $d_{\text{eff,QPM}} = 13.5 \text{ pm/V}$ , characteris-

tic for the used quasi phase-matched planar waveguides, could be determined. In the experiments with a DBR-TPL as NIR pump source a transmission through the waveguide of  $\tau_{\text{DBR-TPL}} = (83 \pm 5) \%$  and a normalized SHG conversion efficiency of  $\bar{\eta}_{\text{SHG}} = (18 \pm 3) \% \text{ W}^{-1}$  were achieved. The latter value corresponded to an effective nonlinear coefficient of  $d_{\text{eff,QPM}}^{\text{DBR-TPL}} = 11.3 \text{ pm/V}$ , which amounted to 84 % of the device specific value determined with a near-Gaussian beam. This deviation correlated well with the central lobe power content in the lateral beam waist of 81 %, determined for the utilized DBR-TPL. Hence, this way a quantitative dependency between the beam quality parameter of the DBR-TPL and the corresponding normalized SHG conversion efficiency could be provided.

Prior to high-power experiments, a comprehensive experimental study of the normalized SHG conversion efficiency as a function of DBR-TPL beam parameters was carried out. A good agreement with theoretical predictions for the experimental parameter variation was observed. This way, optimum NIR pump beam parameters with corresponding tolerances were defined and could be applied in subsequent experiments.

During high-power operation, an SH power of  $P_{\text{SH}} = (1.17 \pm 0.05) \text{ W}$  at an opto-optical and electro-optical conversion efficiency of  $\eta_{\text{opt.}} = (29 \pm 2) \%$  and  $\eta_{\text{el.}} = (9.2 \pm 0.4) \%$  was reached, respectively. Although the maximum SH intensity  $\mathcal{J}_2$  present in the planar waveguide structures in this chapter does not exceed a value of approx.  $0.3 \text{ MW/cm}^2$  and no distinct increase of loss could be determined, a saturation of the SH power and of the opto-optical conversion efficiency was observed during the experiments. This limitation is, therefore, attributed to planar waveguide cladding material not suitable for high-power operation, which corresponds to a maximum fundamental wave intensity  $\mathcal{J}_1$  in the range of  $2.0 \text{ MW/cm}^2$ .

Results on SHG in planar waveguides accomplished in this chapter with diode lasers are comparable with the results reported in the literature for frequency doubling of solid state lasers in similar SHG devices [107]. Higher SH power is expected for an improved waveguide structure.



# Chapter 6

## Final conclusions and perspectives

### 6.1 Summary and conclusions

Single-pass frequency doubling of near-infrared diode lasers in quasi phase-matched nonlinear bulk crystals represents a straightforward approach to realize efficient and compact green emitting lasers with a high output power in CW operation and a nearly diffraction-limited beam quality [19, 20]. In this thesis, the application of waveguide structures, instead of bulk crystals, was investigated theoretically and experimentally in terms of the improvement of conversion efficiency. In particular, a complemented study of second-harmonic generation (SHG) in ridge and planar waveguides provided information concerning the benefits and limitations for both geometries with respect to maximum conversion efficiency and maximum accessible power in the green spectral region.

The properties of a near-infrared diode laser beam influence greatly the SHG process in waveguide structures (Sect. 2.2). For efficient frequency doubling single emitters characterized by a narrow-band emission matching the acceptance bandwidth of the nonlinear crystal are required. In addition, a nearly diffraction-limited beam is desired in order to ensure high coupling efficiency and, in case of planar waveguides, high normalized SHG conversion efficiency. The diode laser output power has to be chosen properly according to the waveguide geometry in order to fully exploit the potential of a given SHG device. For the purpose of this thesis, distributed Bragg reflector diode lasers incorporating an efficient epitaxial structure emitting around 1064 nm were applied. Depending on the desired output power range, a laser either with a ridge waveguide or a tapered resonator concept was selected (Sect. 2.3).

Waveguide SHG devices consisting of periodically poled MgO-doped lithium niobate were chosen for the nonlinear frequency conversion process due to multiple advantages of this dielectric crystal (Sect. 3.3). A thorough theoretical electromagnetic analysis of ridge and planar waveguide structures was carried out prior to experiments in order to provide parameters required for the optical system design and for the simulation of the SHG process. Optical lenses in each setup were selected based on optical simulations in order to provide a maximum coupling efficiency into the lowest-order mode of the waveguide and, in case of planar waveguides, to ensure a maximum normalized SHG conversion

efficiency.

Application of waveguide structures for frequency doubling of near-infrared diode lasers in this thesis resulted in a distinct improvement of the opto-optical conversion efficiency. An increase from approx. 20 % in a bulk crystal [9, 10] to almost 30 % in a planar waveguide and approx. 40 % in a ridge waveguide was achieved. However, unlike in a bulk crystal, the maximum generated power was limited in both waveguide geometries due to reasons described below. Nonetheless, an electro-optical conversion efficiency of more than 9 % was reached with both waveguide geometries. This result represents almost a two times higher value compared to bulk crystals [9]. The generated laser radiation in the green spectral range is characterized by a single-frequency spectrum and nearly diffraction-limited beam quality and is therefore well suited for applications in the fields of bio-medicine, bio-technology and spectroscopy.

In the ridge waveguide structure a maximum generated second-harmonic (SH) power of approx. 0.4 W was reached. With increasing NIR pump power a gradual saturation of the SH power together with an increase in the propagation loss could be observed experimentally. Above an SH wave intensity value of approx.  $1.7 \text{ MW/cm}^2$  a deviation from the theoretically expected  $\tanh^2$  distribution and above a value of  $3.1 \text{ MW/cm}^2$  a saturation of the SH power occurred. A numerical simulation of the nonlinear process based on a tailored theoretical model (Sect. 4.4), which incorporated a geometrical inhomogeneity, as well as increased linear and nonlinear absorption values and subsequent heat generation, matched exactly the experimental results (Sect. 4.6). As a result, for higher SH output power, the effective cross-section between the fundamental and the SH wave needed to be enlarged in order to reduce the power density, which was achieved by utilizing planar waveguide structures.

Prior to high-power experiments (Sect. 5.2.4), a comprehensive experimental study of the normalized SHG conversion efficiency in planar waveguides as a function of spatial diode laser beam parameters was carried out (Sect. 5.2.3). In this way, optimum values with corresponding tolerances were defined and could be applied in subsequent experiments. In addition, a consistent quantitative explanation of the lower normalized SHG conversion efficiency due to inferior diode laser beam quality compared to a Gaussian beam (Sect. 5.1) could be provided. The maximum generated SH power in planar waveguide structures of approx. 1.2 W was limited due to its gradual saturation with increasing NIR pump power. However, unlike in case of the ridge waveguide, no distinct increase of loss in the investigated power range could be determined. In addition, the maximum SH wave power density was determined to a value of approx.  $0.3 \text{ MW/cm}^2$ , which is an order of magnitude lower compared to SH wave intensities reached in the ridge waveguide. Therefore, the experimentally observed power limitation is attributed to thermally induced quasi phase-matching distortion, caused by waveguide cladding material not suitable for high power operation. Higher maximum output power is expected for improved planar waveguide structures.

In conclusion, the highest until now reported output power during frequency

doubling of near-infrared diode lasers in ridge and planar waveguides was reached in this thesis. The opto-optical conversion efficiency of the nonlinear interaction was improved considerably as compared to bulk crystals. Although the maximum output power was limited for both geometries, its further improvement in planar waveguides is expected for structures less prone to high-power operation. Results achieved with diode lasers in this work are comparable with the state-of-the-art on SHG in waveguide structures with solid state and fiber lasers reported in the literature [106, 107].

## 6.2 Future directions

Based on the findings of this thesis, several improvements and enhancements of the introduced concept are by all means recommendable. In particular, additional improvements of the planar waveguide structures are advisable, as this geometry is particularly suitable to further increase both the conversion efficiency and the maximum SH power. First and foremost, waveguide cladding layers less prone to high-power operation are required for this purpose, as was already mentioned in the previous section of this chapter. In addition, waveguides with longer periodically poled regions could be applied in order to increase the conversion efficiency. This, however, would occur at a cost of a narrower acceptance bandwidth, which has to be taken into consideration. Furthermore, near-infrared diode lasers with improved beam quality would also contribute to the enhancement of the conversion efficiency.

Alternatively, single emitters operated in pulsed regime could also be applied for SHG. Given the broad spectral emission of pulsed diode lasers [187], waveguide structures are in this case better suited for frequency doubling than bulk crystals, since they provide considerably higher normalized SHG conversion efficiency at the same acceptance bandwidth. In this context, the application of passively mode-locked diode lasers with integrated gratings for frequency conversion should be investigated systematically in terms of improvement of the conversion efficiency, as this concept is particularly interesting due to its simplicity [188]. In addition, frequency doubling of specially tailored pulses, required, for example, for time-resolved fluorescence spectroscopy [189], could also be conducted in waveguide SHG devices.

The results achieved in this work are already suitable for numerous applications. Therefore, in the next step a miniaturization of the experimental setup, similarly to the concept involving bulk crystals [19, 20], could be performed. For SHG micro-modules comprising a ridge or a planar waveguide, a wall-plug efficiency in the range of 10 % is expected, based on the results accomplished with the laboratory setup. However, this approach requires very accurate positioning and mounting of the optical elements, preferably during laser operation, in order to ensure efficient coupling and conversion. Therefore, the mounting procedure needs to be optimized, especially for high-power operation, in order to provide desired accuracy and to prevent misalignment, which could lead to a damage of the waveguide SHG device.

Furthermore, utilization of diode laser frequency doubling in waveguide structures to reach other wavelengths is also possible. In this context, the yellow spectral region is of particular interest for bio-medical and bio-technical applications, especially since no direct diode lasers are yet commercially available in this spectral range. The fabrication of suitable quasi phase-matched waveguide structures does not appear to be problematic [11, 12], whereas the availability of suitable diode lasers emitting between 1100 – 1200 nm is still limited. Until now, single-frequency edge-emitters operating in this spectral range and characterized by an output power below 100 mW were reported [190]. Therefore, the development of more powerful diode lasers suitable for frequency doubling represents the main challenge in this approach.

The findings of the present work have shown clearly, that frequency doubling of near-infrared diode lasers in quasi phase-matched waveguide structures has the potential to contribute emphatically to future development of efficient visible laser sources and their day-to-day applications.

# Appendix

## A.1 Equipment used for measurements

### Power measurement

Power measurements were conducted with equipment from Gentec Electro-Optics. Different thermopile detectors were applied depending on the investigated power range: for power level below 1 W power detectors XLP12 were used, for higher powers the power detector UP19K was applied. All detectors are certified with a measurement uncertainty of  $(2.5 \% \times \text{measured power})$ . The monitoring devices Solo 2 and Uno, which were used to read out the power values, increase the measurement uncertainty further by a value of  $(0.5 \% \times \text{measurement range})$ .

### Spectrum measurement

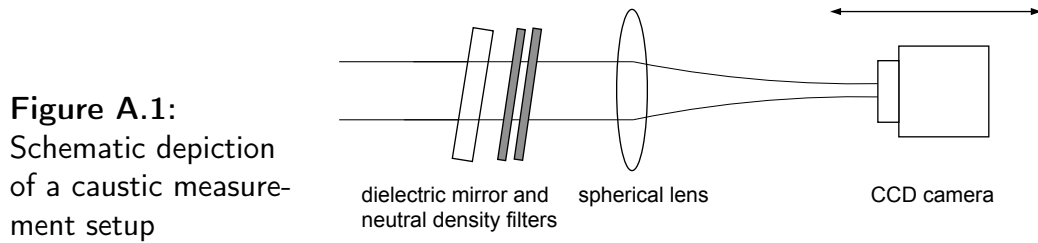
Emission spectra in the near-infrared range were recorded with a Double Echelle Monochromator (DEMON) from Lasertechnik Berlin or alternatively with an optical spectrum analyzer (OSA) Q8384 from Advantest. The former device consists of a high-resolution Echelle spectrometer in sequence with a prism monochromator and is characterized by a signal-to-noise ratio of approx. 40 dB, a resolution of approx. 10 pm (FWHM) at 1064 nm and an absolute central wavelength measurement uncertainty of approx. 150 pm. The latter device consists of a diffraction grating monochromator with a dynamic range of 60 dB and a resolution of approx. 10 pm (FWHM) around the wavelength of 1064 nm.

The laser radiation in the green spectral region was investigated with Emission Line Analyzing Spectrometer (ELIAS) III from Lasertechnik Berlin. This spectrometer consists of an Echelle grating, which can be used in a single, double or quad pass. In this thesis the double pass configuration was used, which provides a dynamic range of approx. 40 dB and a high resolution of approx. 0.2 pm (FWHM).

### Beam quality measurement

Beam quality of near-infrared and green laser beams was determined through a caustic measurement. For this purpose, each investigated beam was firstly attenuated with a dielectric mirror and a set of neutral density filters and secondly focused with a spherical lens ( $f = 200$  mm for near-infrared beams, custom

focal lengths for green beams) to generate a beam caustic with a distinct beam waist, as presented in Fig. A.1. Subsequently, 2-dimensional beam intensity



distributions along the propagation direction  $x$  were recorded with a camera. In this setup a Scorpion SCOR-20SOM camera from Point Grey Research contains a monochromatic CCD chip with a resolution of  $1200 \times 1600$  pixels, a pixel size of  $4.4 \mu\text{m}$  and a maximum signal-to-noise ratio of approx.  $4000 : 1$  was applied. The exposure time of the camera remained unchanged at  $30 \text{ ms}$  throughout the measurement and the laser beam intensity was adjusted to prevent camera chip saturation and provide large signal-to-noise ratio by exchanging the neutral density filters. Each recorded intensity distribution with subtracted background was averaged over 12 frames.

In the first step, through projections along the principal axes of the simple astigmatic beam, 1-dimensional intensity profiles are generated from the recorded 2-dimensional intensity distribution. A beam caustic in each of these directions represents the distribution of the corresponding beam diameters along the propagation direction. In this thesis, the  $1/e^2$ -level method and the second order moments method ( $4\sigma$ ) were applied to determine the beam diameters. In the former, the beam diameter is defined as the distance between two points characterized by an  $1/e^2$  intensity level relative to the maximum value. In the latter, which is approved by ISO norm 11146-1 [191], the beam diameter is defined as four times the standard deviation of the power density distribution under investigation.

In the next step, by means of fitting of a hyperbolic function to the measured data, determined either according to the  $1/e^2$ -level method or the second order moments method, the corresponding beam waist diameter  $d_0$  and the divergence angle  $\theta_{\text{div}}$  of the investigated laser beam can be determined. With these two parameters the desired beam propagation ratio, either  $M_{1/e^2}^2$  or  $M_{4\sigma}^2$ , can be calculated according to Eq. (2.12). Unlike any other approach, the second order moments method provides a reliable way to determine the beam quality of any laser beam [192]. With the applied measuring method, the beam propagation ratio  $M_{4\sigma}^2$  can be determined with an accuracy of approx.  $10 \%$ . The beam propagation ratio  $M_{1/e^2}^2$ , on the other hand, provides an estimated value for the beam quality of the laser beam central lobe.

## Application of a microscope objective lens

The near-infrared beam waist profile in front of the waveguide SHG device cannot be recorded directly, since its diameter corresponds to the pixel size

of the CCD camera. Therefore, a microscope objective has to be applied in order to magnify this intensity distribution. For this purpose, a planachromatic microscope objective lens from Carl Zeiss Jena, characterized by a corrected chromatic aberration and a corrected field curvature, was used. The microscope objective lens is characterized by a magnification power of 25 when the image of the object is formed in infinity. The numerical aperture of 0.5 results in a resolving power of approx.  $0.9 \mu\text{m}^{-1}$ , calculated according to Rayleigh's criterion [48, p. 472] for a wavelength of 1064 nm.

The microscope objective lens and the CCD camera are mounted in a fixed distance, as presented in Fig. A.2. This defines the image plane of the magnifying optical system at a finite interval resulting in a different magnification power than designed. In addition, slight aberrations can occur in this configuration, since the optical system is optimized to provide an image at an infinite interval. In the first step the measurement apparatus needs to be calibrated with respect to its magnifying power. For this purpose, a vertical slit with a width of approx.

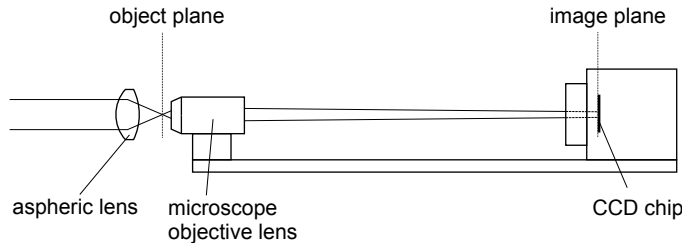


**Figure A.2:**  
Schematic depiction of a magnifying apparatus

$5 \mu\text{m}$  is placed in a collimated laser beam. The whole measurement apparatus is placed behind the slit and moved along the optical axis as a single unit until the image on the camera reaches the smallest width - this defines the object plane of the magnifying system (Fig. A.2). Subsequently, the slit in front of the microscope objective lens is moved in defined steps in the transversal direction. The comparison of the slit step size and the corresponding image shift on the camera defines the magnifying factor of this configuration. A value of  $20.1 \pm 0.2$ , determined during the calibration, was applied in order to scale the recorded power density distribution.

## A.2 Propagation of uncertainty

Due to measurement limitations, physical quantities  $x_i$  measured in an experiment possess uncertainties  $s_{x_i}$ . The uncertainty of a function  $f$  depending on these independent physical quantities is given by

$$s_f = \sqrt{\sum_i \left( \frac{\partial f}{\partial x_i} s_{x_i} \right)^2} \quad (\text{A.1})$$

according to [193]. This definition for propagation of uncertainty was applied throughout this work.



# List of publications

The content of this work has contributed to following scientific publications:

## Articles

JEDRZEJCZYK, D., R. GÜTHER, K. PASCHKE, G. ERBERT and G. TRÄNKLE: *Diode laser frequency doubling in a ppMgO:LN ridge waveguide: influence of structural imperfection, optical absorption and heat generation*. Applied Physics B, 109:33–42, 2012.

JEDRZEJCZYK, D., R. GÜTHER, K. PASCHKE, W.-J. JEONG, H.-J. LEE, and G. ERBERT: *Efficient high-power frequency doubling of distributed Bragg reflector tapered laser radiation in a periodically poled MgO-doped lithium niobate planar waveguide*. Optics Letters, 36(3):367–369, 2011.

JEDRZEJCZYK, D., R. GÜTHER, K. PASCHKE, B. EPPICH and G. ERBERT: *200 mW at 488 nm From a ppMgO:LN Ridge Waveguide by Frequency Doubling of a Laser Diode Module*. IEEE Photonics Technology Letters, 22(17):1282–1284, 2010.

FIEBIG, C., J. FRICKE, M. UEBERNICKEL, D. JEDRZEJCZYK, A. SAHM, and K. PASCHKE: *Watt-class green-emitting laser modules using direct second harmonic generation of diode laser radiation*. Optical Review, 19:405–408, 2012.

PASCHKE, K., D. JEDRZEJCZYK and C. FIEBIG: *Compact lasers for medical technology and displays (in German)*. Optik & Photonik, 5(3):43–46, 2010.

MAIWALD, M., D. JEDRZEJCZYK, A. SAHM, K. PASCHKE, R. GÜTHER, B. SUMPFF, G. ERBERT and G. TRÄNKLE: *Second-harmonic-generation microsystem light source at 488 nm for Raman spectroscopy*. Optics Letters, 34(2):217–219, 2009.

## Conference Talks and Proceedings

JEDRZEJCZYK, D., D. FEISE, R. GÜTHER, K. PASCHKE and G. ERBERT: *1 W at 531 nm generated in a ppMgO:LN planar waveguide by means of frequency doubling of a DBR tapered diode laser*. SPIE Proc., 7917:791703, 2011

PASCHKE, K., C. FIEBIG, G. BLUME, A. SAHM, D. JEDRZEJCZYK, D. FEISE and G. ERBERT: *Miniaturized highly brilliant diode laser modules*

*for future display applications.* The Laser Display Conference 2013, Yokohama, Japan, LDC9-2, 2013.

PASCHKE, K., C. FIEBIG, G. BLUME, A. SAHM, D. JEDRZEJCZYK, D. FEISE and G. ERBERT: *Highly brilliant diode laser modules for the visible spectral range.* Optic and Photonics Taiwan 2012, Taipei, Taiwan, BLR215, 2012.

FIEBIG, C., J. FRICKE, M. UEBERNICKEL, D. JEDRZEJCZYK, A. SAHM and K. PASCHKE, : *Diode laser based Watt class SHG modules.* The Laser Display Conference 2012, Yokohama, Japan, LDC5-2, 2012.

LIU, P. Q., C. FIEBIG, M. UEBERNICKEL, G. BLUME, D. FEISE, A. SAHM, D. JEDRZEJCZYK, K. PASCHKE and G. ERBERT: *High-power (1.1 W) green (532 nm) laser source based on single-pass second harmonic generation on a compact micro-optical bench.* SPIE Proc., 7917:791704, 2011.

# Bibliography

- [1] MAIMAN, T. H.: *Stimulated Optical Radiation in Ruby*. Nature, 187(4736):493–494, 1960.
- [2] TRAINOR, GEORGE L.: *DNA sequencing, automation, and the human genome*. Analytical Chemistry, 62(5):418–426, 1990.
- [3] MAIWALD, MARTIN, HEINAR SCHMIDT, BERND SUMPFF, REINER GÜTHER, GÖTZ ERBERT, HEINZ-DETLEF KRONFELDT and GÜNTHER TRÄNKLE: *Microsystem Light Source at 488 nm for Shifted Excitation Resonance Raman Difference Spectroscopy*. Applied Spectroscopy, 63(11):1283–1287, 2009.
- [4] BHATIA, VIKRAM, ANTHONY S. BAUCO, HASSAN M. OUBEI and DAVID A. S. LOEBER: *Efficient green lasers for high-resolution scanning micro-projector displays*. SPIE Proc., 7582:758205, 2010.
- [5] MÜLLER, ANDRÉ, OLE BJARLIN JENSEN, ANGELIKA UNTERHUBER, TUAN LE, ANDREAS STINGL, KARL-HEINZ HASLER, BERND SUMPFF, GÖTZ ERBERT, PETER E. ANDERSEN and PAUL MICHAEL PETERSEN: *Frequency-doubled DBR-tapered diode laser for direct pumping of Ti:sapphire lasers generating sub-20 fs pulses*. Optics Express, 19(13):12156–12163, 2011.
- [6] MICHIEUE, ATSUO, TAKASHI MIYOSHI, TOMOYA YANAMOTO, TOKUYA KOZAKI, SHIN ICHI NAGAHAMA, YUKIO NARUKAWA, MASAHIKO SANO, TAKAO YAMADA and TAKASHI MUKAI: *Recent development of nitride LEDs and LDs*. SPIE Proc., 7216:72161Z, 2009.
- [7] SCHMIDT, MATHEW C., CHRISTIANE POBLENZ, YU-CHIA CHANG, BEN LI, MARK J. MONDRY, JUSTIN IVELAND, MICHAEL R. KRAMES, RICHARD CRAIG, JAMES W. RARING, JAMES S. SPECK, STEVEN P. DENBAARS and SHUJI NAKAMURA: *High-performance blue and green laser diodes based on nonpolar/semipolar GaN substrates*. SPIE Proc., 8039:80390D, 2011.
- [8] LUTGEN, STEPHAN, DIMITRI DINI, INES PIETZONKA, SOENKE TAUTZ, ANDREAS BREIDENASSEL, ALFRED LELL, ADRIAN AVRAMESCU, CHRISTOPH EICHLER, TERESA LERMER, JENS MÜLLER, GEORG BRUEDERL, ALVARO GOMEZ-IGLESIAS, UWE STRAUSS, WOLFGANG G. SCHEIBENZUBER, ULRICH T. SCHWARZ,

- BERNHARD PASENOW and STEPHAN KOCH: *Recent results of blue and green InGaN laser diodes for laser projection*. SPIE Proc., 7953:79530G, 2011.
- [9] JENSEN, OLE BJARLIN, PETER E. ANDERSEN, BERND SUMPFF, KARL-HEINZ HASLER, GOETZ ERBERT and PAUL MICHAEL PETERSEN: *1.5 W green light generation by single-pass second harmonic generation of a single-frequency tapered diode laser*. Optics Express, 17(8):6532–6539, 2009.
- [10] FIEBIG, C., S. PEKAREK, K. PASCHKE, M. UEBERNICKEL, T. SÜDMEYER, U. KELLER and G. ERBERT: *High-brightness distributed-Bragg-reflector tapered diode lasers: pushing your application to the next level*. SPIE Proc., 7918:79180R, 2011.
- [11] HARA, TOKUTAKA, MIKI YATSUKI, YUJI YAMANE, HITOSHI OGURI and MASAHITO MURE: *Novel 560 nm yellow-green laser using stabilized broad-area laser diode and PPLN waveguide*. In *QELS*, volume 2, pages 856–858, JTuC26, Optical Society of America, 2005.
- [12] LEE, WON-KYU, CHANG YONG PARK, DAI-HYUK YU, SANG EON PARK, SANG-BUM LEE and TAEG YONG KWON: *Generation of 578-nm yellow light over 10 mW by second harmonic generation of an 1156-nm external-cavity diode laser*. Optics Express, 19(18):17453–17461, 2011.
- [13] HOEFER, T., M. SCHMITT, T. SCHWARZ, M. KUEHNELT, R. SCHULZ, I. PIETZONKA, H. LINDBERG, C. LAUER, S. LUTGEN, U. STEEGMUELLER and U. STRAUSS: *High-performance at low cost: the challenge manufacturing frequency doubled green semiconductor lasers for mass markets*. SPIE Proc., 7582:758207, 2010.
- [14] KHAYDAROV, JOHN, STEPAN ESSAIAN, ANDREI SHCHEGROV, SLAV SLAVOV, GEVORG GABRIELIAN, ARMEN POGHOSYAN and SUREN SOGHOMONYAN: *Modulation and efficiency characteristics of miniature microchip green laser sources based on PPMgOLN nonlinear material*. SPIE Proc., 7917:791705, 2011.
- [15] LU, YANG, QING-YANG XU, YI GAN and CHANG-QING XU: *MgO:PPLN based green lasers for portable laser projectors*. SPIE Proc., 8280:828004, 2012.
- [16] STROTKAMP, MICHAEL, THOMAS SCHWARZ, BERND JUNGLUTH, HEINRICH FAIDEL and MICHAEL LEERS: *Efficient, green laser based on a blue-diode pumped rare-earth-doped fluoride crystal in an extremely short resonator*. SPIE Proc., 7578:75780O, 2010.
- [17] HANSEN, NILS-OWE, AUDE-REINE BELLANCOURT, ULRICH WEICHMANN and GÜNTER HUBER: *Efficient green continuous-wave las-*

- ing of blue-diode-pumped solid-state lasers based on praseodymium-doped LiYF<sub>4</sub>*. Applied Optics, 49(20):3864–3868, 2010.
- [18] GÜN, TEOMAN, PHILIP METZ and GÜNTER HUBER: *Power scaling of laser diode pumped Pr<sup>3+</sup>:LiYF<sub>4</sub> cw lasers: efficient laser operation at 522.6 nm, 545.9 nm, 607.2 nm, and 639.5 nm*. Optics Letters, 36(6):1002–1004, 2011.
- [19] FIEBIG, CHRISTIAN, ALEXANDER SAHM, MIRKO UEBERNICKEL, GUNNAR BLUME, BERND EPPICH, KATRIN PASCHKE and GÖTZ ERBERT: *Compact second-harmonic generation laser module with 1 W optical output power at 490 nm*. Optics Express, 17(25):22785–22790, 2009.
- [20] LIU, P. Q., C. FIEBIG, M. UEBERNICKEL, G. BLUME, D. FEISE, A. SAHM, D. JEDRZEJCZYK, K. PASCHKE and G. ERBERT: *High-power (1.1W) green (532nm) laser source based on single-pass second harmonic generation on a compact micro-optical bench*. SPIE Proc., 7917:791704, 2011.
- [21] BOYD, G. D. and D. A. KLEINMAN: *Parametric Interaction of Focused Gaussian Light Beams*. Journal of Applied Physics, 39(8):3597–3639, 1968.
- [22] NATHAN, MARSHALL I., WILLIAM P. DUMKE, GERALD BURNS, JR. FREDERICK H. DILL and GORDON LASHER: *Stimulated emission of radiation from GaAs p-n junctions*. Applied Physics Letters, 1(3):62–64, 1962.
- [23] HALL, R. N., G. E. FENNER, J. D. KINGSLEY, T. J. SOLTYS and R. O. CARLSON: *Coherent Light Emission From GaAs Junctions*. Physical Review Letters, 9:366–368, 1962.
- [24] HOLONYAK, N. JR. and S. F. BEVACQUA: *Coherent (visible) light emission from Ga(As<sub>1-x</sub>P<sub>x</sub>) junctions*. Applied Physics Letters, 1(4):82–83, 1962.
- [25] QUIST, T. M., R. H. REDIKER, R. J. KEYES, W. E. KRAG, B. LAX, A. L. MCWHORTER and H. J. ZEIGLER: *Semiconductor Maser of GaAs*. Applied Physics Letters, 1(4):91–92, 1962.
- [26] QUIST, T. M., R. H. REDIKER, W. E. KRAG, B. LAX, A. L. MCWHORTER and H. J. ZEIGER: *Erratum: Semiconductor Maser of GaAs*. Applied Physics Letters, 2(1):22–22, 1963.
- [27] HAYASHI, I., M. B. PANISH, P. W. FOY and S. SUMSKI: *Junction lasers which operate continuously at room temperature*. Applied Physics Letters, 17(3):109–111, 1970.

- [28] PANISH, M. B., I. HAYASHI and S. SUMSKI: *Double-heterostructure injection lasers with room-temperature thresholds as low as 2300 A/cm<sup>2</sup>*. Applied Physics Letters, 16(8):326–327, 1970.
- [29] HARTMAN, R. L., J. C. DYMENT, C. J. HWANG and M. KUHN: *Continuous operation of GaAs/Single Bond/Ga<sub>1-x</sub>Al<sub>x</sub>As double-heterostructure lasers with 30 [degree]C half-lives exceeding 1000 h*. Applied Physics Letters, 23(4):181–183, 1973.
- [30] HARTMAN, R.L., J.C. DYMENT, C.J. HWANG and M. KUHN: *Erratum: Continuous operations of GaAs/Single Bond/Ga<sub>1-x</sub>Al<sub>x</sub>As double-heterostructure lasers with 30[degree]C half-lives exceeding 1000 h*. Applied Physics Letters, 23(8):491–491, 1973.
- [31] HARTMAN, R. L., N. E. SCHUMAKER and R. W. DIXON: *Continuously operated (Al,Ga)As double-heterostructure lasers with 70 [degree]C lifetimes as long as two years*. Applied Physics Letters, 31(11):756–759, 1977.
- [32] ZAPPE, HANS P.: *Laser Diode Microsystems*. Springer, 2004.
- [33] KANSKAR, M., T. EARLES, T.J. GOODNOUGH, E. STIERS, D. BOTEZ and L.J. MAWST: *73 % CW power conversion efficiency at 50 W from 970 nm diode laser bars*. Electronics Letters, 41:245–247, 2005.
- [34] ERBERT, GÖTZ, FRANK BUGGE, ANDREA KNIGGE, RALF STASKE, BERND SUMPFF, HANS WENZEL and GÜNTHER TRÄNKLE: *Highly reliable 75 W InGaAs/AlGaAs laser bars with over 70 % conversion efficiency*. SPIE Proc., 6133:61330B, 2006.
- [35] CRUMP, PAUL A., MIKE GRIMSHAW, JUN WANG, WEIMIN DONG, SHIGUO ZHANG, SUHIT DAS, JASON FARMER, MARK DEVITO, LEI S. MENG and JASON K. BRASSEUR: *85 % Power Conversion Efficiency 975-nm Broad Area Diode Lasers at - 50° C, 76 % at 10° C*. In *CLEO/QELS, JWB24*, Optical Society of America, 2006.
- [36] SCHULTZ, C. M., P. CRUMP, A. MAASSDORF, O. BROX, F. BUGGE, A. MOGILATENKO, H. WENZEL, S. KNIGGE, B. SUMPFF, M. WEYERS, G. ERBERT and G. TRÄNKLE: *In situ etched gratings embedded in AlGaAs for efficient high power 970 nm distributed feedback broad-area lasers*. Applied Physics Letters, 100(20):201115, 2012.
- [37] PEKAREK, SELINA, CHRISTIAN FIEBIG, MAX CHRISTOPH STUMPF, ANDREAS ERNST HEINZ OEHLER, KATRIN PASCHKE, GÖTZ ERBERT, THOMAS SÜDMEYER and URSULA KELLER: *Diode-pumped gigahertz femtosecond Yb:KGW laser with a peak power of 3.9 kW*. Optics Express, 18(16):16320–16326, 2010.

- 
- [38] PIETRZAK, AGNIESZKA, PAUL CRUMP, HANS WENZEL, GÖTZ ERBERT, FRANK BUGGE and GÜNTHER TRÄNKLE: *Combination of Low-Index Quantum Barrier and Super Large Optical Cavity Designs for Ultranarrow Vertical Far-Fields From High-Power Broad-Area Lasers*. IEEE Journal of Selected Topics in Quantum Electronics, 17:1715–1722, 2011.
- [39] SUMPFF, B., A. KLEHR, G. ERBERT and G. TRÄNKLE: *Application of 940 nm high-power DFB lasers for line-broadening measurements at normal pressure using a robust and compact setup*. Applied Physics B, 106:357–364, 2012.
- [40] MAIWALD, MARTIN, HEINAR SCHMIDT, BERND SUMPFF, GÖTZ ERBERT, HEINZ-DETLEF KRONFELDT and GÜNTHER TRÄNKLE: *Microsystem 671 nm light source for shifted excitation Raman difference spectroscopy*. Applied Optics, 48(15):2789–2792, 2009.
- [41] BAWAMIA, A.I., G. BLUME, B. EPPICH, A. GINOLAS, S. SPIESSBERGER, M. THOMAS, B. SUMPFF and G. ERBERT: *Miniaturized Tunable External Cavity Diode Laser with Single-Mode Operation and a Narrow Linewidth at 633 nm*. IEEE Photonics Technology Letters, 23(22):1676–1678, 2011.
- [42] SPIESSBERGER, STEFAN, MAX SCHIEMANGK, ALEXANDER SAHM, ANDREAS WICHT, HANS WENZEL, ACHIM PETERS, GÖTZ ERBERT and GÜNTHER TRÄNKLE: *Micro-integrated 1 Watt semiconductor laser system with a linewidth of 3.6 kHz*. Optics Express, 19(8):7077–7083, 2011.
- [43] SPIESSBERGER, STEFAN, MAX SCHIEMANGK, ALEXANDER SAHM, FRANK BUGGE, JÖRG FRICKE, HANS WENZEL, ANDREAS WICHT, GÖTZ ERBERT and GÜNTHER TRÄNKLE: *All-semiconductor-based narrow linewidth high-power laser system for laser communication applications in space at 1060 nm*. SPIE Proc., 8246:82460I6, 2012.
- [44] ZAPPE, HANS P.: *Introduction to semiconductor integrated optics*. Artech House, Inc., 1995.
- [45] DIEHL, ROLAND: *High-Power Diode Lasers*. Springer, 2000.
- [46] ZIEL, J. P. VAN DER, R. DINGLE, R. C. MILLER, W. WIEGMANN and JR. W. A. NORDLAND: *Laser oscillation from quantum states in very thin GaAs - Al<sub>0.2</sub>Ga<sub>0.8</sub>As multilayer structures*. Applied Physics Letters, 26(8):463–465, 1975.
- [47] ILROY, P.M., A. KUROBE and Y. UEMATSU: *Analysis and application of theoretical gain curves to the design of multi-quantum-well lasers*. IEEE Journal of Quantum Electronics, 21(12):1958–1963, 1985.
- [48] HECHT, EUGENE: *Optics*. Addison-Wesley, 4<sup>th</sup> edition, 2002.
-

- [49] BROX, O., F. BUGGE, A. GINOLAS, A. KLEHR, P. RESSEL, H. WENZEL, G. ERBERT and G. TRÄNKLE: *High-power ridge waveguide DFB and DFB-MOPA lasers at 1064 nm with a vertical farfield angle of 15°*. SPIE Proc., 7616:761610, 2010.
- [50] FRICKE, J., H. WENZEL, M. MATAALLA, A. KLEHR and G. ERBERT: *980-nm DBR lasers using higher order gratings defined by i-line lithography*. Semiconductor Science and Technology, 20:1149–1152, 2005.
- [51] FRICKE, J., H. WENZEL, F. BUGGE, O.P. BROX, A. GINOLAS, W. JOHN, P. RESSEL, L. WEIXELBAUM and G. ERBERT: *High-Power Distributed Feedback Lasers With Surface Gratings*. IEEE Photonics Technology Letters, 24(16):1443–1445, 2012.
- [52] KOGELNIK, H. and C. V. SHANK: *Coupled-Wave Theory of Distributed Feedback Lasers*. Journal of Applied Physics, 43(5):2327–2335, 1972.
- [53] YARIV, A.: *Coupled-mode theory for guided-wave optics*. IEEE Journal of Quantum Electronics, 9(9):919–933, 1973.
- [54] FRICKE, J., W. JOHN, A. KLEHR, P. RESSEL, L. WEIXELBAUM, H. WENZEL and G. ERBERT: *Properties and fabrication of high-order Bragg gratings for wavelength stabilization of diode lasers*. Semiconductor Science and Technology, 27(5):055009, 2012.
- [55] KOECHNER, WALTER: *Solid-state laser engineering (6th edition)*. Springer Science+Business Media, Inc, 6<sup>th</sup> edition, 2006.
- [56] MESCHEDER, DIETER: *Optik, Licht und Laser (in German)*. B. G. Teubner Stuttgart Leipzig, 1999.
- [57] HEMPEL, MARTIN, FABIO LA MATTINA, JENS W. TOMM, UTE ZEIMER, ROLF BROENNIMANN and THOMAS ELSAESSER: *Defect evolution during catastrophic optical damage of diode lasers*. Semiconductor Science and Technology, 26(7):075020, 2011.
- [58] TOMM, JENS W., MATHIAS ZIEGLER, THOMAS ELSAESSER, HENNING E. LARSEN, PAUL M. PETERSEN, PETER E. ANDERSEN, SØNNIK CLAUSEN, UTE ZEIMER and DAVID FENDLER: *Catastrophic optical mirror damage in diode lasers monitored during single pulse operation*. SPIE Proc., 7616:76161G, 2010.
- [59] ZIEGLER, MATHIAS, JENS W. TOMM, UTE ZEIMER and THOMAS ELSAESSER: *Imaging Catastrophic Optical Mirror Damage in High-Power Diode Lasers*. Journal of Electronic Materials, 39:709–714, 2010.
- [60] FRANKEN, P. A., G. WEINREICH, C. W. PETERS and A. E. HILL: *Generation Of Optical Harmonics*. Physical Review Letters, 7(4):118–119, 1961.

- 
- [61] ARMSTRONG, J. A., N. BLOEMBERGEN, J. DUCUING and P. S. PERSHAN: *Interactions between Light Waves in a Nonlinear Dielectric*. Physical Review, 127(6):1918–1939, 1962.
- [62] ACHMANOV, S.A. and R.V. CHOCHLOV: *Problems of Nonlinear Optics (in Russian)*. Itogi Nauki, Moscow, 1964.
- [63] KLEINMAN, D. A. and R. C. MILLER: *Dependence of Second-Harmonic Generation on the Position of the Focus*. Physical Review, 148:302–312, 1966.
- [64] MCGEOCH, M. and R. SMITH: *Optimum second-harmonic generation in lithium niobate*. IEEE Journal of Quantum Electronics, 6(4):203–205, 1970.
- [65] HELMFRID, STEN and GUNNAR ARVIDSSON: *Second-harmonic generation in quasi-phase-matching waveguides with a multimode pump*. J. Opt. Soc. Am. B, 8(11):2326–2330, 1991.
- [66] QU, YUJIANG and SURENDRA SINGH: *Second-harmonic generation and photon bunching in multimode laser beams*. Physical Review A, 47(4):3259–3263, 1993.
- [67] KONTUR, F. J., I. DAJANI, YALIN LU and R. J. KNIZE: *Frequency-doubling of a CW fiber laser using PPKTP, PPMgSLT, and PPMgLN*. Optics Express, 15(20):12882–12889, 2007.
- [68] NYGA, SEBASTIAN, JENS GEIGER and BERND JUNGBLUTH: *Frequency doubling of fiber laser radiation of large spectral bandwidths*. SPIE Proc., 7578:75780P, 2010.
- [69] SHENG, SHINAN-CHUR and A. E. SIEGMAN: *Nonlinear-optical calculations using fast-transform methods: Second-harmonic generation with depletion and diffraction*. Physical Review A, 21:599–606, 1980.
- [70] GÜTHER, R.: *Optimisation of SHG for high-brightness semiconductor laser diode radiation with large aberrations*. In *DGaO Proc.*, 106th Convention, Poster P44, 2005.
- [71] GÜTHER, R., G. BLUME, M. UEBERNICKEL, C. FIEBIG, K. PASCHKE, A. GINOLAS, B. EPPICH and G. ERBERT: *Generation of Second Harmonic with non-diffraction limited radiation*. In *DGaO Proc.*, 109th Convention, Poster P45, 2008.
- [72] BLUME, G., M. UEBERNICKEL, C. FIEBIG, K. PASCHKE, A. GINOLAS, B. EPPICH, R. GÜTHER and G. ERBERT: *Rayleigh length dependent SHG conversion at 488 nm using a monolithic DBR tapered diode laser*. SPIE Proc., 6875:68751C, 2008.
-

- [73] UEBERNICKEL, M., R. GÜTHER, G. BLUME, C. FIEBIG, K. PASCHKE and G. ERBERT: *Study of the properties of the SHG with diode lasers*. Applied Physics B, 99(3):457–464, 2010.
- [74] WENZEL, H., J. FRICKE, A. KLEHR, A. KNAUER and G. ERBERT: *High-power 980-nm DFB RW lasers with a narrow vertical far field*. IEEE Photonics Technology Letters, 18:737–739, 2006.
- [75] NGUYEN, H. K., S. COLEMAN, N. J. VISOVSKY, Y. LI, K. SONG, R. W. DAVIS, JUN, M. H. HU and C. ZAH: *Reliable high-power 1060 nm DBR lasers for second-harmonic generation*. Electronics Letters, 43(13):716–717, 2007.
- [76] ACHTENHAGEN, MARTIN, NUDITHA VIBHAVIE AMARASINGHE, LINGLIN JIANG, JEFFREY THREADGILL and PRESTON YOUNG: *Spectral Properties of High-Power Distributed Bragg Reflector Lasers*. Journal of Lightwave Technology, 27:3433–3437, 2009.
- [77] PASCHKE, K., S. SPIESSBERGER, C. KASPARI, D. FEISE, C. FIEBIG, G. BLUME, H. WENZEL, A. WICHT and G. ERBERT: *High-power distributed Bragg reflector ridge-waveguide diode laser with very small spectral linewidth*. Optics Letters, 35(3):402–404, 2010.
- [78] LI, JIN, DMITRI V. KUKSENKOV, WAYNE LIU, YABO LI, NICK J. VISOVSKY, DRAGAN PIKULA, ALBERT P. HEBERLE, GORDON C. BROWN, GARRETT A. PIECH, DOUGLAS L. BUTLER and CHUNG EN ZAH: *Wavelength tunable high-power single-mode 1060-nm DBR lasers*. SPIE Proc., 8277:82771L, 2012.
- [79] FIEBIG, C., G. BLUME, C. KASPARI, D. FEISE, J. FRICKE, M. MATALLA, W. JOHN, H. WENZEL, K. PASCHKE and G. ERBERT: *12 W high-brightness single-frequency DBR tapered diode laser*. Electronics Letters, 44:1253–1255, 2008.
- [80] FIEBIG, CHRISTIAN, GUNNAR BLUME, MIRKO UEBERNICKEL, DAVID FEISE, CHRISTIAN KASPARI, KATRIN PASCHKE, JÖRG FRICKE, HANS WENZEL and GÖTZ ERBERT: *High-power DBR tapered laser at 980 nm for single path second harmonic generation*. IEEE Journal of Selected Topics in Quantum Electronic, 15(3):978–983, 2009.
- [81] SUMPFF, B., K.-H. HASLER, P. ADAMIEC, F. BUGGE, J. FRICKE, P. RESSEL, H. WENZEL, G. ERBERT and G. TRÄNKLE: *1060 nm DBR tapered lasers with 12 W output power and a nearly diffraction limited beam quality*. SPIE Proc., 7230:72301E, 2009.
- [82] OSOWSKI, M. L., W. HU, R. M. LAMMERT, T. LIU, Y. MA, S. W. OH, C. PANJA, P. T. RUDY, T. STAKELON and J. E. UNGAR: *High brightness semiconductor lasers*. SPIE Proc., 6456:64560D, 2007.

- 
- [83] WENZEL, H., K. PASCHKE, O. BROX, F. BUGGE, J. FRICKE, A. GINOLAS, A. KNAUER, P. RESSEL and G. ERBERT: *10 W continuous-wave monolithically integrated master-oscillator power-amplifier*. Electronics Letters, 43:160–162, 2007.
- [84] SPREEMANN, M., M. LICHTNER, M. RADZIUNAS, U. BANDELOW, and H. WENZEL: *Measurement and Simulation of Distributed-Feedback Tapered Master-Oscillators Power-Amplifiers*. IEEE Journal of Quantum Electronics, 45:609–616, 2009.
- [85] JEDRZEJCZYK, D., O. BROX, F. BUGGE, J. FRICKE, A. GINOLAS, K. PASCHKE, H. WENZEL and G. ERBERT: *High-power distributed-feedback tapered master-oscillator power amplifiers emitting at 1064 nm*. SPIE Proc., 7583:758317, 2010.
- [86] RESSEL, P., G. ERBERT, U. ZEIMER, K. HAUSLER, G. BEISTER, B. SUMPFF, A. KLEHR and G. TRÄNKLE: *Novel passivation process for the mirror facets of Al-free active-region high-power semiconductor diode lasers*. IEEE Photonics Technology Letters, 17(5):962–964, 2005.
- [87] SUJECKI, S., L. BORRUEL, J. WYKES, P. MORENO, B. SUMPFF, P. SEWELL, H. WENZEL, T.M. BENSON, G. ERBERT, I. ESQUIVIAS and E.C. LARKINS: *Nonlinear properties of tapered laser cavities*. IEEE Journal of Selected Topics in Quantum Electronics, 9(3):823–834, 2003.
- [88] BORRUEL, L., S. SUJECKI, P. MORENO, J. WYKES, M. KRAKOWSKI, B. SUMPFF, P. SEWELL, S.-C. AUZANNEAU, H. WENZEL, D. RODRIGUEZ, T.M. BENSON, E.C. LARKINS and I. ESQUIVIAS: *Quasi-3-D simulation of high-brightness tapered lasers*. IEEE Journal of Quantum Electronics, 40(5):463–472, 2004.
- [89] BORRUEL, LUIS, HELENA ODRIOZOLA, JOSE TIJERO, IGNACIO ESQUIVIAS, SLAWOMIR SUJECKI and ERIC LARKINS: *Design strategies to increase the brightness of gain guided tapered lasers*. Optical and Quantum Electronics, 40(2-4):175–189, 2008.
- [90] TIEN, P. K., R. ULRICH and R. J. MARTIN: *Optical second harmonic generation in form of coherent Čerenkov radiation from a thin-film waveguide*. Applied Physics Letters, 17(10):447–450, 1970.
- [91] BURNS, W. K. and A. B. LEE: *Observation of noncritically phase-matched second-harmonic generation in an optical waveguide*. Applied Physics Letters, 24(5):222–224, 1974.
- [92] UESUGI, NAOSHI and TATSUYA KIMURA: *Efficient second-harmonic generation in three-dimensional LiNbO<sub>3</sub> optical waveguide*. Applied Physics Letters, 29(9):572–574, 1976.
- [93] REGENER, R. and W. SOHLER: *Efficient second-harmonic generation in Ti:LiNbO<sub>3</sub> channel waveguide resonators*. J. Opt. Soc. Am. B, 5(2):267–277, 1988.
-

- [94] LAURELL, FREDRIK and GUNNAR ARVIDSSON: *Frequency doubling in Ti:MgO:LiNbO<sub>3</sub> channel waveguides*. J. Opt. Soc. Am. B, 5(2):292–299, 1988.
- [95] WEBJORN, J., S. SIALA, D.W. NAM, R.G. WAARTS and R.J. LANG: *Visible laser sources based on frequency doubling in nonlinear waveguides*. IEEE Journal of Quantum Electronics, 33(10):1673–1686, 1997.
- [96] FEJER, M. M., M. J. F. DIGONNET and R. L. BYER: *Generation of 22 mW of 532-nm radiation by frequency doubling in Ti:MgO:LiNbO<sub>3</sub> waveguides*. Optics Letters, 11(4):230–232, 1986.
- [97] FLUCK, D., B. BINDER, M. KÜPFER, H. LOOSER, CH. BUCHAL and P. GÜNTER: *Phase-matched second harmonic blue light generation in ion implanted KNbO<sub>3</sub> planar waveguides with 29% conversion efficiency*. Optics Communications, 90(4-6):304–310, 1992.
- [98] ZHANG, L., P. J. CHANDLER, P. D. TOWNSEND, Z. T. ALWAHABI, S. L. PITAYANA and A. J. MCCAFFERY: *Frequency doubling in ion-implanted KTiOPO<sub>4</sub> planar waveguides with 25% conversion efficiency*. Journal of Applied Physics, 73(6):2695–2699, 1993.
- [99] WEBJORN, J., S. MACCORMACK and R. WAARTS: *Efficient quasi-phase-matched frequency doubling of a high power, unpolarized fiber laser source*. In *CLEO 1998 Technical Digest. Summaries of papers presented at the Conference*, page 76, 1998.
- [100] IWAI, M., T. YOSHINO, S. YAMAGUCHI, M. IMAEDA, N. PAVEL, I. SHOJI and T. TAIRA: *High-power blue generation from a periodically poled MgO:LiNbO<sub>3</sub> ridge-type waveguide by frequency doubling of a diode end-pumped Nd:Y<sub>3</sub>Al<sub>5</sub>O<sub>12</sub> laser*. Applied Physics Letters, 83(18):3659–3661, 2003.
- [101] NGUYEN, HONG KY, M.H. HU, N. NISHIYAMA, N.J. VISOVSKY, YABO LI, KECHANG SONG, XINGSHENG LIU, J. GOLLIER, JR. HUGHES, L.C., R. BHAT and CHUNG-EN ZAH: *107-mW low-noise green-light emission by frequency doubling of a reliable 1060-nm DFB semiconductor laser diode*. IEEE Photonics Technology Letters, 18(5):682–684, 2006.
- [102] NGUYEN, H. K., M. H. HU, Y. LI, K. SONG, N. J. VISOVSKY, S. COLEMAN and C.-E. ZAH: *304 mW green light emission by frequency doubling of a high-power 1060-nm DBR semiconductor laser diode*. SPIE Proc., 6890:68900I, 2008.
- [103] LI, JIN, WAYNE LIU, YABO LI, NICK VISOVSKY, DRAGAN PIKULA, ALBERT HEBERLE, GORDON BROWN, GARRETT PIECH, DOUGLAS BUTLER and CHUNG-EN ZAH: *350 mW green light emission from a*

- directly frequency-doubled DBR laser in a compact package.* In *IEEE Photonics Conference 2011*, pages 292–293, 2011.
- [104] SAKAI, KIYOHIDE, YASUHARU KOYATA and YOSHIHITO HIRANO: *Planar-waveguide quasi-phase-matched second-harmonic-generation device in Y-cut MgO-doped LiNbO<sub>3</sub>.* *Optics Letters*, 31:3134–3136, 2006.
- [105] KOYATA, Y., K. SAKAI and Y. HIRANO: *Planar-waveguide quasi-phase matched second-harmonic generation device in Y-cut MgO-doped LiNbO<sub>3</sub>.* In *CLEO/QELS 2006*, pages 1–2, 2006.
- [106] SUN, JIAN and CHANQING XU: *466 mW green light generation using annealed proton-exchanged periodically poled MgO:LiNbO<sub>3</sub> ridge waveguides.* *Optics Letters*, 37(11):2028–2030, Jun 2012.
- [107] SAKAI, K., Y. KOYATA, S. ITAKURA and Y. HIRANO: *High-Power, Highly Efficient Second-Harmonic Generation in a Periodically Poled MgO:LiNbO<sub>3</sub> planar waveguide.* *Journal of Lightwave Technology*, 27(5):590–596, 2009.
- [108] SUHARA, T. and M. FUJIMURA: *Waveguide Nonlinear-Optic Devices.* Springer-Verlag, 2003.
- [109] DAMASK, JAY N.: *Polarization Optics in Telecommunications.* Springer, 2005.
- [110] HERZIGER, G. and R. POPRAWA: *Lecture transcript Laser Technology I (2nd Edition, in German).* Lehrstuhl für Lasertechnik der RWTH Aachen und Fraunhofer-Institut für Lasertechnik, 1998.
- [111] SUGITA, T., K. MIZUUCHI, K. YAMAMOTO, K. FUKUDA, T. KAI, I. NAKAYAMA and K. TAKAHASHI: *Highly efficient second-harmonic generation in direct-bonded MgO:LiNbO<sub>3</sub> pure crystal waveguide.* *Electronics Letters*, 40(21):1359–1361, 2004.
- [112] BOYD, ROBERT W.: *Nonlinear Optics (3rd Edition).* Elsevier, Acad. Press, 2008.
- [113] FRANKEN, P. A. and J. F. WARD: *Optical Harmonics And Nonlinear Phenomena.* *Reviews Of Modern Physics*, 35(1):23–39, 1963.
- [114] SHEN, YUEN-RON: *Principles of nonlinear optics.* Wiley-Interscience, 1<sup>st</sup> edition, 1984.
- [115] MIDWINTER, J. E. and J. WARNER: *The effects of phase matching method and of uniaxial crystal symmetry on the polar distribution of second-order non-linear optical polarization.* *British Journal of Applied Physics*, 16(8):1135, 1965.
- [116] RISK, W. P., T. R. GOSNELL and A. V. NURMIKKO: *Compact Blue-Green Lasers.* Cambridge University Press, 2003.

- [117] HUM, DAVID S. and MARTIN M. FEJER: *Quasi-phasematching*. Comptes Rendus Physique, 8(2):180–198, 2007.
- [118] FENG, D., N. B. MING, J. F. HONG, Y. S. YANG, J. S. ZHU, Z. YANG and Y. N. WANG: *Enhancement Of 2nd-Harmonic Generation In  $\text{LiNbO}_3$  Crystals With Periodic Laminar Ferroelectric Domains*. Applied Physics Letters, 37(7):607–609, 1980.
- [119] FEISST, A. and P. KOIDL: *Current Induced Periodic Ferroelectric Domain-Structures In  $\text{LiNbO}_3$  Applied For Efficient Nonlinear Optical Frequency Mixing*. Applied Physics Letters, 47(11):1125–1127, 1985.
- [120] YAMADA, M., N. NADA, M. SAITOH and K. WATANABE: *First-order quasi-phase matched  $\text{LiNbO}_3$  waveguide periodically poled by applying an external field for efficient blue second-harmonic generation*. Applied Physics Letters, 62:435–436, 1993.
- [121] JASKORZYNSKA, B., G. ARVIDSSON and F. LAURELL: *Periodic structures for phase-matching in second harmonic generation in titanium lithium niobate waveguides*. SPIE Proc., 651:221–228, 1986.
- [122] SUHARA, T. and H. NISHIHARA: *Theoretical analysis of waveguide second-harmonic generation phase matched with uniform and chirped gratings*. IEEE Journal of Quantum Electronics, 26:1265–1276, 1990.
- [123] FEJER, M. M., G. A. MAGEL, D. H. JUNDT and R. L. BYER: *Quasi-phase-matched second harmonic generation: tuning and tolerances*. IEEE Journal of Quantum Electronics, 28:2631–2654, 1992.
- [124] LAURELL, FREDRIK: *Periodically poled materials for miniature light sources*. Optical Materials, 11(2-3):235–244, 1999.
- [125] BORTZ, M. L., M. FUJIMURA and M. M. FEJER: *Increased acceptance bandwidth for quasi-phasematched second harmonic generation in  $\text{LiNbO}_3$  waveguides*. Electronics Letters, 30(1):34–35, 1994.
- [126] LEE, YEUNG LAK, YOUNG-CHUL NOH, CHANGSOO JUNG, TAE YU, DO-KYEONG KO and JONGMIN LEE: *Broadening of the second-harmonic phase-matching bandwidth in a temperature-gradient-controlled periodically poled  $\text{Ti:LiNbO}_3$  channel waveguide*. Optics Express, 11(22):2813–2819, 2003.
- [127] LEE, YEUNG LAK, YOUNG-CHUL NOH, CHANGSOO JUNG, TAE JUN YU, BONG-AHN YU, JONGMIN LEE, DO-KYEONG KO and KYUNGHWAN OH: *Reshaping of a second-harmonic curve in periodically poled  $\text{Ti:LiNbO}_3$  channel waveguide by a local-temperature-control technique*. Applied Physics Letters, 86(1):011104, 2005.

- 
- [128] MIZUUCHI, K., A. MORIKAWA, T. SUGITA and K. YAMAMOTO: *High-power continuous-wave ultraviolet generation by singlepass frequency doubling in periodically poled MgO:LiNbO<sub>3</sub>*. Electronics Letters, 39(25):1836–1838, 2003.
- [129] STIVALA, S., A. C. BUSACCA, A. PASQUAZI, R. L. OLIVERI, R. MORANDOTTI and G. ASSANTO: *Random quasi-phase-matched second-harmonic generation in periodically poled lithium tantalate*. Optics Letters, 35(3):363–365, 2010.
- [130] HELMFRID, STEN, GUNNAR ARVIDSSON and JONAS WEBJÖRN: *Influence of various imperfections on the conversion efficiency of second-harmonic generation in quasi-phase-matching lithium niobate waveguides*. J. Opt. Soc. Am. B, 10(2):222–229, 1993.
- [131] MIZUUCHI, K., K. YAMAMOTO and M. KATO: *Harmonic blue light generation in bulk periodically poled MgO:LiNbO<sub>3</sub>*. Electronics Letters, 32(22):2091–2092, 1996.
- [132] FLUCK, D.: *Theory on phase-matched second-harmonic generation in biaxial planar waveguides*. IEEE Journal of Quantum Electronics, 35(1):53–59, 1999.
- [133] SAKAI, KIYOHIDE, YASU HARU KOYATA, NAOYUKI SHIMADA, KIMITAKA SHIBATA, YOSHIHIKO HANAMAKI, SHIGETAKA ITAKURA, TETSUYA YAGI and YOSHIHITO HIRANO: *Master-oscillator power-amplifier scheme for efficient green-light generation in a planar MgO:PPLN waveguide*. Optics Letters, 33:431–433, 2008.
- [134] DMITRIEV, VALENTIN G., GAGIK G. GURZADYAN and DAVID N. NIKOGOSYAN: *Handbook of nonlinear crystals (3rd Revised Edition)*. Springer, 1999.
- [135] BORTZ, M. L., M. M. FEJER, D. W. NAM, R. G. WAARTS and D. F. WELCH: *Noncritical quasi-phase-matched second harmonic generation in an annealed proton-exchanged LiNbO<sub>3</sub> waveguide*. IEEE Journal of Quantum Electronics, 30:2953–2960, 1994.
- [136] JECHOW, ANDREAS, MARCO SCHEDEL, SANDRA STRY, JOACHIM SACHER and RALF MENZEL: *Highly efficient single-pass frequency doubling of a continuous-wave distributed feedback laser diode using a PPLN waveguide crystal at 488 nm*. Optics Letters, 32:3035–3037, 2007.
- [137] KEYS, R.W., A. LONI and R.M. DE LA RUE: *Measurement of the increase in the SHG coefficient of proton-exchanged LiNbO<sub>3</sub> after annealing using a grating diffraction technique*. Electronics Letters, 26(10):624–626, 1990.
- [138] CAO, X., R. SRIVASTAVA, R.V. RAMASWAMY and J. NATOUR: *Recovery of second-order optical nonlinearity in annealed proton-exchanged LiNbO<sub>3</sub>*. IEEE Photonics Technology Letters, 3(1):25–27, 1991.
-

- [139] BORTZ, M. L., L. A. EYRES and M. M. FEJER: *Depth profiling of the  $d$ /sub 33/ nonlinear coefficient in annealed proton exchanged LiNbO<sub>3</sub> waveguides*. Applied Physics Letters, 62(17):2012–2014, 1993.
- [140] MIZUUCHI, K., K. YAMAMOTO and M. KATO: *Harmonic blue light generation in X-cut MgO:LiNbO<sub>3</sub> waveguide*. Electronics Letters, 33(9):806–807, 1997.
- [141] SUGITA, TOMOYA, KIMINORI MIZUUCHI, YASUO KITAOKA and KAZUHISA YAMAMOTO: *31%-efficient blue second-harmonic generation in a periodically poled MgO:LiNbO<sub>3</sub> waveguide by frequency doubling of an AlGaAs laser diode*. Optics Letters, 24(22):1590–1592, 1999.
- [142] FUJIWARA, TAKUMI, RAMAKANT SRIVASTAVA, XIAOFAN CAO and RAMU V. RAMASWAMY: *Comparison of photorefractive index change in proton-exchanged and Ti-diffused LiNbO<sub>3</sub> waveguides*. Optics Letters, 18(5):346–348, 1993.
- [143] SHOJI, ICHIRO, TAKASHI KONDO, AYAKO KITAMOTO, MASAYUKI SHIRANE and RYOICHI ITO: *Absolute scale of second-order nonlinear-optical coefficients*. J. Opt. Soc. Am. B, 14(9):2268–2294, 1997.
- [144] FURUKAWA, YASUNORI, KENJI KITAMURA, SHUNJI TAKEKAWA, KAZUO NIWA and HIDEKI HATANO: *Stoichiometric Mg:LiNbO<sub>3</sub> as an effective material for nonlinear optics*. Optics Letters, 23(24):1892–1894, 1998.
- [145] FURUKAWA, Y., K. KITAMURA, S. TAKEKAWA, A. ALEXANDROVSKI, R.K. ROUTE, M.M. FEJER and G. FOULON: *Improved material properties in MgO-doped near-stoichiometric LiNbO<sub>3</sub> for nonlinear optical applications*. In *CLEO 2000*, pages 386–387, 2000.
- [146] FURUKAWA, Y., K. KITAMURA, S. TAKEKAWA, A. MIYAMOTO, M. TERAOKA and N. SUDA: *Photorefraction in LiNbO<sub>3</sub> as a function of [Li]/[Nb] and MgO concentrations*. Applied Physics Letters, 77(16):2494–2496, 2000.
- [147] ASOBE, MASAKI, OSAMU TADANAGA, TSUTOMU YANAGAWA, HIROKI ITOH and HIROYUKI SUZUKI: *Reducing photorefractive effect in periodically poled ZnO- and MgO-doped LiNbO<sub>3</sub> wavelength converters*. Applied Physics Letters, 78(21):3163–3165, 2001.
- [148] FURUKAWA, Y., K. KITAMURA, A. ALEXANDROVSKI, R. K. ROUTE, M. M. FEJER and G. FOULON: *Green-induced infrared absorption in MgO doped LiNbO<sub>3</sub>*. Applied Physics Letters, 78(14):1970–1972, 2001.
- [149] HIROHASHI, J., T. TAGO, O. NAKAMURA, A. MIYAMOTO and Y. FURUKAWA: *Characterization of GRIIRA properties in LiNbO<sub>3</sub> and LiTaO<sub>3</sub> with different compositions and doping*. SPIE Proc., 6875:687516, 2008.

- 
- [150] ASHKIN, A., G. D. BOYD, J. M. DZIEDZIC, R. G. SMITH, A. A. BALLMAN, J. J. LEVINSTEIN and K. NASSAU: *Optically-induced refractive index inhomogeneties in LiNbO<sub>3</sub> and LiTaO<sub>3</sub>*. Applied Physics Letters, 9(1):72–74, 1966.
- [151] BATCHKO, R.G., G.D. MILLER, A. ALEXANDROVSKI, M.M. FEJER and R.L. BYER: *Limitations of high-power visible wavelength periodically poled lithium niobate devices due to green-induced infrared absorption and thermal lensing*. In *CLEO 1998. Technical Digest. Summaries of papers presented at the Conference*, pages 75–76, 1998.
- [152] SCHWESYNG, J. R., M. C. C. KAJIYAMA, M. FALK, D. H. JUNDT, K. BUSE and M. M. FEJER: *Light absorption in undoped congruent and magnesium-doped lithium niobate crystals in the visible wavelength range*. Applied Physics B, 100:109–115, 2010.
- [153] LINDE, D. VON DER, A. M. GLASS and K. F. RODGERS: *Multiphoton photorefractive processes for optical storage in LiNbO<sub>3</sub>*. Applied Physics Letters, 25(3):155–157, 1974.
- [154] LOUCHEV, OLEG A., NAN EI YU, SUNAO KURIMURA and KENJI KITAMURA: *Thermal inhibition of high-power second-harmonic generation in periodically poled LiNbO<sub>3</sub> and LiTaO<sub>3</sub> crystals*. Applied Physics Letters, 87(13):131101, 2005.
- [155] LOUCHEV, OLEG A., NAN EI YU, SUNAO KURIMURA and KENJI KITAMURA: *Nanosecond pulsed laser energy and thermal field evolution during second harmonic generation in periodically poled LiNbO<sub>3</sub> crystals*. Journal of Applied Physics, 98(11):113103, 2005.
- [156] BRYAN, D. A., ROBERT GERSON and H. E. TOMASCHKE: *Increased optical damage resistance in lithium niobate*. Applied Physics Letters, 44(9):847–849, 1984.
- [157] VOLK, T. R., M. A. IVANOV, N. M. RUBININA, A. I. KHOLODNYKH and H. METZ: *Non-photorefractive LiNbO<sub>3</sub>:Mg as the effective material for the nonlinear optics*. Ferroelectrics, 95(1):121–125, 1989.
- [158] MILLER, G.D., R.G. BATCHKO, W.M. TULLOCH, D.R. WEISE, M.M. FEJER and R.L. BYER: *42%-efficient single-pass CW second-harmonic generation in periodically poled lithium niobate*. Optics Letters, 22(24):1834–1836, 1997.
- [159] PAVEL, N., I. SHOJI, T. TAIRA, K. MIZUUCHI, A. MORIKAWA, T. SUGITA and K. YAMAMOTO: *Room-temperature, continuous-wave 1-W green power by single-pass frequency doubling in a bulk periodically poled MgO:LiNbO<sub>3</sub> crystal*. Optics Letters, 29(8):830–832, 2004.
- [160] GAYER, O., Z. SACKS, E. GALUN and A. ARIE: *Temperature and wavelength dependent refractive index equations for MgO-doped congruent and stoichiometric LiNbO<sub>3</sub>*. Applied Physics B, 91(2):343–348, 2008.
-

- [161] GAYER, O., Z. SACKS, E. GALUN and A. ARIE: *Erratum to: Temperature and wavelength dependent refractive index equations for MgO-doped congruent and stoichiometric LiNbO<sub>3</sub>*. Applied Physics B, 94:367–367, 2009.
- [162] GAYER, O., Z. SACKS, E. GALUN and A. ARIE: *Erratum to: Temperature and wavelength dependent refractive index equations for MgO-doped congruent and stoichiometric LiNbO<sub>3</sub>*. Applied Physics B, 101:481–481, 2010.
- [163] ARIZMENDI, L.: *Photonic applications of lithium niobate crystals*. physica status solidi (a). 201(2):253–283, 2004.
- [164] SUGITA, TOMOYA, KIMINORI MIZUUCHI, YASUO KITAOKA and KAZUHISA YAMAMOTO: *Ultraviolet Light Generation in a Periodically Poled MgO:LiNbO<sub>3</sub> Waveguide*. Japanese Journal of Applied Physics, 40:1751–1753, 2001.
- [165] NISHIDA, Y., H. MIYAZAWA, M. ASOBE, O. TADANAGA and H. SUZUKI: *Direct-bonded QPM-LN ridge waveguide with high damage resistance at room temperature*. Electronics Letters, 39(7):609–611, 2003.
- [166] TOMITA, YOSHIHIRO, MASATO SUGIMOTO and KAZUO EDA: *Direct bonding of LiNbO<sub>3</sub> single crystals for optical waveguides*. Applied Physics Letters, 66(12):1484–1485, 1995.
- [167] KWON, S.W., W.S. YANG, H.M. LEE, W.K. KIM, H.Y. LEE, W.J. JEONG, M.K. SONG and D.H. YOON: *The ridge waveguide fabrication with periodically poled MgO-doped lithium niobate for green laser*. Applied Surface Science, 254(4):1101–1104, 2007.
- [168] KWON, S.W., Y.S. SONG, W.S. YANG, H.M. LEE, W.K. KIM, H.Y. LEE and D.Y. LEE: *Effect of photoresist grating thickness and pattern open width on performance of periodically poled LiNbO<sub>3</sub> for a quasi-phase matching device*. Optical Materials, 29(8):923 – 926, 2007.
- [169] PARK, JUN-HEE, WOO-KYUNG KIM, WOO-JIN JEONG, MYUNG-GUN SONG, HUN-HWA KIM, KYUNG-HWAN KOO, YEUNG-LAK LEE, YENA KIM, JU-HAN LEE, WOO-SEOK YANG and HAN-YOUNG LEE: *Continuous control of spatial mode rotation using second harmonic generation*. Applied Physics Letters, 97(19):191113, 2010.
- [170] PARK, JUN-HEE, TAI-YOUNG KANG, TAE-HO LIM and HAN-YOUNG LEE: *Simultaneous RGB light emission using second harmonic generation in z-cut MgO: Periodically-poled LiNbO<sub>3</sub> ridge waveguide*. In *Opto-Electronics and Communications Conference 2012*, pages 653–654, 2012.
- [171] WIEDMANN, J., O. BROX, T. TEKIN, F. SCHOLZ, T. BÜTTNER, S. MARX, G. LANG, H. SCHRÖDER, A. KLEHR and G. ERBERT:

- 
- Compact green laser source using butt-coupling between multi-section DFB-laser and SHG waveguide crystal.* Electronics Letters, 44(25):1463–1464, 2008.
- [172] MAIWALD, MARTIN, DANIEL JEDRZEJCZYK, ALEXANDER SAHM, KATRIN PASCHKE, REINER GÜTHER, BERND SUMPFF, GÖTZ ERBERT and GÜNTHER TRÄNKLE: *Second-harmonic-generation microsystem light source at 488 nm for Raman spectroscopy.* Optics Letters, 34(2):217–219, 2009.
- [173] MÜLLER, ANDRÉ, OLE BJARLIN JENSEN, KARL-HEINZ HASLER, BERND SUMPFF, GÖTZ ERBERT, PETER E. ANDERSEN and PAUL MICHAEL PETERSEN: *Efficient concept for generation of diffraction-limited green light by sum-frequency generation of spectrally combined tapered diode lasers.* Optics Letters, 37(18):3753–3755, 2012.
- [174] SAKAI, KIYOHIDE, YASUHARU KOYATA and YOSHIHITO HIRANO: *Blue light generation in a ridge waveguide MgO:LiNbO<sub>3</sub> crystal pumped by a fiber Bragg grating stabilized laser diode.* Optics Letters, 32:2342–2344, 2007.
- [175] ACHTENHAGEN, M., W. D. BRAGG, J. O’DANIEL and P. YOUNG: *Efficient green-light generation from waveguide crystal.* Electronics Letters, 44:985–986, 2008.
- [176] JEDRZEJCZYK, D., R. GÜTHER, K. PASCHKE, B. EPPICH and G. ERBERT: *200 mW at 488 nm From a ppMgO:LN Ridge Waveguide by Frequency Doubling of a Laser Diode Module.* IEEE Photonics Technology Letters, 22(17):1282–1284, 2010.
- [177] NASH, F. R., G. D. BOYD, M. SARGENT III and P. M. BRIDENBAUGH: *Effect of Optical Inhomogeneities on Phase Matching in Nonlinear Crystals.* Journal of Applied Physics, 41(6):2564–2576, 1970.
- [178] CAO, XIAOFAN, JAMAL NATOUR, RAMU V. RAMASWAMY and RAMAKANT SRIVASTAVA: *Effect of waveguide uniformity on phase matching for frequency conversion in channel waveguides.* Applied Physics Letters, 58(21):2331–2333, 1991.
- [179] DMITRIEV, V. G., A. G. ZLODEEV, V. A. KONOVALOV, and E. A. SHALAEV: *Hysteresis of the temperature phase-matching curve in second harmonic generation.* Soviet Journal of Quantum Electronics, 9(12):1539–1542, 1979.
- [180] HELMFRID, STEN and GUNNAR ARVIDSSON: *Influence of randomly varying domain lengths and nonuniform effective index on second-harmonic generation in quasi-phase-matching waveguides.* J. Opt. Soc. Am. B, 8(4):797–804, 1991.
-

- [181] JOHN H. LIENHARD V, JOHN H. LIENHARD V: *A Heat Transfer Textbook*. Phlogiston Press Cambridge, 4<sup>th</sup> edition, 2011. Version 2.01 dated January 22, 2011.
- [182] ZWILLINGER, DANIEL: *Handbook of Differential Equations*. Academic Press, Inc., 2<sup>nd</sup> edition, 1992.
- [183] CHERCHI, M., S. STIVALA, A. PASQUAZI, A. BUSACCA, S. RIVA SANSEVERINO, A. CINO, L. COLACE and G. ASSANTO: *Second-harmonic generation in surface periodically poled lithium niobate waveguides: on the role of multiphoton absorption*. Applied Physics B, 93(2):559–565, 2008.
- [184] SCHWESYG, JUDITH R., MATTHIAS FALK, CHRIS R. PHILLIPS, DIETER H. JUNDT, KARSTEN BUSE and MARTIN M. FEJER: *Pyroelectrically induced photorefractive damage in magnesium-doped lithium niobate crystals*. J. Opt. Soc. Am. B, 28(8):1973–1987, 2011.
- [185] SAHM, ALEXANDER, MIRKO UEBERNICKEL, KATRIN PASCHKE, GÖTZ ERBERT and GÜNTHER TRÄNKLE: *Thermal optimization of second harmonic generation at high pump powers*. Optics Express, 19(23):23029–23035, 2011.
- [186] SUN, JIAN, YI GAN and CHANGQING XU: *Efficient green-light generation by proton-exchanged periodically poled MgO:LiNbO<sub>3</sub> ridge waveguide*. Optics Letters, 36(4):549–551, 2011.
- [187] WENZEL, HANS, SVEN SCHWERTFEGER, ANDREAS KLEHR, DANIEL JEDRZEJCZYK, THOMAS HOFFMANN and GÖTZ ERBERT: *High peak power optical pulses generated with a monolithic master-oscillator power amplifier*. Optics Letters, 37(11):1826–1828, 2012.
- [188] BROX, O., T. PRZIWARKA, A. KLEHR, F. BUGGE, M. MATAALLA, H. WENZEL and G. ERBERT: *Integrated 13 GHz ps-pulse-source at 1064 nm*. Semiconductor Science and Technology, 28(4):045015, 2013.
- [189] RIECKE, S., S. SCHWERTFEGER, K. LAURITSEN, K. PASCHKE, R. ERDMANN and G. TRÄNKLE: *23 W peak power picosecond pulses from a single-stage all-semiconductor master oscillator power amplifier*. Applied Physics B, 98:295–299, 2010.
- [190] KOETH, J., M. FISCHER, M. LEGGE, J. SEUFERT and R. WERNER: *High performance quantum dot distributed feedback laser diodes around 1.15 μm*. SPIE Proc., 6909:690904, 2008.
- [191] *ISO 11146-1 Lasers and laser-related equipment – Test methods for laser beam widths, divergence angles and beam propagation ratios – Part 1: Stigmatic and simple astigmatic beams*. 2005.
- [192] EPPICH, BERND: *Optical Design of Beam Delivery and Beam Forming Systems*. Optik & Photonik, 3(2):48–51, 2008.

- [193] KU, H. H.: *Notes on the use of propagation of error formulas*. Journal of Reasearch of the National Bureau of Standards. Section C: Engineering and Instrumentation, 70C:263–273, 1966.